Direct Determination of Isosteric Heats of Sorption Using Pressure-Gradient Differential Scanning Calorimetry

By

Kerry-Anne White

Thesis presented in partial fulfilment of the requirements for the degree of Master of Science in Chemistry at Stellenbosch University

Department of Chemistry and Polymer Science

Supervisor: Prof Leonard Barbour

Co-supervisor: Dr Vincent Smith

December 2017

Declaration

By submitting this thesis electronically, I declare that the entirety of the work contained therein is my own, original work, that I am the sole author thereof (save to the extent explicitly otherwise stated), that reproduction and publication thereof by Stellenbosch University will not infringe any third party rights and that I have not previously in its entirety or in part submitted it for obtaining any qualification.

December 2017

Abstract

Porous materials, specifically porous coordination polymers (PCP) and metal-organic frameworks (MOFs), have shown great potential for catalysis as well as gas storage, separation and purification. Energy efficient adsorption processes utilising these porous materials are desirable for reducing the energetic cost of industrial processes. Thus characterisation of these materials in terms of their thermodynamic properties is essential for practical applications.

Isosteric heat (Q_{st}) is an approximation of the enthalpy (or heat) of sorption and indicates the affinity of a material for a specific adsorbate. Conventionally Q_{st} is determined indirectly by plotting isosteres at various temperatures and making use of the Clausius-Clapeyron approximation (the isosteric method). By comparing Q_{st} values from the literature, there appears to be a correlation between the Q_{st} value and the temperature range used. The higher the temperatures in the temperature range, the larger is the Q_{st} value. This contradicts the assumption of temperature independence by the Clausius-Clapeyron approximation.

Heat-flow calorimetry employing a temperature gradient is another method that has been used to determine Q_{st}. A calorimetric approach requires fewer assumptions regarding the interaction energies and equilibrium of the system compared to the isosteric method. Herein a method is proposed for the direct determination of Q_{st} using pressure-gradient differential scanning calorimetry (PGDSC). The PGDSC method involves the measurement of heat flow during the sorption and desorption of a gas over a predefined pressure range. In conjunction with gas loading data derived from gas sorption isotherms, Q_{st} can be determined directly over the entire pressure (or rather gas loading) range from the changes in measured heat flow. The sorption of CO_2 by CuHKUST was chosen as a test system to validate this direct method. It was found that the PGDSC approach produces temperature-independent values that are comparable to literature values obtained using the isosteric method. Since the PGDSC method is temperature independent, it requires a less labour-intensive procedure than the isosteric method. Only one PGDSC experiment and one isotherm at the same temperature are required, as opposed to multiple isotherms at various temperatures necessary for the application of the isosteric method. PGDSC furthermore employs direct heat measurements as compared to the indirect approximation of the isosteric method.

The PGDSC method was further successfully applied to a 2D-layered interdigitated PCP ($[Cd(oba)(bpy)]_n$) that displays stepped sorption and hysteresis for CO_2, N_2 and CH_4. Since the isosteric method is not easily applied to materials with sorption profiles other than Type I, this presents an important improvement in how Q_{st} values are measured. Q_{st} values can also be used to predict the selectivity of the material for a specific gas. This investigation showed that $[Cd(oba)(bpy)]_n$ has the highest affinity for CO_2 over N_2 and CH_4.

Uittreksel

Poreuse materiale, spesifiek poreuse koördinasie polimere (PKPe) en metaal-organiese raamwerke (MORe), toon groot potensiaal vir katalise sowel as die berging, skeiding en suiwering van gasses. Die energie-doeltreffende adsorpsieprosesse wat hierdie poreuse materiale gebruik is begeerlik vir die verlaging van die energie koste van industriële prosesse verminder. Die karakterisering van hierdie materiale in terme van hul termodinamiese eienskappe is dus noodsaaklik vir praktiese toepassing.

Isosteriese hitte (Q_{st}) is verwant aan die entalpie (of hitte) van sorpsie en dui die affiniteit van die materiaal vir die adsorbaat aan. Gewwonlik word Q_{st} indirek bepaal deur isostere by verskillende temperature te plot en gebruik te maak van die Clausius-Clapeyron-benadering (ook genoemd, die isosteriese metode). Deur Q_{st}-waardes uit die literatuur te verkeglyk blyk daar om 'n verband tussen die Q_{st}-waarde en die temperatuurreeks wat gebruik word te wees. Hoe hoër die temperature in die temperatuurreeks, hoe groter is die Q_{st}-waarde. Dit is teenstrydig met die aanname van temperatuur onafhanklikheid in die Clausius-Clapeyron benadering.

Hitte-vloei kalorimetrie teen 'n temperatuurgradiënt is ‘n manier wat gebruik kan word om Q_{st} te bepaal. ‘n Kalorimetriese benadering benodig minder aannames ten opsigte van die interaksie energie en die ewewig van die stelsel in vergelyking met die isosteriese metode. Hierin word 'n metode vir direkte -bepaling van Q_{st} voorgestel met behulp van druk-gradiënt differensiële skanderingskalorimetrie (DGDSK). Die DGDSK metode behels die meting van hitte vloei gedurende die sorpsie en desorpsie van 'n gas oor 'n voorafbepaalde druk reeks. Q_{st}, tesame met gas lading data afgelei vanaf gas sorpsie isoterme, kan direk bereken word oor die hele druk (oftewel gas lading) reeks vanaf die gemete verandering in hitte vloei. Die opneem van CO_2 deur CuHKUST met is gekies as 'n toets sisteem om hierdie direkte metode te beproef. Daar is gevind dat die DGDSK benadering temperatuur onafhanklike Q_{st} waardes produseer wat vergelykbaar is met literatuur Q_{st} waardes verkry vanaf die isosteriese metode. Omdat die DGDSK-metode temperatuur onafhanklik is, is hierdie prosedure minder veeleisend as die isosteriese metode aangesien slegs een DGDSK-eksperiment en een isoterm by dieselfde temperatuur nodig is, in teenstelling met verskeie isoterme by verskillende temperature wat nodig is om die isosteriese metode toe te pas. Verder word direkte gemete veranderinge in hitte vloei gebruike vir DGDSK ingespan in vergelyking met die indirekte benadering van die isosteriese metode.

Die DGDSK -metode is ook suksesvol toegepas op 'n 2D inmekaar geritsde PKP ($[Cd(oba)(bpy)]_n$) wat trapvormige sorpsie en histerese vir CO_2, N_2 en CH_4 vertoon. Aangesien die isosteriese metode nie maklik toegepas kan word op materiale met ander sorpsieprofiele as Tipe I nie, is dit 'n belangrike verbetering van hoe Q_{st} waardes gemeet kan word. Q_{st} waardes kan ook gebruik word om die selektiwiteit van die materiaal vir ‘n spesifieke gas te voorspel. Hierdie ondersoek, het getoon dat $[Cd(oba)(bpy)]_n$ die hoogste affiniteit vir CO_2 teenoor N_2 en CH_4 getoon.

Acknowledgements

- I would like to thank my supervisor Prof. Len Barbour for giving me the opportunity to complete my MSc in a world-class environment. We are truly fortunate to be in a group this well-equipped and successful. I am grateful for the opportunity to present my work locally and abroad at international conferences and to meet some of the authors I have cited.
- I would also like to thank my co-supervisor Dr Vincent Smith who was the first person to introduce me to Supramolecular Chemistry, for which I am grateful. Thank you for all the advice and the extra effort you always put in for your students.
- Dr Charl Bezuidenhout has been a fantastic mentor throughout my time in the research group. He always found time for in-depth discussions and advice.
- I would like to thank Dewald van Heerdan and Dr Leigh Loots specifically for their constant assistance with all things thesis related, and for the motivation.
- The Supramolecular Materials Chemistry Group members at the University of Stellenbosch provided a helpful environment to learn and grow as a scientist. They also provided a friendly environment to socialise and relax on occasion; I am especially grateful for those lunchtime talks.
- I thank Debbie, who keeps our office clean and tidy so that we can work in a comfortable environment. Thank you for the morning smiles and stories.
- Thanks to my friends and family, especially Charl Viljoen and Alison White, who have been patient, understanding and supportive throughout. You are loved and appreciated.
- National Research Foundation (NRF) and The Harry Crossley Scholarship provided financial support, for which I am grateful.

Publications

1. Article in editing phase due to be submitted.

Conferences

1. The 23rd International Conference on the Chemistry of the Organic Solid State: ICCOSS-2017 in Stellenbosch, South Africa. Poster: *Direct Determination of Isosteric Heats of Sorption Using Pressure-Gradient Differential Scanning Calorimetry*.
2. The 6th Latin American Symposium on Coordination and Organometallic Chemistry: SILQCOM6 (2017) in Puerto Iguazú, Argentina. Poster: *Direct Determination of Isosteric Heats of Sorption Using Pressure-Gradient Differential Scanning Calorimetry*.
   (Awarded 1st place poster prize).

List of abbreviations and symbols

1D	one dimensional
2D	two dimensional
3D	three dimensional
ANG	adsorbed natural gas
ASU	assymmetric unit
BET	Brunauer-Emmett-Teller
bpy	4,4'-bipyridine
CIF	crystallographic information file
CP	coordination polymer
DSC	differential scanning calorimetry
FNG	free natural gas
GCMC	Grand Canonical Monte Carlo
IUPAC	International Union of Pure and Applied Chemistry
MOF	metal-organic framework
M_r	molecular mass
NIST	National Institute of Standards and Technology
oba	4,4'-oxybis(benzoic acid)
PCP	porous coordination polymer
PGDSC	pressure-gradient differential scanning calorimetry
PXRD	powder X-ray diffraction
SCXRD	single-crystal X-ray diffraction
TGA	thermogravimetric analysis
TMA	trimesic acid or benzene-1,3,5-tricarboxylic acid
Z	number of formula units in the unit cell
α	angle between the b and c axes
β	angle between the a and c axes
γ	angle between the a and b axes
θ	angle of X-ray incident beam
ΔG_{ads}	Gibbs free energy of adsorption
ΔH_{ads}	enthalpy of adsorption
ΔH_{des}	enthalpy of desorption
ΔH_{vap}	enthalpy of vaporisation
ΔS_{ads}	entropy of adsorption
Q_{diff}	differential heat
Q^{int}	integral heat
Q_{st}	isosteric heat of sorption

Atom colours

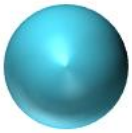

Cadmium

Oxygen

Nitrogen

Carbon

Table of contents

Chapter 1 Introduction

Porous materials have shown great potential for catalysis as well as gas storage, separation and purification.[1] Energy efficient adsorption processes utilizing these porous materials are desirable for reducing the energetic cost of industrial processes.[2] Carbon-based materials, such as activated carbon, and inorganic materials, aluminosilicates and aluminophosphates, were the first porous materials to spark interest and have dominated industry and research ever since. Activated carbons have high porosity and large surface areas but are limited by their disordered arrangements. Zeolites (also known as molecular sieves), have 3-dimensional (3D) framework structures consisting of alkaline or alkaline-earth aluminosilicates that contain cavities occupied by water molecules or large ions. Open porous channels and cavities are made available by the movement of these ions or through dehydration.[3,4] Zeolites occur naturally (eg. phillipsite, chabazite, clinoptilolite, mordenite, stilbite, analcime and laumontite) and are commonly formed near volcanic areas.[5] The first attempts at chemically synthesising zeolites in the laboratory, by Sainte Claire Deville[6] (1862), spurred the synthesis and modification of zeolites to produce interesting and useful chemical properties.[4]

1.1 Coordination polymers and metal-organic frameworks

In recent years 1D, 2D and 3D organic-inorganic hybrid materials have come to the forefront as materials with exploitable properties.[3] These materials are also referred to as coordination polymers which encompasses structures with an infinite extended structure of metal nodes linked by bridging organic ligands.[7,8] When the materials are porous (defined later in 1.1.2) the term porous coordination polymer (PCP) is most descriptive. The first coordination polymer was synthesised by Hofmann (Hofmann complex/clathrate)[9] in 1897 while its molecular structure was later elucidated by Powell and Rayner[10] (1949) to be a 2D arrangement of $(Ni(CN)_2(NH_3)\cdot C_6H_6)_n$. It is widely accepted that the first 3D PCP, with a copper node and 4,4',4",4"'-tetracyanotetraphenylmethane as an organic linker, was synthesised by Hoskins and Robson[11] (1990), who predicted that many more would soon be studied: "The results provide confidence that a wide range of scaffolding-like solids should prove accessible". They estimated that the enclosed guest molecules occupy about two-thirds of the total volume.

In 1995 Yaghi *et al.* introduced the term Metal-Organic Frameworks (MOFs) to describe robust 2D and 3D coordination polymers consisting of metal centres (nodes) and organic linkers.[12,13] From their work with MOF synthesis, Yaghi and co-workers put forward the idea of reticular synthesis. This concept is described as "…the process of assembling judiciously designed rigid molecular building blocks into predetermined ordered structures (networks), which are held together by strong bonding."[14] Essentially it describes the idea of designing frameworks to have certain desirable topologies and properties. Secondary building units, recurring metal cluster motifs and framework structural designs, once synthesised, can be analysed and reproduced using similar ligands and metal ions as these are the main factors influencing the topology of frameworks.[15,16]

Terminology surrounding these types of materials is varied and can cause confusion even among those in the field. For the purposes of this study, the recommendations set out by IUPAC[17] will be followed. It is recommended that the term "coordination polymer" (CP) be used as a blanket term encompassing all types of

coordination and dimensions.[7] MOFs are a subset of the CP class where metal ions must be the nodes of the framework. Another criterion to be met is that MOFs must contain voids with the potential for porosity, although they need not be measured i.e. do not need to be porous *per se*.[17] MOF research increased dramatically as a result of their large pore sizes, surface areas, robust porosity and, more importantly, their potential for designable properties.[16,18,19]

Kitagawa *et al.* quoting Aristotle, "*nature abhors a vacuum*," suggests that it is not possible to synthesise empty MOF structures without the initial inclusion of guest molecules. These guest molecules can have a templating effect and in some cases they also stabilise the structure.[3] Thus, MOFs can be classified into three classes based on their response to guest removal (Figure 1.1). First generation coordination polymers collapse into amorphous material upon guest removal. The second generation materials retain their rigidity and crystallinity when the guest molecules are removed, while third generation materials collapse into a different phase but retain crystallinity. Third generation materials are transformable due to contributions from the metal and ligand that can provide some flexibility.[20] This gave rise to the idea of "soft porous" materials.

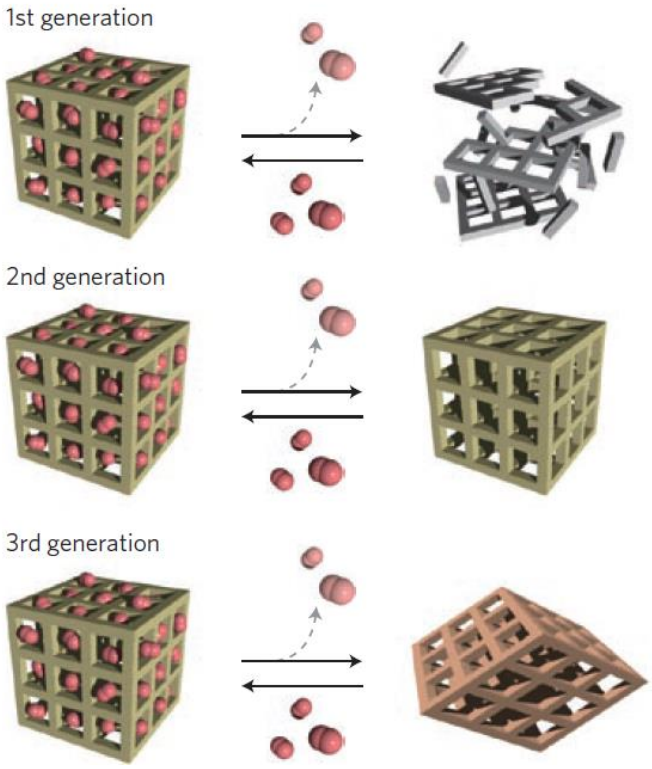

Figure 1.1 The three classes of coordination polymers described by Horike *et al.*[20]

1.1.1 Soft porous crystals

The idea that crystallinity is synonymous with rigidity is surprisingly inaccurate for some MOFs. Third generation materials (as described in Figure 1.1) have dynamic and flexible frameworks that can respond to external stimuli by changing their channels or pores; they are termed "soft porous" materials. Stimuli can include light, heat, electric field and guest molecules.[20] Flexibility in frameworks is mainly due to the rearrangement of the weak interactions, namely coordination bonds, π-π interactions and van der Waals

interactions, between the components. Another factor conferring structural flexibility is the dynamic motion, rotational and vibrational movements, of the organic ligands in the MOF.[21] There are many ways that flexibility can manifest in these frameworks. Kitagawa and Uemura categorise them as shown in Figure 1.2 and go on to recommend that judicious choice of the framework components can lead to the manifestation of these arrangements, as suggested by Yaghi (reticular synthesis).[14,22]

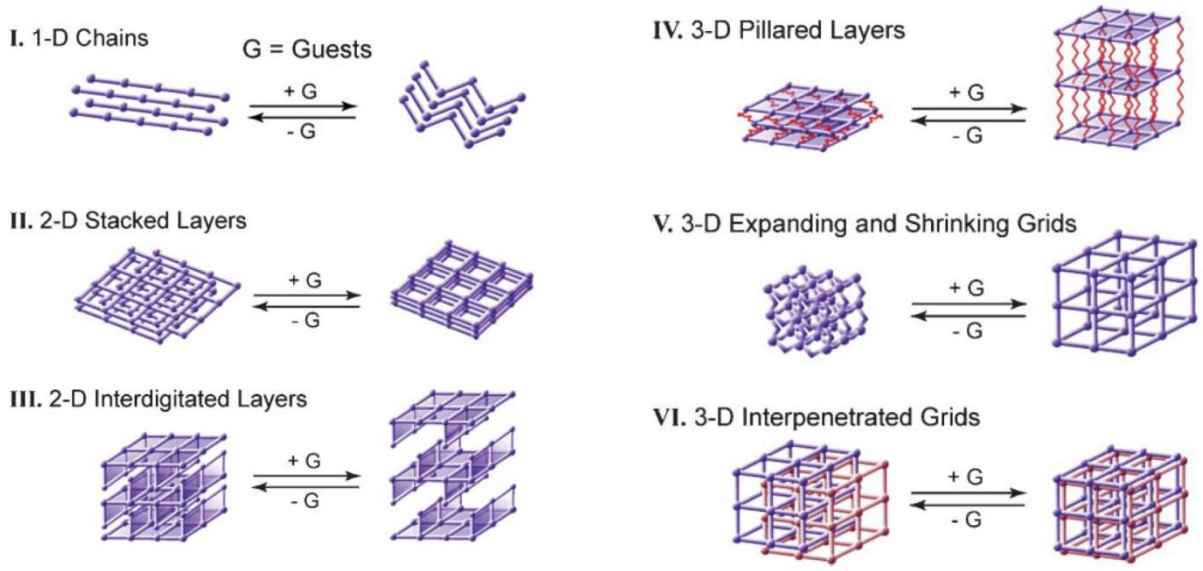

Figure 1.2 Possible motifs of dynamic porous coordination polymers. Adapted from Kitagawa and Uemura.[22]

The dynamic nature of these structures affect how guest molecules are sorbed. The gas sorption isotherms of these materials tend to exhibit interesting profiles that deviate from the Brunauer-Teller isotherm profiles (see section 1.2).[23] Gate-opening and "breathing" has been observed in which the sorption profile shows little gas uptake at low pressure but an abrupt uptake occurs at a threshold pressure. This is characteristic of soft porous materials and is associated with a structural transformation of the motifs from non-porous to porous, especially in systems that are interdigitated (Figure 1.2 III) or interpenetrated[24] (Figure 1.2 VI) as these entanglements allow movement between layers and motifs. 2D interdigitated layers have been particularly well studied for this sorption property.[20,25,26] Flexibility can lead to some gas selectivity as suggested by Matsudo, likening the selectivity of MOFs to the induced-fit capability of proteins.[21] Rosseinsky *et al.* reported an example of a porous MOF that is selective for *p*-xylene and they showed how the MOF adapts its channels in a positive feedback loop.[27] Crystal properties, including flexibility, influence sorption behaviour. Before gas sorption is discussed, it is prudent to define what is meant by porosity.

1.1.2 Porosity

Porosity (ε) can be defined as the ratio of specific accessible space (pore volume) to the volume of the adsorbent, as described by Rouquerol *et al.*[28] A porous material (host) has cavities, channels or pores that allow dynamic transport of another compound (guest) through its bulk. Pore size classification according to IUPAC[29]

is as follows: pores exceeding 50 nm are macropores, those between 2 and 50 nm are called mesopores, and pore sizes less than 2 nm are considered micropores.

Porosity is often misinterpreted and must be carefully considered before any claims thereof are made. Barbour[30] proposes two key criteria that must be met to confirm porosity: firstly, permeability must be proven through sorption, and secondly, the term "porosity" must apply to a specific host phase rather than being used as a general term for the material. Conventional or permanent porosity exists only if the host framework can retain its structure without collapsing once the guest molecules are removed.[30] This occurs in systems such as zeolites and very rigid MOFs. It is common for PCPs and other MOFs (usually flexible systems) to collapse to a more tightly packed "closed" phase. If the collapsed phase is still permeable then that phase can be described as porous "without pores" a property attributed to momentary cooperation of the host components to allow for guest diffusion. This type of porosity can also be termed *transient* porosity and can occur in materials that seem nonporous but are able to take up gas, such as materials with isolated 0D pores or closely packed materials.[30,31] Non-conventional porosity is especially important for flexible frameworks where the "activated" (guest removed) closed form is transformed into a porous compound after exposure to gas.[32]

The degree of porosity can be determined by measuring the surface area using the Brunauer-Emmett-Teller (BET) gas sorption method with nitrogen gas.[33] However, it must be noted that this demonstrates nitrogen sorption and does not necessarily indicate that it is possible for other gases to be sorbed by the host.[34] Other probe sizes, i.e. other gases, can be used for a more accurate surface area determination.[33] The largest reported surface area to date is ~7000 m^2/g for MOFs NU-109/110.[35]

Virtual porosity is often reported but it is discouraged. It is entails deleting selected guest atoms *in silico* to show the "void" that was occupied by that guest. This is usually not supported by an experimental demonstration of permeability and is therefore not true porosity.[30]

Porous coordination polymers can be classified into four groups based on the dimensionality of the cavities as shown in Figure 1.3. Zero-dimensional (0D) cavities are isolated from each other and the crystal surface and therefore so are the trapped guest molecules. One-dimensional (1D) channels extend along one direction while two-dimensional (2D) channels extend along two directions and three dimensional (3D) space has intersecting channels along three directions.

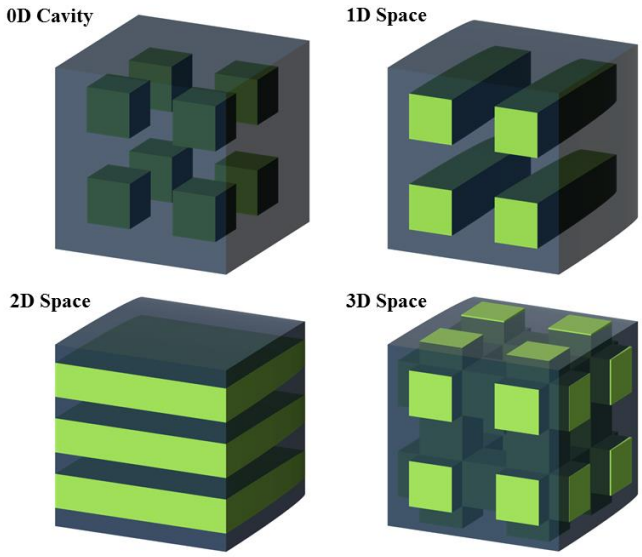

Figure 1.3 Dimensionality of porous coordination polymers. Figure recreated from Kitagawa *et al.*[3]

Porosity in coordination polymers has led to many applications, including catalysis,[36,37] gas storage,[2,38–42] drug delivery,[43,44] sensing[45,46] and chemical separations.[15,47–49] Kitagawa very recently suggested that hybrid materials (fourth generation) may enhance and combine current properties of third generation materials and lead to new properties that will promote current and future applications.[50]

1.2 Gas sorption

The generic term sorption is used to describe the process of a gas (sorptive) being taken up by a solid porous material (sorbent).[31] Once the sorptive has been taken up, it is termed the sorbate. It is difficult to distinguish between adsorption and absorption when discussing the uptake of gases by porous materials. According to the IUPAC, the term absorption is used to describe sorbate penetration deeper than the surface layer where it enters the bulk of the solid, while adsorption is used to describe the incorporation of the sorbate into the interfacial layer (comprising the surface layer and the adsorption space). Adsorption can either occur through chemisorption, where chemical bonds form between the adsorbent and adsorbate, or through physisorption where van der Waals interactions are mainly responsible for the uptake of gas.[28,34] It has become commonplace to use the term adsorption to describe physisorption. Therefore the term sorption will be used here to describe adsorption, and the term desorption will describe the converse process of expelling the adsorbed gas. Sorption and desorption are presented as a sorption isotherm, where the amount of gas sorbed is plotted as a function of the equilibrium pressure at constant temperature. Hysteresis arises when the sorption profile does not match the desorption profile (see Section 1.2.1, Figure 1.4 for isotherm and hysteresis profiles).[34]

Filling of the pores and cavities of a porous material is dependent on three factors: the molecular sieving effect resulting from the size exclusion principle, the thermodynamic effect resulting from the favourable packing of gas molecules, and lastly the kinetic effect determined by the kinetic diameter of the gas. These factors can also affect the selectivity of the material for specific gases over others.[51] The primary mechanism

for physisorption when there are only micropores present is micropore filling. The presence of mesopores causes physisorption to take place in more than one step. Firstly, monolayer adsorption[52] occurs when adsorbed molecules coat the surface layer of the pores followed by multilayer adsorption where not all the molecules are in contact with the surface layer of the adsorbent. Finally the remaining residual pore space is filled through capillary condensation where the adsorbate is condensed to a quasi-liquid state. The adsorbate and adsorbent can be considered as one unit where the trapped guest is part of the framework and is no longer considered to be in a gaseous state.[34,53] The excess amount (n^{σ}) is defined as the difference between the total amount (n) of the adsorptive and the amount that would be present in a reference system in which no adsorption occurs.[28]

Thermodynamically, the process of physisorption must be exothermic for it to be spontaneous ($\Delta G_{ads}{}^{0} < 0$). As a result of the adsorption process, molecules are in a more ordered state as they are restricted to a surface or pore. This is translated into a decrease in entropy ($\Delta S_{ads}{}^{0} < 0$) that is compensated for by a negative enthalpy ($\Delta H_{ads}{}^{0} < 0$). Therefore a decrease in temperature is favoured by the physisorption process.[54]

$$\Delta G^{0}_{\mathrm{ads}} = \Delta H^{0}_{\mathrm{ads}} - T\Delta S^{0}_{\mathrm{ads}} \qquad \textbf{Eq. 1.1}$$

1.2.1 Isotherm and hysteresis profiles

Physisorption isotherms can usually be grouped into the six types shown in Figure 1.4 as defined by the IUPAC based on Brunauer's work.[34,55] At very low loading (concentration of adsorbed gas per gram of material, mmol/g), the isotherms can be considered linear and the range is referred to as the Henry's Law region where the adsorbed molecules are still independent of each other. The reversible Type I isotherm is typically exhibited by microporous solids and the uptake is usually limited by the size of the sorbtive (molecular sieving effect). The plateau of the isotherm represents the completion of monolayer adsorption.[33] Type I was first reported by Langmuir, who proposed the concept of a one-molecule thick adsorption layer (the monolayer); the profile is sometimes referred to as the Langmuir isotherm.[52] Type II, also reversible, is associated with macroporous materials with monolayer-multilayer sorption. Point B in Figure 1.4 indicates where monolayer sorption is complete and where multilayer sorption begins. Type III isotherms are also reversible, but uncommon. For this type, adsorbate-adsorbate interactions play a crucial role and the isotherm is concave. Type IV isotherms have a hysteresis loop that is usually associated with mesopores where capillary condensation takes place. The end of multilayer adsorption and the start of capillary condensation are indicated by the upward curve of the isotherm (deviating from the initial Type II shape).[33] Also uncommon, Type V is related to Type III where adsorbate-adsorbate interactions overshadow adsorbent-adsorbate interactions. Lastly, the number and sharpness of the steps in the Type VI isotherm are dependent on the system and temperature.[34]

Hysteresis loops appear in the multilayer adsorption range of physisorption for Type IV and V isotherms and are mostly associated with capillary condensation. According to Rouquerol *et al.*[28] the amount adsorbed is dependent on the chemical potential of the adsorptive (gas), which means that the two branches of the hysteresis loop are not thermodynamically reversible. It follows that if there is a stable reproducible hysteresis loop then there are metastable states present.[28] Types H1 and H4 hysteresis loops are the two extremes of the four types where Type H1 branches are nearly vertical and parallel compared to Type H4 branches, which are nearly horizontal and parallel. The various types of hysteresis loops are associated with different defined pore structures. Type H1 hysteresis loops are given by a narrow distribution of uniform pores, whereas Type H2 loops are associated with a complex interconnecting network of different shaped and sized pores. Type H3 hysteresis loops are usually associated with slit-shaped pores as are Type H4 loops, but the latter have pores mainly in the microporous size range.[34]

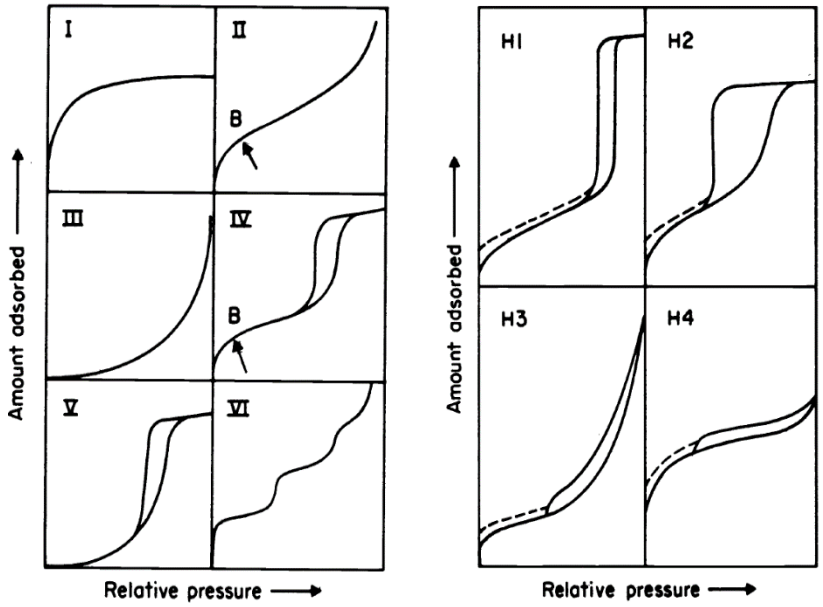

Figure 1.4 **Left** - The six types of physisorption isotherms. **Right** - The four types of hysteresis loops. The sorption profiles are based on the original work of Brunauer *et al.* The isotherm classifications are limited to single-component gas adsorption. Figure 1.4 is adapted from Sing *et al.*[34,55]

As mentioned above, stepped or gated sorption isotherms that deviate from the classical Brunauer-Teller isotherm profiles are being reported more frequently and are associated with framework structural transformations due to the dynamic flexible nature of PCPs.[32,56,57] In some cases this involves bond breakage between metal and ligands, or deformations of the framework through layer movements.[58] In other cases the sorption isotherm is manipulated by tuning the gate-opening phenomenon through doping.[59]

1.2.2 Sorption methods

There are two main methods for recording of sorption data: volumetric and gravimetric. Both have advantages and disadvantages. Volumetric measurements involve recording of pressure differences usually using a Sievert-style instrument. With this type of instrument there is an accumulation of uncertainties with every pressure measurement, and high pressure measurements tend to be less accurate than low pressure

measurements. The gravimetric method uses a microbalance with a suspended pan in a gas-filled chamber. Buoyancy corrections are a concern with this type of sorption measurement. Recently there have been combinations of the two methods to combat these limitations.[28,60]

Typically, adsorption measurements are made in a discontinuous manner, where the adsorptive is introduced in point-by-point doses. After each dose, thermodynamic equilibrium is reached before the next dose is introduced. More recently, continuous procedures have been utilised but they are still not common. Instead of the adsorptive being introduced in doses, it is fed continuously, at an appropriately slow rate that allows for quasi-equilibrium such that the rate of introduction approximates the rate of adsorption.[28,61]

When evaluating the merits of a given porous material for gas sorption it is necessary to consider several important factors. These include working capacity, saturation pressure, hysteresis, kinetics, selectivity, heats of sorption, and the temperature-dependence of all of these phenomena. With the exception of heats of sorption, it is possible to measure these parameters directly using standard sorption isotherms. As the adsorption process is spontaneous, with a decrease in enthalpy and entropy, it follows that adsorption is an exothermic process and the enthalpy involved is called the heat of sorption.[62]

1.3 Heats of sorption

The isosteric heat of sorption (Q_{st}) is an approximation of the enthalpy of sorption (ΔH_{ads} or ΔH_{des}) and is influenced by various adsorbent-adsorbate and adsorbate-adsorbate interaction energies.[63] The thermodynamic expression of isosteric heat of a pure gas is given as:

$$Q_{st} = h^{g} - \left[\frac{\delta H^{m}}{\delta n^{m}}\right]_{T} \qquad \textbf{Eq. 1.2}$$

where h^{g} is the molar enthalpy in the gas phase, H^{m} is the specific enthalpy of the adsorbed phase and n^{m} is the specific amount adsorbed. The bracketed second term represents the differential enthalpy in the adsorbed phase.[64]

At zero loading, where adsorbate-adsorbate interactions are eliminated, Q_{st} can provide an indication of the strength of interaction between the adsorbate and adsorptive.[28] The strength of the interaction between the adsorbate and adsorbent can be used to distinguish between chemisorption and physisorption. According to Gatta,[62] if the heat of sorption exceeds 20 kJ/mol then the process is regarded as chemisorption, and if the heat of sorption is below this value, it is physisorption. For physisorption, because van der Waals forces are responsible for the interaction, the binding energy should be close to the condensation heat of the gas. For chemisorption, Gatta suggests that the enthalpy involved in adsorption is of the same order of magnitude as the bonds in free molecules; 30-600 kJ/mol.[62] According to Bowker, the values for potential energy are similar; ~20 kJ/mol for physisorption and between ~40-600 kJ/mol for chemisorption.[65] The strength of the interaction could also provide an indication of potential selectivity; high values could indicate a preference for a specific gas. However, this could also have negative implications for the regeneration of the material as harsher conditions may be needed to remove the sorbate. Historically, Q_{st} is obtained in two ways: indirectly through isosteres[66] or directly using calorimetry.[62]

1.3.1 Isosteric method

By far the most common method for determining Q_{st} is through the use of isosteres. Known as the isosteric method, this is an indirect approach employing a series of sorption isotherms at different temperatures (at least two). Various adsorption and mathematical models can be applied to the adsorption isotherms, including the Sips, Toth, and Langmuir equations for loading.[67]

To determine Q_{st} from these isotherms, the Clausius-Clapeyron approximation[68] is used:

$$\frac{dP}{P} = \frac{\Delta H_{vap}}{R}\frac{dT}{T^2} \qquad \textbf{Eq. 1.3}$$

where[29]

$$\Delta H_{vap} = -\Delta H_{ads} \approx Q_{st} \qquad \textbf{Eq. 1.4}$$

Assuming temperature independence, Q_{st} is approximated using the integrated version of the Clausius-Clapeyron approximation:

$$lnP = \frac{-Q_{st}}{R}\frac{1}{T} + C \qquad \textbf{Eq. 1.5}$$

where P is pressure or fugacity, R is the gas constant, T is temperature (measure in Kelvin) and C is a constant from integration.

Q_{st} is obtained by graphical interpolation of best-fit straight lines, ln P vs $1/T$ at constant loading (shown in Figure 1.5) where the gradient is used to determine Q_{st}. The term "isosteric" here means "constant volume" i.e. a constant volume adsorbed.[69] It is important to note that Q_{st} is determined from a line of best fit, rather than determining the gradient at each point.[70] Another method to determine Q_{st} is by using the Virial equation but this method requires the investigator to arbitrarily choose the number or parameters.[67]

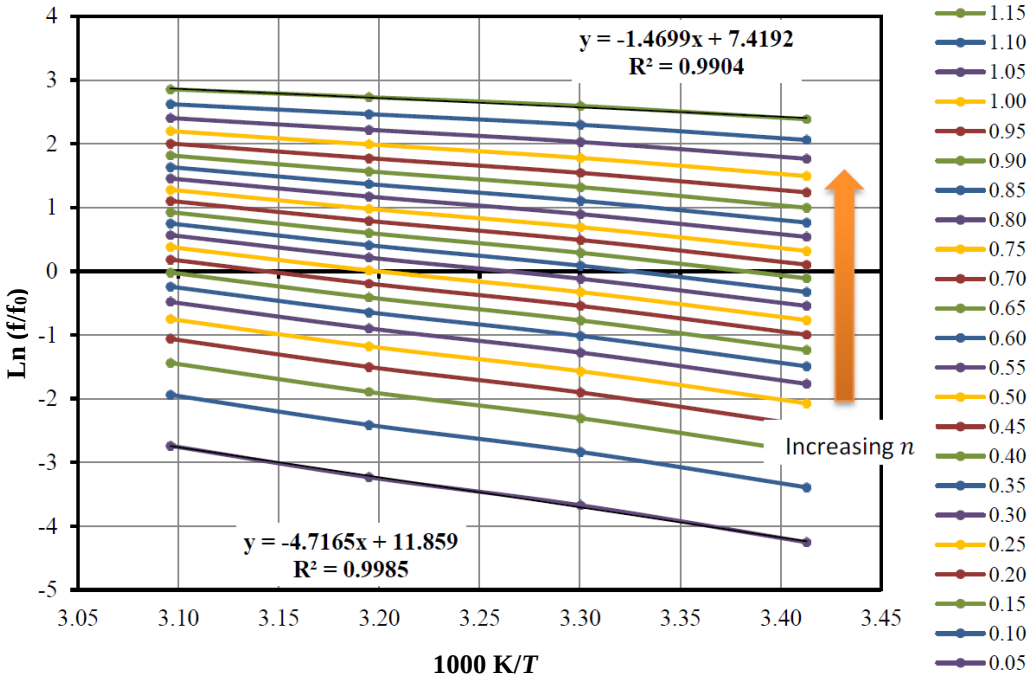

Figure 1.5 An example of isosteres for a metallocycle - [Cd_2(4,4′-bis(2-methylimidazol-1-ylmethyl)-1,1′-biphenyl)$_2Cl_4$] investigated by van Heerden.[67] Here fugacity is used: effective pressure exerted by a real gas.

The isosteric method is most widely used for determining Q_{st} because of its simplicity and the general availability of the required instrumentation. However, it should be noted that this method makes several assumptions, such as ideal gas behaviour and temperature-independence of ΔH_{vap} of the sorbate gas,[71] and it also ignores the adsorbed gas phase volume. The consequence of such assumptions is that there are inaccuracies at high loading (high pressure) (Figure 1.6).[72,73] It has also been shown that at low loading (< 0.5 mmol/g), pressure measurements need to be extremely accurate for the isosteric method to yield reliable Q_{st} values.[28,69]

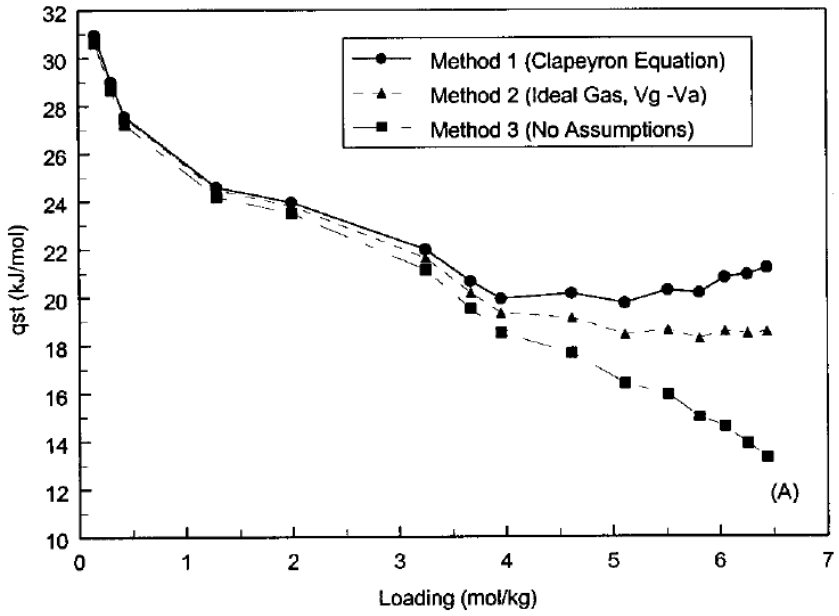

Figure 1.6 The isosteric heats of adsorption of ethane on BAX carbon (high grade activated carbon) at 300 K calculated from three methods: ● – Clausius-Clapeyron equation. ▲ – assuming ideal behaviour and taking into account the adsorbed gas volume. ■ – not assuming ideal gas behaviour and taking into account the adsorbed gas volume. Adapted from Balbuena *et al.*[72]

Computational methods make it possible to determine isosteric heats of sorption in the absence of experimental data by generating theoretical sorption isotherms. The most used technique, grand canonical Monte Carlo (GCMC) simulation, makes use of the Boltzmann distribution law to predict the average movement of molecules.[28,69] Isosteric heat of sorption is then determined using simulated isosteres, as described above.[74]

1.3.2 Calorimetry

Direct determination of Q_{st} is accomplished through the measurement of heat flow during the sorption-desorption process using calorimetry. The word "calorimeter" comes from the Latin word *calor*, meaning "heat capacity", and the Greek word *meter*, meaning "measure". The principles used today in calorimetry were formed by Galilei. The development of calorimetry date back to the 18th century and progressed further once the work carried out by Hess was published.[75] Hess's Law states: "The heat effect of chemical reactions depends not on the path along which the system passes from state I to state II but only on the initial and final

state."[68] In the 20th century, microcalorimetry was introduced to measure long-term, constant and small heat effects.[75] Ward advanced microcalorimetry for the measurement of heats of adsorption of gases by solid substances.[76] For further reading on calorimerty, see *Calorimetry* by W. Zielenkiewicz.[75]

Compared to the isosteric method, fewer assumptions are made during the calorimetric approach regarding the interaction energies and the system equilibrium.[62] Conventional calorimetry measures heat flow directly, usually with a Tian-Calvet type calorimeter. This method makes use of differential heat (heat as a function of loading) to calculate isosteric heat[77]:

$$Q_{st} = Q_{diff} + RT \qquad \textbf{Eq. 1.6}$$

Differential scanning calorimetry (DSC) measures heat flow at constant pressure with temperature changes recorded as a function of time.[68] Pressure-gradient differential scanning calorimetry (PGDSC), used in this study, is performed by measuring the heat flow of the reaction while maintaining a continuous pressure gradient under isothermal conditions (a more detailed description is given in Chapter 2). Llewellyn and Maurin have shown that continuous introduction of gas to an adsorptive material in a calorimeter, as opposed to incremental dosing, increases resolution in the heat flow curve. This allows subtle adsorption phenomena to be observed.[78] Gupta *et al*.[79] reported an instrumental setup which closely matches that described in this study but they carried out constant high-pressure DSC experiments. In this study, the temperature is kept constant while the pressure is ramped.

Calorimetric determinations of the heats of adsorption in zeolites have been explored previously but few studies consider PCPs, for which the widely used isosteric method has been preferred.[63,77,78] Previous studies comparing isosteric and calorimetric methods show large deviations of between 10-100% for the same systems.[80]

1.3.3 Applications

Three uses for isosteric heats of sorption are: i) energetic characterisation of the sorbent, ii) providing data for new theories for adsorption equilibria and kinetics, iii) providing information for the design of industrial adsorption processes such as pressure or temperature-swing adsorption.[80] Isosteric heat can provide an indication of the extent to which the environment temperature changes during the adsorption (exothermic) and desorption (endothermic) processes.[81] Adsorbed natural gas (ANG) systems, where natural gas is stored as adsorbed gas in porous materials, are of industrial interest for NG storage and transport. ANG has a lower storage pressure than free natural gas (FNG) but since the management of the thermal effects have been neglected the development of this technology has not progressed.[82] Other technologies dependent on this development include heat pumps and cooling systems where an adsorptive material is used in conjunction with water (or methanol) as a means of heating or cooling the environment.[83–85] There are five important factors to optimize when evaluating an ANG/adsorptive system, as shown in Figure 1.7. Heat of adsorption and thermal effects go hand in hand as one determines the other.[86]

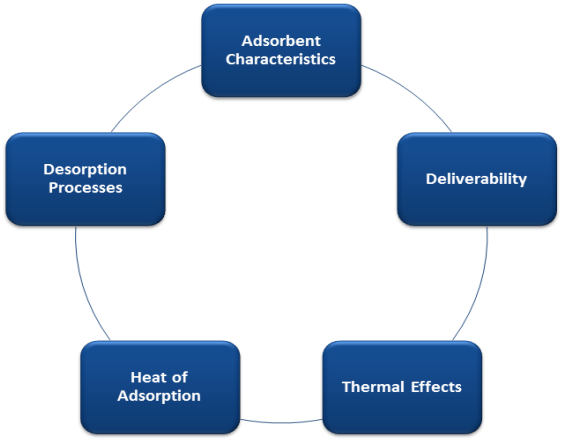

Figure 1.7 The important factors that lead to successful ANG systems. Adapted from Alhasan *et al.*[86]

Chang and Talu[87] have shown the importance of managing thermal effects during the sorption process since temperature changes affect the working capacity of the material (Figure 1.8). A temperature increase during adsorption may reduce the sorption capacity of the material, while a temperature decrease during desorption limits the ability of the material to expel the sorbent. Recent studies have shown how to overcome this problem by using the heat expelled in adsorption to promote desorption for regeneration of the material.[87,88]

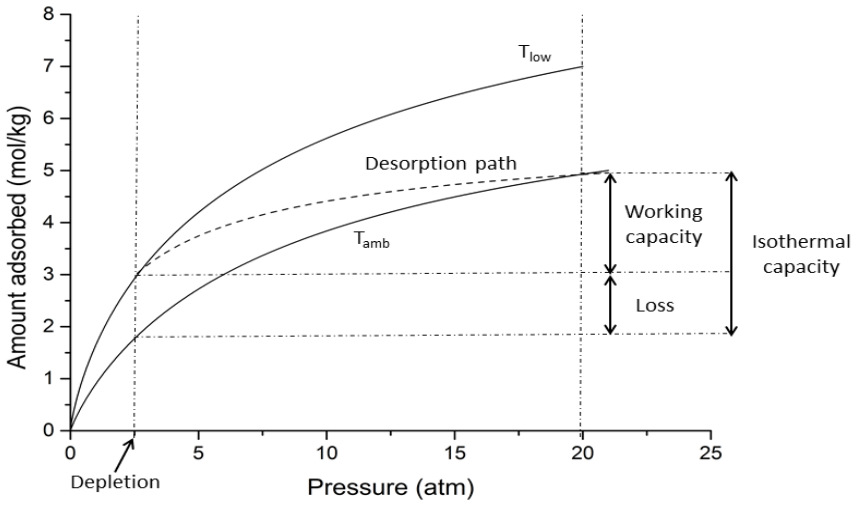

Figure 1.8 An example of the impact that the heat of adsorption has on the capacity of the adsorptive material during the adsorption and desorption processes of ANG systems. The figure is adapted from Chang and Talu.[87]

1.4 Aim of this study

The primary aim of this study is to develop a procedure that can directly determine isosteric heats of sorption using pressure-gradient differential scanning calorimetry (PGDSC) and a suitable test compound (CuHKUST). To show applicability, the procedure was also applied to a different compound that deviates from the classical IUPAC isotherm profiles, a 2D layered PCP with stepped sorption profiles. The overall aim is to show that this method is superior to the commonly used isosteric method that makes use of an approximation rather than employing direct heat measurements.

1.5 Thesis outline

This thesis mainly follows the order in which the aims are presented. The methods and materials used are described in **Chapter 2**. This includes methods to characterise the porous materials used, as well as a detailed description of the instrumentation and method for PGDSC. **Chapter 3** describes the development of the PGDSC Q_{st} method using CuHKUST as the test compound and CO_2 as the test gas. The method is validated by comparing experimental Q_{st} values to the literature values obtained using the isosteric method as well as from calorimetry. Both the isosteric method and PGDSC method are applied to the data for comparative purposes. **Chapter 4** describes the determination of Q_{st} for the 2D $[Cd(oba)(bpy)]_n$, to show applicability to other types of sorption profiles. This compound shows large amounts of hysteresis with three different gases, N_2, CO_2 and CH_4, as well as stepped sorption that is associated with structural changes. Q_{st} curves are determined over a range of pressures, including pressure ranges where structural transformations take place. Summary and concluding remarks for this study are presented in **Chapter 5**.

1.6 References

1 P. B. Venuto, *Microporous Mater.*, 1994, **2**, 297–411.

2 D. M. D'Alessandro, B. Smit and J. R. Long, *Angew. Chem. Int. Ed.*, 2010, **49**, 6058–6082.

3 S. Kitagawa, R. Kitaura and S. Noro, *Angew. Chem. Int. Ed.*, 2004, **43**, 2334–2375.

4 J. V. Smith, *Chem. Rev.*, 1988, **88**, 149–182.

5 S. Wang and Y. Peng, *Chem. Eng. J.*, 2010, **156**, 11–24.

6 de S. C. Deville, *C. R. Hebd. Seances Acad. Sci.*, 1862, **54**, 324–324.

7 K. Biradha, A. Ramanan and J. J. Vittal, *Cryst. Growth Des.*, 2009, **9**, 2969–2970.

8 J. W. Steed and J. L. Atwood, *Supramolecular Chemistry*, Wiley, Winchester, UK, Second Ed., 2009.

9 K. A. Hofmann and F. Küspert, *Z. Anorg. Chem*, 1897, **15**, 204–207.

10 H. M. Powell and J. H. Rayner, *Nature*, 1949, **163**, 566–567.

11 B. F. Hoskins and R. Robson, *J. Am. Chem. Soc.*, 1990, **112**, 1546–1554.

12 O. M. Yaghi, D. A. Richardson, G. Li, C. E. Davis and T. L. Groy, *Mat. Res. Soc. Symp. Proc.*, 1995, **371**, 15–19.

13 J. L. C. Rowsell and O. M. Yaghi, *Microporous Mesoporous Mater.*, 2004, **73**, 3–14.

14 O. M. Yaghi, M. O'Keeffe, N. W. Ockwing, H. K. Chae, M. Eddaoudi and J. Kim, *Nature*, 2003, **423**, 705–714.

15 J. Li, J. Sculley and H. Zhou, *Chem. Rev.*, 2012, **112**, 869–932.

16 W. Lu, Z. Wei, Z.-Y. Gu, T.-F. Liu, J. Park, J. Park, J. Tian, M. Zhang, Q. Zhang, T. Gentle III, M. Bosch and H.-C. Zhou, *Chem. Soc. Rev.*, 2014, **43**, 5561–5593.

17 S. R. Batten, N. R. Champness, X.-M. Chen, J. Garcia-Martinez, S. Kitagawa, L. Öhrström, M. O'Keeffe, M. Paik Suh and J. Reedijk, *Pure Appl. Chem.*, 2013, **85**, 1715–1724.

18 H. Li, M. Eddaoudi, M. O'Keeffe and O. M. Yaghi, *Nature*, 1999, **402**, 276–279.

19 O. M. Yaghi, G. Li and H. Li, *Nature*, 1995, **378**, 703–706.

20 S. Horike, S. Shimomura and S. Kitagawa, *Nat. Chem.*, 2009, **1**, 695–704.

21 R. Matsuda, *Nature*, 2014, **509**, 434–435.

22 S. Kitagawa and K. Uemura, *Chem. Soc. Rev.*, 2005, **34**, 109–119.

23 A. J. Fletcher, K. M. Thomas and M. J. Rosseinsky, *J. Solid State Chem.*, 2005, **178**, 2491–2510.

24 H. Aggarwal, R. K. Das, P. M. Bhatt and L. J. Barbour, *Chem. Sci.*, 2015, **6**, 4986–4992.

25 G. Férey and C. Serre, *Chem. Soc. Rev.*, 2009, **38**, 1380–1399.

26 S. Horike, D. Tanaka, K. Nakagawa and S. Kitagawa, *Chem. Commun.*, 2007, 3395–3397.

27 J. E. Warren, C. G. Perkins, K. E. Jelfs, P. Boldrin, P. A. Chater, G. J. Miller, T. D. Manning, M. E. Briggs, K. C. Stylianou, J. B. Claridge and M. J. Rosseinsky, *Angew. Chem. Int. Ed.*, 2014, **53**, 4592–4596.

28 F. Rouquerol, J. Rouquerol and K. Sing, *Adsorption by Powders and Porous Solids*, Academic Press, London, 1999.

29 D. H. Everett, *Pure Appl. Chem.*, 1972, **31**, 1–78.

30 L. J. Barbour, *Chem. Commun.*, 2006, **11**, 1163–1168.

31 L. J. Barbour, D. Das, T. Jacobs, G. O. Lloyd and V. J. Smith, in *Supramolecular Chemistry: From Molecules to Nanomaterials. Vol. 6: Supramolecular Materials Chemistry*, 2011, pp. 2869–2903.

32 D. Li and K. Kaneko, *Chem. Phys. Lett.*, 2001, **335**, 50–56.

33 K. S. . W. Sing, *Adv. Colloid Interface Sci.*, 1998, **76–77**, 3–11.

34 K. S. W. Sing, D. H. Everett, R. A. W. Haul, L. Moscou, R. A. Pierotti, J. Rouquerol and T. Siemieniewska, *Pure*, 1985, **57**, 603–619.

35 O. K. Farha, I. Eryazici, N. C. Jeong, B. G. Hauser, C. E. Wilmer, A. A. Sarjeant, R. Q. Snurr, S. T. Nguyen, A. Ö. Yazaydin and J. T. Hupp, *J. Am. Chem. Soc.*, 2012, **134**, 15016–15021.

36 A. Corma, H. García and F. X. Llabrés i Xamena, *Chem. Rev.*, 2010, **110**, 4606–4655.

37 L. Ma, C. Abney and W. Lin, *Chem. Soc. Rev.*, 2009, **38**, 1248–1256.

38 L. J. Murray, M. Dincă and J. R. Long, *Chem. Soc. Rev.*, 2009, **38**, 1294–1314.

39 D. Zhao, D. Yuan and H.-C. Zhou, *Energy Environ. Sci.*, 2008, **1**, 222–235.

40 G. Férey, C. Serre, T. Devic, G. Maurin, H. Jobic, P. L. Llewellyn, G. De Weireld, A. Vimont, M. Daturi and J.-S. Chang, *Chem. Soc. Rev.*, 2011, **40**, 550–562.

41 J. A. Mason, M. Veenstra and J. R. Long, *Chem. Sci.*, 2014, **5**, 32–51.

42 Y. He, W. Zhou, G. Qian and B. Chen, *Chem. Soc. Rev.*, 2014, **43**, 5657–5678.

43 K. Sun, L. Li, X. Yu, L. Liu, Q. Meng, F. Wang and R. Zhang, *J. Colloid Interface Sci.*, 2017, **486**, 128–135.

44 P. Horcajada, C. Serre, M. Vallet-Regí, M. Sebban, F. Taulelle and G. Férey, *Angew. Chem. Int. Ed.*, 2006, **45**, 5974–5978.

45 Y. Yang, L. Chen, F. Jiang, M. Yu, X. Wan, B. Zhang and M. Hong, *J. Mater. Chem. C*, 2017, **5**, 1981–1989.

46 B. Chen, S. Xiang and G. Qian, *Acc. Chem. Res.*, 2010, **43**, 1115–1124.

47 H. R. Fu and J. Zhang, *Inorg. Chem.*, 2016, **55**, 3928–3932.

48 M. Lusi and L. J. Barbour, *Angew. Chem. Int. Ed.*, 2012, **51**, 3928–3931.

49 B. Chen, C. Liang, J. Yang, D. S. Contreras, Y. L. Clancy, E. B. Lobkovsky, O. M. Yaghi and S. Dai, *Angew. Chem. Int. Ed.*, 2006, **45**, 1390–1393.

50 S. Kitagawa, *Acc. Chem. Res.*, 2017, **50**, 514–516.

51 C. X. Bezuidenhout, V. J. Smith, P. M. Bhatt, C. Esterhuysen and L. J. Barbour, *Angew. Chem. Int. Ed.*, 2015, **54**, 2079–2083.

52 I. Langmuir, *J. Am. Chem. Soc.*, 1916, **38**, 2221–2295.

53 B. P. Bering, M. M. Dubinin and V. V. Serpinsky, *J. Colloid Interface Sci.*, 1972, **38**, 185–194.

54 R. Roque-Malherbe, *Adsorption and diffusion in nanoporous materials*, CRC Press: USA, 2007.

55 S. Brunauer, L. S. Deming, W. E. Deming and E. Teller, *J. Am. Chem. Soc.*, 1940, **62**, 1723–1732.

56 R. Kitaura, K. Seki, G. Akiyama and S. Kitagawa, *Angew. Chem. Int. Ed.*, 2003, **42**, 428–431.

57 A. Kondo, H. Noguchi, L. Carlucci, D. M. Proserpio, G. Ciani, H. Kajiro, T. Ohba, H. Kanoh and K.

Kaneko, *J. Am. Chem. Soc.*, 2007, **129**, 12362–12363.

58 J. Seo, C. Bonneau, R. Matsuda, M. Takata and S. Kitagawa, *J. Am. Chem. Soc.*, 2011, **133**, 9005–9013.

59 Y. Cheng, H. Kajiro, H. Noguchi, A. Kondo, T. Ohba, Y. Hattori, K. Kaneko and H. Kanoh, *Langmuir*, 2011, **27**, 6905–6909.

60 J. Burress, D. Bethea and B. Troub, *Rev. Sci. Instrum.*, 2017, **88**, 539021–539030.

61 J. Rouquerol, D. Avnir, C. W. Fairbridge, D. H. Everett, J. H. Haynes, N. Pernicone, J. D. F. Ramsay, K. S. W. Sing and K. K. Unger, *Pure Appl. Chem.*, 1994, **66**, 1739–1758.

62 G. Della Gatta, *Thermochim. Acta*, 1985, **96**, 349–363.

63 R. Roque-Malherbe, *Microporous Mesoporous Mater.*, 2000, **41**, 227–240.

64 D. Shen, M. Bülow, F. Siperstein, M. Engelhard and A. L. Myers, *Adsorption*, 2000, **6**, 275–286.

65 M. Bowker, *The Basis and Applications of Heterogeneous Catalysis.*, Oxford University Press, New York, 1998.

66 T. Takaishi, *Pure Appl. Chem.*, 1986, **58**, 1375–1382.

67 D. P. van Heerden, Stellenbosch University, 2014.

68 T. Engel and P. Reid, *Thermodynamics, Statistical Thermodynamics, and Kinetics*, Pearson, Third Ed., 2013.

69 P. L. Llewellyn and G. Maurin, in *Introduction to Zeolite Science and Practice*, eds. J. Čejka, H. van Bekkum, A. Corma and F. Schüth, Elsevier B.V., 3rd edn., 2007, vol. 17, pp. 555–610.

70 D. Shen, M. Burlow, F. Siperstein, M. Engelhard and A. L. Myers, *Adsorption*, 2000, **6**, 275–286.

71 N. Bimbo, J. E. Sharpe, V. P. Ting, A. Noguera-Díaz and T. J. Mays, *Adsorption*, 2014, **20**, 373–384.

72 H. Pan, J. A. Ritter and P. B. Balbuena, *Langmuir*, 1998, **14**, 6323–6327.

73 A. Chakraborty, B. B. Saha, I. I. El-Sharkawy, S. Koyama, K. Srinivasan and K. C. Ng, *High Temp. - High Press.*, 2008, **37**, 109–117.

74 D. Bahamon and L. F. Vega, *Chem. Eng. J.*, 2016, **284**, 438–447.

75 W. Zielenkiewicz, *Calorimetry*, Institute of Physical Chemistry of the Polish Academy of Sciences, Warsaw, 2nd edn., 2008.

76 A. F. H. Ward, *Proc. Cambridge Philos. Soc.*, 1930, **26 (2)**, 278–284.

77 J. A. Dunne, R. Mariwala, M. Rao, S. Sircar, R. J. Gorte and A. L. Myers, *Langmuir*, 1996, **12**, 5888–5895.

78 P. L. Llewellyn and G. Maurin, *Comptes Rendus Chim.*, 2005, **8**, 283–302.

79 A. Gupta, J. Lachance, E. D. Sloan and C. A. Koh, *Chem. Eng. Sci.*, 2008, **63**, 5848–5853.

80 W. Zimmermann and J. U. Keller, *Thermochim. Acta*, 2003, **405**, 31–41.

81 S. Sircar, R. Mohr, C. Ristie and M. B. Rao, *J. Phys. Chem. B*, 1999, **103**, 6539–6546.

82 X. D. Yang, Q. R. Zheng, A. Z. Gu and X. S. Lu, *Appl. Therm. Eng.*, 2005, **25**, 591–601.

83 L. W. Wang, R. Z. Wang and R. G. Oliveira, *Renew. Sustain. Energy Rev.*, 2009, **13**, 518–534.

84 F. Jeremias, D. Fröhlich, C. Janiak and S. K. Henninger, *New J. Chem.*, 2014, **38**, 1846–1852.

85 M. F. De Lange, B. L. Van Velzen, C. P. Ottevanger, K. J. F. M. Verouden, L. C. Lin, T. J. H. Vlugt, J. Gascon and F. Kapteijn, *Langmuir*, 2015, **31**, 12783–12796.

86 S. Alhasan, R. Carriveau and D. S.-K. Ting, *Int. J. Environ. Stud.*, 2016, **73**, 343–356.

87 K. J. Chang and O. Talu, *Appl. Therm. Eng.*, 1996, **16**, 359–374.

88 PCT Int. Appl., WO 2016-TR50255, 2017.

Chapter 2 Materials, Methods and Instrumentation

This chapter describes the synthetic methods for CuHKUST or $[Cd(oba)(bpy)]_n$ as well as the analytical techniques used to characterise them. The setup and procedure for the pressure-gradient differential scanning calorimeter (PGDSC) are described in detail.

2.1 Materials

All chemicals used for syntheses were obtained from Sigma Aldrich and used as received with no modification or purification. For all sorption and PGDSC experiments, the materials used were ground to a fine powder.

2.1.1 CuHKUST

CuHKUST[1] (also known as HKUST-1 and $[Cu_3(TMA)_2(H_2O)_3]_n$) was synthesised using a solvothermal method described by Ye and coworkers.[2] $Cu(NO_3)_2 \cdot 3H_2O$ (1.5 mmol, 362.4 mg) was dissolved in 5 ml deionized water and mixed with an ethanolic solution (5 ml) of benzene-1,3,5-tricarboxylic acid (0.83 mmol, 174.4 mg, TMA). The mixture was heated in a glass autoclave at 120 °C for 24 hours and allowed to cool (spontaneously) to room temperature. The resultant blue powder was washed several times with water followed by ethanol and dried (activated) overnight at 110 °C under dynamic vacuum. The process of activation (desolvation) produced a colour change from light blue to dark purple.

2.1.2 $[Cd(oba)(bpy)]_n$

$[Cd(oba)(bpy)]_n$ was synthesised using the solvothermal method laid out by Nakagawa *et al.*[3] In a glass autoclave the following were added to 10 ml dimethylformamide: 4,4-oxybis(benzoic acid) (0.5 mmol, 129.12 mg, oba), 4,4'-bipyridine (0.5 mmol, 78.1 mg, bpy) and $Cd(NO_3)_2 \cdot 4H_2O$ (0.5 mmol, 154.2 mg). The mixture was heated to 120 °C for 24 hours and cooled naturally to room temperature (for bulk material) or cooled over 12 hours (to yield single crystals). Activation of the white compound was achieved through heating under dynamic vacuum at 150 °C.

2.2 Analytical Instrumentation

2.2.1 Single-crystal X-ray diffraction (SCXRD)

Suitable single crystals of $[Cd(oba)(bpy)]_n$ were isolated and the structure elucidated using SCXRD. This is a non-destructive technique using X-ray radiation to determine the atomic coordinates of compounds in the solid state. The Fourier transform of the measured reciprocal lattice allows for 3D structure determination.

The crystals were immersed in paratone N oil (Exxon),[4] and mounted on a magnetic MiTeGen mount that was placed on a goniometer head. Intensity data were collected on a Bruker SMART APEX-II single-crystal X-ray diffractometer equipped with a CCD (charge coupled device) area-detector using graphite-multilayer-monochromated MoKα radiation (λ = 0.71073 Å, sealed tube) and an Oxford Cryosystems 700 Plus cryostat allowing for low temperature collections (100 ± 2 K). Both ϕ (phi) and ω (omega) scans were recorded.

Data reduction was carried out by means of the standard procedure using the Bruker software package SAINT[5] and absorption correction and the correction of other systematic errors was performed using SADABS[6] within APEX3.[7] The structures were solved by direct methods using SHELXS[8] or SHELXT[9] and refined using SHELXL[10]. X-Seed[11,12] was used as the graphical interface for the SHELX program suite, which was used to solve the crystal structures by direct methods and for refinement by means of least-squares minimisation. Hydrogen atoms were placed using riding model constraints.

PLATON SQUEEZE[13] was used to determine how many electrons are within the crystal structure voids after all modelling had taken place. The technique was used on $[Cd(oba)(bpy)]_n$ SXRD data to determine the total electron count per unit cell of DMF molecules within the PCP. High quality data including high and low angle reflections are required for accurate results. If there are residual electron density peaks still present, particularly around a metal centre or disordered structures, the electron count will not accurately represent the guest molecules.

2.2.2 Powder X-ray diffraction (PXRD)

PXRD is a non-destructive technique that can be used as both a structure determining method and a "fingerprint" tool. It is useful for monitoring phase changes occurring under particular conditions of temperature and pressure. In this study it is mainly used to confirm the identity and purity of the bulk material.

PXRD was carried out on a Bruker D2 PHASER equipped with a Lynxeye 1D detector and Ni-filtered Cu Kα radiation (λ = 1.5418 Å; 30 kV, 10 mA generator parameters; restricted by a 1.0 mm divergence slit and a 2.5 Soller collimator). All PXRD patterns were recorded at ambient temperature over a scan width of 5 to 40° 2θ in step sizes of 0.016° 2θ. The time per step was 0.5 s.

Pressure-resolved PXRD experiments were carried out on a PANalytical X'pert PRO instrument operating in Bragg-Brentano geometry using Cu Kα radiation (λ = 1.5418 Å, 45 kV and 40 mA). Powdered samples were packed into a 0.3 mm sealed glass capillary attached to an *in-house developed* environmental gas cell.[14] The upper part of the cell is a modified stainless steel barbed fitting (see Figure 2.1) into which a glass capillary is inserted and fixed using an epoxy resin. The base, a nickel-coated brass cell, contains the valve that allows for gas loading and evacuation. Figure 2.1 depicts an example of the gas cell with a single crystal loaded in a Lindemann glass capillary. For powder X-ray diffraction, the capillary was approximately 4.5 cm in length and packed with the powdered material. The gas cell is mounted on a standard goniometer head, which is attached to a capillary spinner. The capillary is capable of withstanding gas pressures up to 80 bar and is also suitable for high vacuum experiments. Intensity data were collected in the range of 5 to 40° 2θ at room temperature. A step size of 0.017° 2θ was used with 0.8 s per step. A pressure range spanning vacuum (1.50 x 10^{-3} mbar) to 30 bar of CO_2 gas pressure was used for $[Cd(oba)(bpy)]_n$.

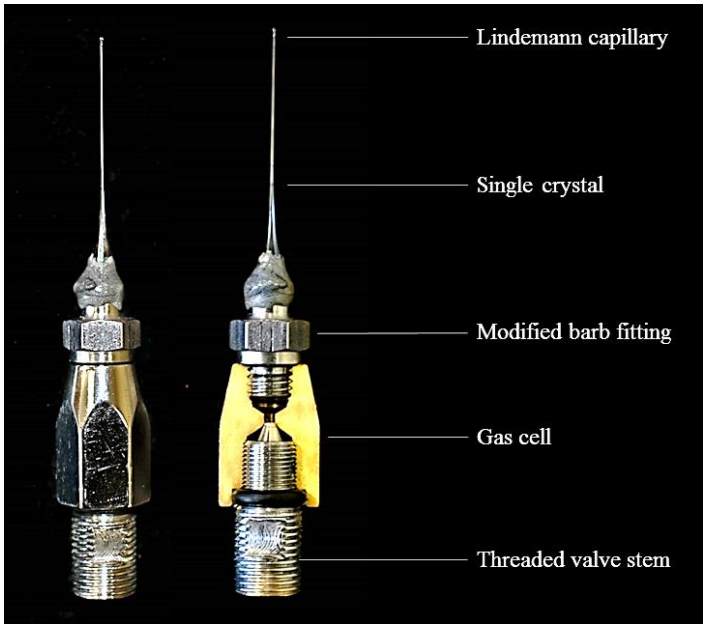

Figure 2.1 Environmental gas cell developed by Barbour.[14] The single-crystal version is shown here. The picture is adapted from a manuscript in progress authored by V.I. Nikolayenko, L. J. Barbour and D. de Villiers.

2.2.3 Thermogravimetric analysis (TGA)

TGA provides information about the compound's thermal stability, as it records mass loss as a function of temperature. It can be used to determine the temperature of desolvation and degradation (decomposition) of the compound. After desolvation, TGA is used to ensure complete solvent removal and assess thermal stability.

Thermogravimetric data were collected on a TA Instruments Q500 analyser. In a typical experiment, between 3-5 mg of sample is placed in an aluminium pan and the temperature is ramped up at 10 K/min under nitrogen gas flow of 50 ml/min from room temperature to 600 °C.

2.2.4 Mercury

Mercury[15,16] is a useful tool for structure visualisation and analysis. Simulated PXRD patterns can be generated from structural data which can be manually compared to experimental patterns to ensure phase purity. Another useful tool of Mercury is the surface mapping function using a spherical probe. Two options are available: a) solvent accessible volume and b) contact surface volume. Solvent accessible volume makes use of the centre of the probe as a reference point which will result in mapped space that reflects where solvent molecules (similar in size to the probe) can gain access. The contact surface volume, on the other hand, maps the surface of the voids by rolling the outer surface of the probe along the structure surface which will reflect the total void space in the structure. The solvent accessible volume will always be smaller than the contact surface volume but both properties are highly dependent on the probe size used. A default of 1.4 Å was used.

2.2.5 Volumetric gas sorption

Volumetric gas sorption was carried out using a Setaram PCTPro-E&E gas sorption analyser with a MicroDoser attachment. Test gases used in this study include: CO_2, N_2, CH_4, C_2H_6 and C_3H_8. Sample masses for gas sorption ranged between 60-100 mg.

A reservoir with a set pressure and known volume is connected to a sample holder with a known pressure and volume separated from each other by a valve. Once the valve is opened, the sample system is allowed to equilibrate. The difference in measured pressure, after equilibration, and predicted pressure, based on no sorption occurring in the sample holder, is used to determine how much gas is adsorbed. The thermodynamic corrections were calculated using NIST (National Institute of Standards and Technology) software to account for non-ideal gas behaviour at high pressures. Blank experiments are run for each gas to compensate for any systematic errors. This system has an operating pressure range of vacuum to 200 bar.

Data were collected at a ΔP of 0.1 bar at very low pressure measurements (vacuum to 1 bar), 0.4 bar at higher pressure measurements (1 to 2 bar), and 4 bar for high pressure measurements (2 to 50 bar). ΔP is the step size of the dosage pressure relative to the previous equilibrated pressure point. Samples were first activated *in-situ* using a heating mantle connected to a thermalcouple. The sample temperature during sorption was controlled by immersing the sample holder in anti-freeze liquid regulated by a Grant GD120 thermostat.

2.2.6 Pressure-gradient differential scanning calorimetry (PGDSC)

A conventional differential scanning calorimeter (DSC) provides information about phase changes of a material as a function of temperature and time in an isobaric environment of ambient pressure. Relative to an empty reference cell, it measures the heat flow from or into the sample. This can be endothermic or exothermic. Pressure-gradient differential scanning calorimetry (PGDSC) measures heat flow as a function of pressure and time under isothermal conditions.

PGDSC measurements were carried out using a Setaram μDSC7 Evo module, equipped with a 3D thermocouple sensor, coupled with a Teledyne ISCO 260D syringe pump. A schematic setup is shown in Figure 2.2. The sample is loaded into a high pressure sample holder that can withstand up to 1000 bar inside a thermostated chamber (**5**). The Setaram μDSC7 Evo module has a temperature range from -45 °C to 120 °C. The pressure-time gradient is maintained with the syringe pump (**2**) and is controlled by *in-house developed* software written by Prof L. J. Barbour (**6**). The pressure gradient rate from the pump is manually controlled by feeding in gas flow rates determined using an iterative Excel spread sheet making use of Eq. 2.1 i.e. van der Waals equation of state.[17]

$$\left(P + \frac{n^2 a}{V^2}\right)(V - nb) = nRT \qquad \textbf{Eq. 2.1}$$

where there are two corrective terms. The first ($\frac{n^2 a}{V^2}$), corrects the pressure in the ideal gas equation as it accounts for the attractive intermolecular forces between gas molecules. The *a* term is indicative of the strength

of that interaction. The second corrective term (nb) accounts for the volume of the gas molecules, where b represents the volume per mole of the closely layered gas molecules (almost liquid state).

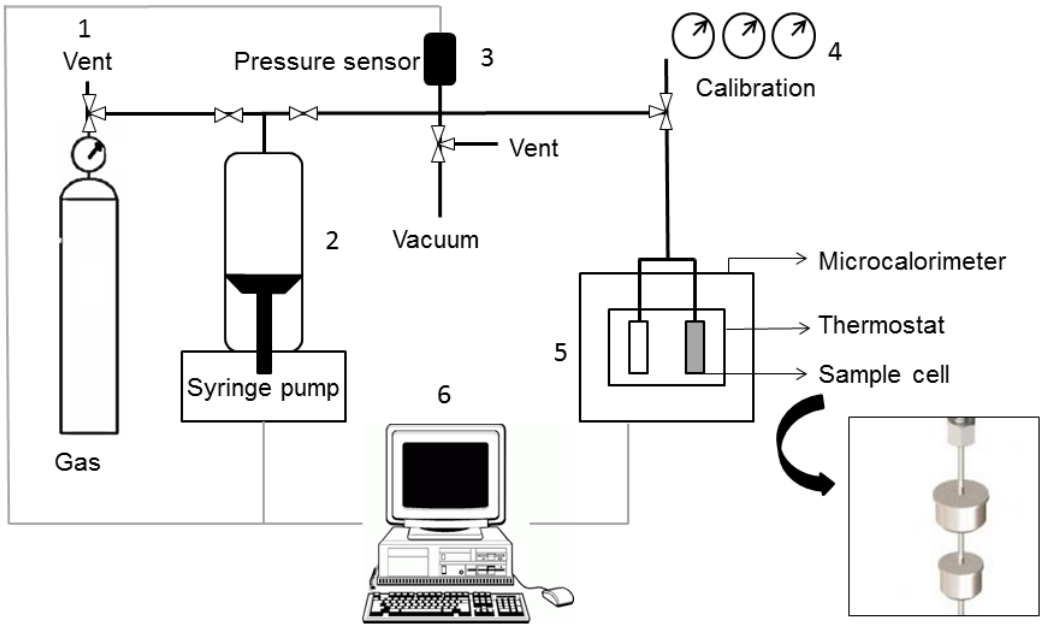

Figure 2.2 Schematic diagram of the PGDSC setup

1 - Gas inlet: controlled by a valve that can be vented to reduce pressure build-up in the system.

2 - Teledyne ISCO 260D syringe pump: responsible for controlling the pressure gradient. Controlled by **6**.

3 - Pressure sensor: allows careful monitoring of pressure readings.

4 - Calibration gauges: for calibrating the pressure sensor to obtain accurate pressure measurements. Calibration is carried out each time a new sample is introduced to the system and when the pressure sensors are changed.

5 - Setaram DSC with a high pressure sample holder: contains a thermostat that allows for isothermal experiments

6 - Computer with data analysing program from Setaram, Calisto: allows data to be saved as a plot of heat flow versus pressure. The pressure-gradient program is controlled here.

Samples were activated *in-situ* in the temperature range of 100-120 °C for 1 hour and left under dynamic vacuum overnight (approximately 12 hours) to ensure the complete removal of water and gas molecules adsorbed during sample loading. The vacuum pressure reached was 6.97 $x10^{-2}$ mbar. After each cycle the samples are activated under the same conditions for 15 minutes. All cycles for a specific temperature are performed within a 24 hour period to avoid errors caused by leakage. Before each cycle the lines are flushed twice with gas to ensure that all residual contaminant gases and impurities are removed; this is especially important for low pressure cycles. The initial pressure is required to be slightly higher than the desired starting pressure as the filling of the lines leading to the sample, as well as adsorption of gas by the sample, causes the

pressure to drop slightly once the sample valve is opened. Once the pressure and temperature are set, the sample is exposed to the pre-set pressure by opening the sample valve and left to equilibrate for approximately 30 minutes. The manual flow-rate program is started once the baseline of the heat flow is stable. After completion of the program, the sample is left for a further 10 minutes to return to its original equilibrium point, after which an activation cycle is run. Specific parameters for each compound and gas are shown in Table 2.1.

Table 2.1 PGDSC program details for CuHKUST and $[Cd(oba)(bpy)]_n$.

Compound	**Gas**	**Pressure range (bar)**	**Pressure Rate (bar/min)**	**Temperature (K)**
CuHKUST	CO_2	0.05-0.35	0.04	288, 298, 308, 318
CuHKUST	CO_2	0.25-2	0.04	288, 298, 308, 318
CuHKUST	CH_4	0.05-0.35	0.04	288, 298, 308, 318
CuHKUST	CH_4	0.25-2	0.04	288, 298, 308, 318
CuHKUST	CH_4	1-50	0.2	288, 298, 308, 318
$[Cd(oba)(bpy)]_n$	CO_2	1-50	0.2/0.3	298
$[Cd(oba)(bpy)]_n$	CH_4	1-50	0.2/0.3	298
$[Cd(oba)(bpy)]_n$	N_2	1-50	0.2/0.3	298

Data were recorded and analysed using the Calisto software package from Setaram and then further reduced and refined along with sorption data using the software package (© OriginLab Corporation, Massachusetts, USA).[18,19]

2.3 Heats of sorption determination

2.3.1 Isosteric method

This method, as outlined in Chapter 1, makes use of the Clausius-Clapeyron approximation to indirectly determine isosteric heat (Q_{st}).

The following expression assumes ideal gas behaviour[17]:

$$\frac{dP}{dT} = \frac{P\Delta H_{vap}}{RT^2} \qquad \textbf{Eq. 2.2}$$

Rearranged:

$$\frac{dP}{P} = \frac{\Delta H_{vap}}{R}\frac{dT}{T^2} \qquad \textbf{Eq. 2.3}$$

Assuming that ΔH_{vap} is constant over the temperature range used, the expression can be integrated:

$$\int \frac{dP}{P} = \int \frac{\Delta H_{vap}}{R}\frac{dT}{T^2} \qquad \textbf{Eq. 2.4}$$

$$lnP = -\frac{\Delta H_{vap}}{R}\frac{1}{T} + C \qquad \textbf{Eq. 2.5}$$

Since:

$$\Delta H_{vap} = -\Delta H_{ads} \sim Q_{st} \qquad \textbf{Eq. 2.6}$$

the following expression is given to determine isosteric heats of sorption as described in Figure 2.3:

$$lnP = \frac{-Q_{st}}{R}\frac{1}{T} + C \qquad \textbf{Eq. 2.7}$$

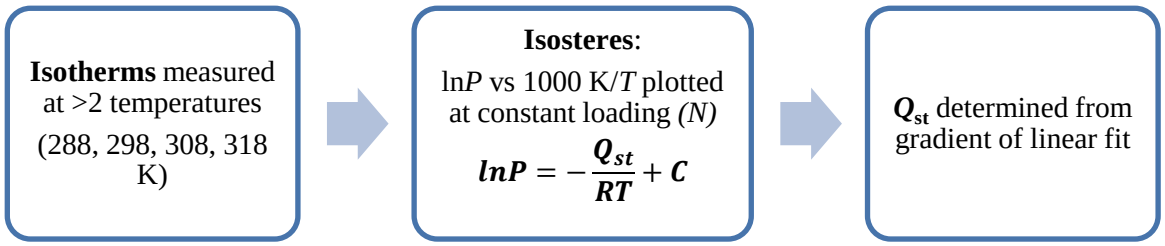

Figure 2.3 Schematic outline of the isosteric method.

To determine Q_{st} in kJ/mol, ln*P* (f/f_0 in Pascal which eliminates the units) is plotted and temperature is plotted as 1000/*T* in Kelvin (K). An Excel function (LINEST) was used to determine the slope (using a best fit line) and the error in the slope. This function calculates the statistics for a straight line using the least-squares method and has an array output with information about that line, including the errors in the slope and intercept.

2.3.2 PGDSC method

The PGDSC method requires one isotherm and one PGDSC experiment at the same temperature. In this study, we show temperature independence by using four temperatures over the same range used in the isosteric method (288, 298, 308, 318 K). The two methods can be compared in this way.

Firstly, the heat flow measured in the PGDSC run is integrated over time to acquire the total heat for the entire sorption process (Q^{int}). This integral heat is differentiated with respect to loading (n), which is extracted from the sorption isotherms, to calculate the differential heat (Q^{diff}). To equate this to isosteric heat, a thermodynamic term must be added: RT.[20–22]

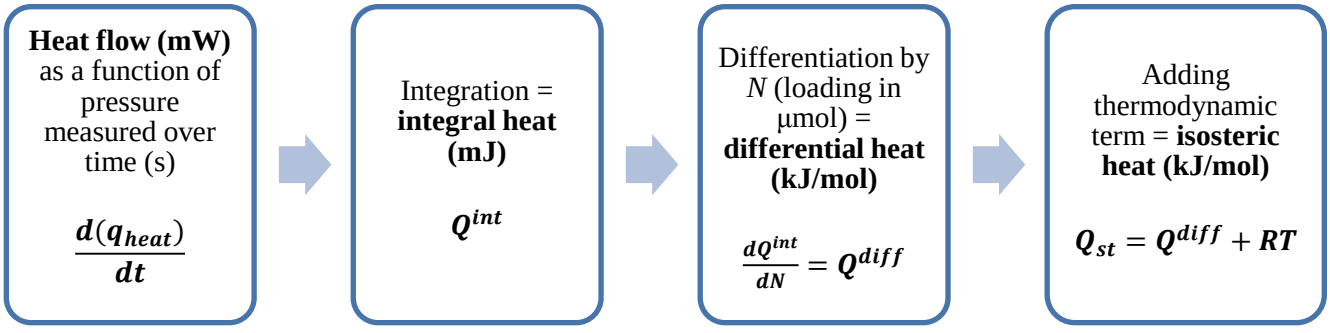

Figure 2.4 Flow chart showing the PGDSC method**.**

2.4 References

1 S. S.-Y. Chui, S. M.-F. Lo, J. P. H. Charmant, A. G. Orpen and I. D. Williams, *Science.*, 1999, **283**, 1148–1150.

2 S. Ye, X. Jiang, L. W. Ruan, B. Liu, Y. M. Wang, J. F. Zhu and L. G. Qiu, *Microporous Mesoporous Mater.*, 2013, **179**, 191–197.

3 K. Nakagawa, D. Tanaka, S. Horike, S. Shimomura, M. Higuchi and S. Kitagawa, *Chem. Commun. (Camb).*, 2010, **46**, 4258–4260.

4 *Paratone N oil*, Exxon Chemical Co.,Texas, USA.

5 *SAINT V8.37A*, Bruker AXS, Inc.: Madison, WI, 2016.

6 *SADABS*, Bruker AXS Inc.:Madison, WI, 2016.

7 *APEX3, SAINT, and SADABS*, Bruker AXS Inc.: Madison, WI, 2016.

8 G. M. Sheldrick, *Acta Crystallogr.*, 2008, **A64**, 112–122.

9 G. M. Sheldrick, *Acta Crystallogr.*, 2015, **A71**, 3–8.

10 G. M. Sheldrick, *Acta Crystallogr.*, 2015, **C71**, 3–8.

11 L. J. Barbour, *J. Supramol. Chem.*, 2001, **1**, 189–191.

12 L. J. Atwood, J. L. and Barbour, *Cryst. Growth Des.*, 2003, **3**, 3–8.

13 A. L. Spek, *Acta Crystallogr. Sect. C Struct. Chem.*, 2015, **71**, 9–18.

14 T. Jacobs, G. O. Lloyd, J. A. Gertenbach, K. K. Müller-Nedebock, C. Esterhuysen and L. J. Barbour, *Angew. Chemie - Int. Ed.*, 2012, **51**, 4913–4916.

15 C. F. Macrae, P. R. Edgington, P. McCabe, E. Pidcock, G. P. Shields, R. Taylor, M. Towler and J. van de Streek, *J. Appl. Crystallogr.*, 2006, **39**, 453–457.

16 C. F. Macrae, I. J. Bruno, J. A. Chisholm, P. R. Edgington, P. McCabe, E. Pidcock, L. Rodriguez-Monge, R. Taylor, J. van de Streek and P. A. Wood, *J. Appl. Crystallogr.*, 2008, **41**, 466–470.

17 T. Engel and P. Reid, *Thermodynamics, Statistical Thermodynamics, and Kinetics*, Pearson, Third Ed., 2013.

18 E. Seifert, *J. Chem. Inf. Model.*, 2014, **54**, 1552–1552.

19 K. J. Stevenson, *J. Am. Chem. Soc.*, 2011, **133**, 5621–5621.

20 D. H. Everett, *Pure Appl. Chem.*, 1972, **31**, 1–78.

21 R. Roque-Malherbe, *Microporous Mesoporous Mater.*, 2000, **41**, 227–240.

22 J. A. Dunne, R. Mariwala, M. Rao, S. Sircar, R. J. Gorte and A. L. Myers, *Langmuir*, 1996, **12**, 5888–5895.

Chapter 3 Development and validation of PGDSC method for direct determination of isosteric heat of sorption: CuHKUST

This chapter outlines the development and validation of the PGDSC method. The procedure is discussed in detail in Chapter 2. Here the results of the PGDSC and isosteric method for Q_{st} determination are presented and discussed through comparison of the two methods. CuHKUST with CO_2 gas was chosen as the test system since CuHKUST is a well-studied compound with many Q_{st} values for CO_2 sorption reported in the literature.

3.1 CuHKUST – The test compound

Chui *et al.* describe the single crystals of CuHKUST to be of octahedral-shape and containing 3D intersecting square-shaped pores with 10 trapped water molecules per formula unit. The framework comprises dimeric copper units with four TMA molecules coordinated through the carboxylate moeity. Two axial water molecules, one coordinated on each metal centre, complete the paddle wheel shown in Figure 3.1 left.[1] The square-shaped micropores have sides measuring between 0.7-0.9 nm.[2] A diagonal view of the packing, [111], shows a large honeycomb arrangement of hexagonal-shaped windows with 1.86 nm between opposite vertices, Figure 3.1 right.[1] The calculated pore volume for this material is 62-72% with a BET surface area of between 800-1500 m^2/g.[3,4] During activation, the guest as well as the axially coordinated water molecules are removed and the compound changes colour from light blue to dark purple. This is a useful indication of activation.

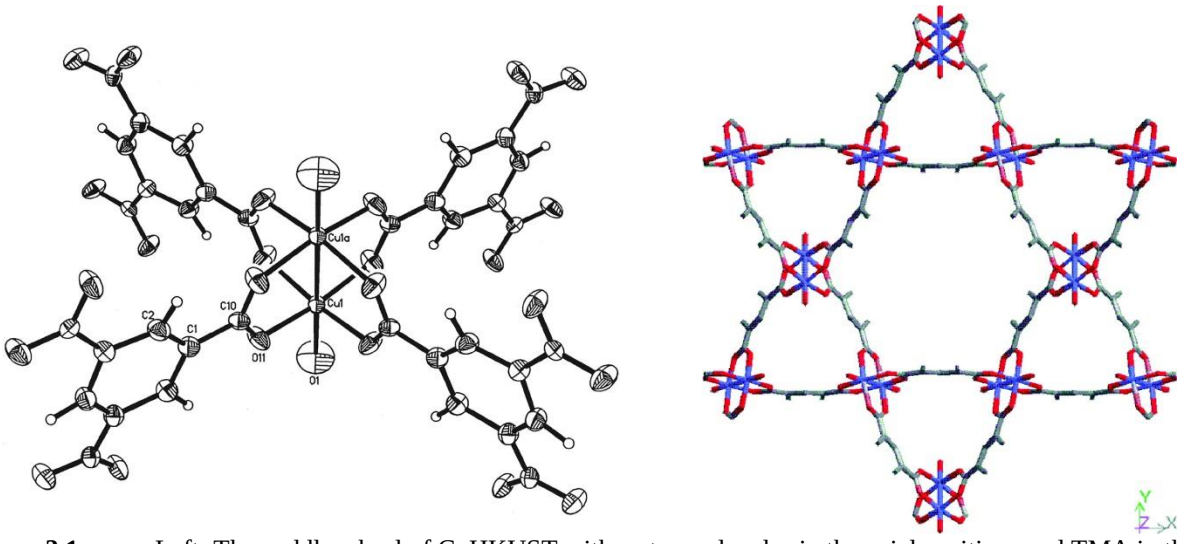

Figure 3.1 Left: The paddle wheel of CuHKUST with water molecules in the axial positions and TMA in the four equatorial positions. Right: Hexagonal windows created by six cupric dimers and six trimesic acid moieties viewed diagonally along the cell body [1 1 1]. Figures taken from Chui *et al.*[1]

Table 3.1 Selected crystallographic data for CuHKUST determined by Chui *et al.*[1]

Formula	$C_{18}H_{12}O_{15}Cu_3$
Molecular mass	658.9 g/mol
Crystal system	Cubic
Space group	$Fm\bar{3}m$
a	26.343(5) Å
V	18280(7) Å^3
Z	16
D_x	0.96 g/cm^3

The coordinated water molecules are removed during activation, resulting in unsaturated copper centres. The unsaturated metal centres are beneficial for CO_2 adsorption due to the quadrupolar nature of CO_2 molecules, which allows strong interactions between the gas molecule and the framework.[4,5] Policicchio *et al.* report that CuHKUST has a working capacity for CO_2 gas of 7.09 mmol/g at 15 bar and 298 K[4] that corresponds to a value of 7.19 mmol/g at 10 Bar and 303 K reported by Ye *et al.*[6]. Another study, by Moellmer *et al.*, reports *ca* 17 mmol/g at 150 bar and 303-343 K; under these conditions the gas can be considered supercritical.[2]

Many values for the heats of CO_2 sorption have been reported for CuHKUST. The majority of studies have utilised the isosteric method. There are large differences between the reported values, illustrated in Figure 3.2. Interestingly there appears to be a correlation between the reported Q_{st} value and the temperature range at which the sorption experiments were carried out; the higher the temperatures in the range used, the higher the Q_{st} value. The difference between the largest and smallest values is 11.75 kJ/mol, which is extraordinarily large for studies of the same system. Specifically, the Q_{st} data tends to be higher for temperature ranges that span temperatures in excess of 298 K. For example, Zhao *et al.*[5] report a Q_{st} value for CuHKUST and CO_2 of 23.2 kJ/mol over the temperature range 273-295 K, whereas Wang *et al.*[7] obtained a value of 35 kJ/mol over the temperature range of 295-423 K for CuHKUST and CO_2. Additional Q_{st} values from the literature for different gases and materials can be found in Appendix A, Figures S1-S8.

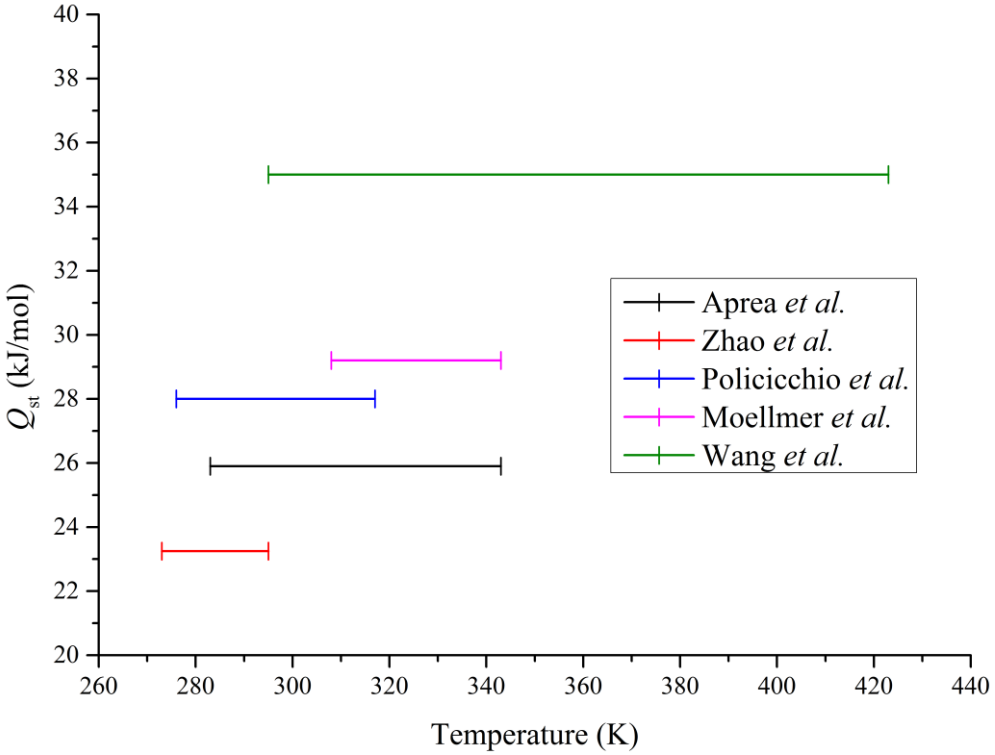

Figure 3.2 Q_{st} values from the literature for CuHKUST with CO_2 gas as a function of the experimental temperature range. All values, except for that from the study by Aprea *et al.*, which is an average for Q_{st} at zero-loading.[2,4,5,7,8]

3.1.1 Characterisation

CuHKUST was characterised by PXRD and TGA to confirm the phase purity of the material. As shown in Figure 3.3, the as-synthesised pattern matches that from the literature.[1] After activation at 120 °C for 12 hours, the material is still crystalline and the diffraction pattern changes only slightly, with a small peak appearing at about 6° 2θ.The differences are likely due to the removal of the coordinated axial water molecules.

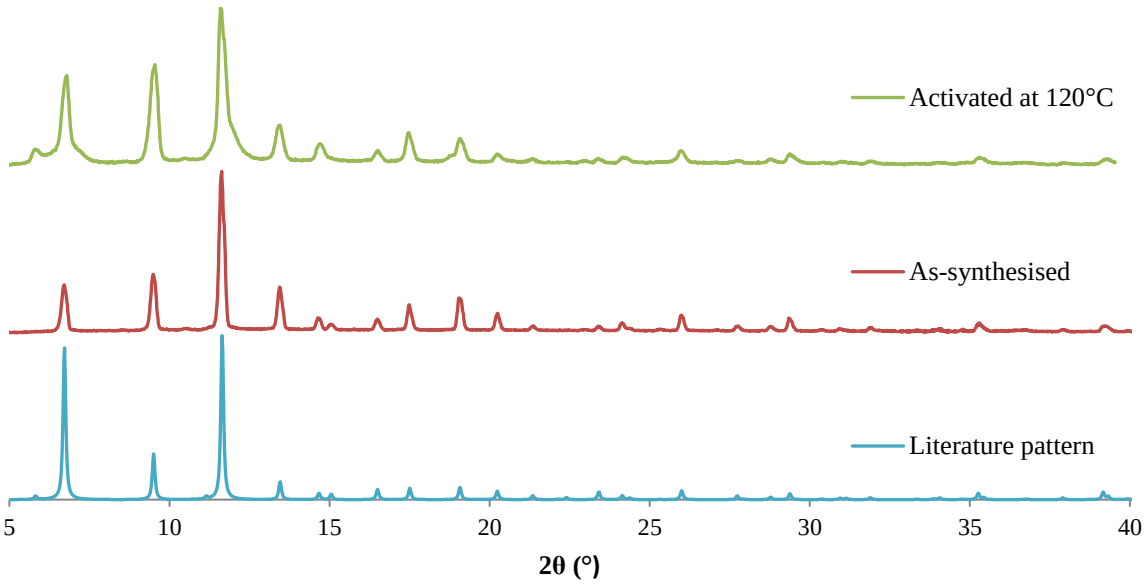

Figure 3.3 PXRD patterns for CuHKUST. **Bottom**: A calculated pattern from the literature.[1] **Middle**: The experimental pattern for the as-synthesised material. **Top**: The experimental pattern for the activated material.

The TGA profile, Figure 3.4, shows that the as-synthesised material loses solvent over a temperature range of 20-90 °C. This includes water molecules, and possibly also ethanol molecules as the % mass loss does not correspond to the expected thirteen water molecules (ten trapped and three coordinated water molecules per formula unit). The % mass loss for the activated material corresponds to 3.5 water molecules which is consistent with the three axially coordinated water molecules, and additional water molecules from the atmosphere, per formula unit. The material rapidly takes up these water molecules from moisture in the air during sample loading, saturating the open metal centres.

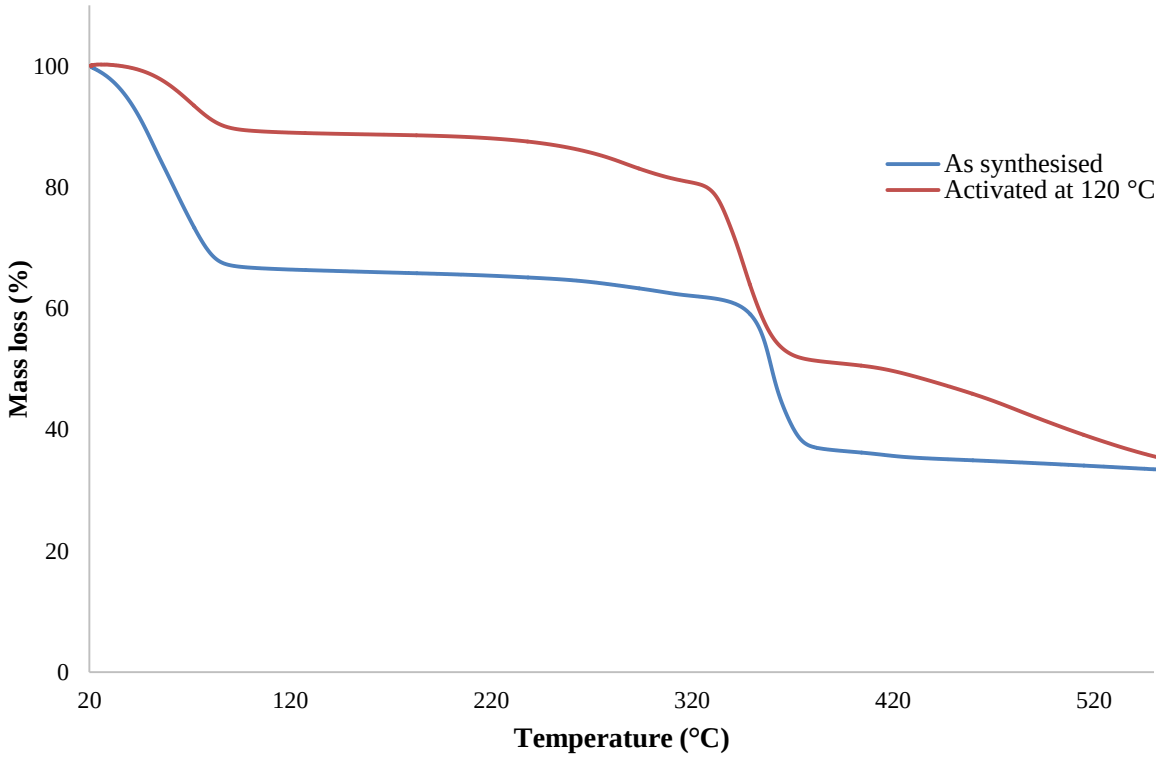

Figure 3.4 TGA profile for CuHKUST showing a % mass loss at 20-90 °C corresponding to a solvent loss consisting of a mixture of water and ethanol molecules (**blue**). Once activated the material only loses approximately three molecules of water per formula unit that coordinate to the open metal centres during sample loading (**red**).

3.2 Results and discussion

Q_{st} is a measurement of magnitude and thus is inherently positive but in this study Q_{st}(sorption) is presented as positive values while Q_{st}(desorption) is presented as negative values. This was only applied for the graph form of the results for easy differentiation between the two sections.

3.2.1 Isosteric method

The following section describes the results from the isosteric method, employing sorption isotherms at four temperatures and then applying the Clausius-Clapeyron approximation. Isosteres have been the preferred method for the determination of Q_{st} for CuHKUST, with many values reported in literature.[2,4,5,7,8] However, the reported values span a range of 11.8 kJ/mol ($23.2 \leq Q_{st} \geq 35$) over different temperature ranges, as mentioned before in Section 3.1. The large deviations within the literature values can be attributed to the assumption that sorption isosteres are linear. If the isosteres are instead curved, there will be different gradients at different points along the curve and thus different Q_{st} values for different temperature ranges. This applies if a line of best fit was not used. If a line of best fit was used then the Q_{st} values obtained will not be an accurate representation.

CuHKUST displays Type I adsorption for CO_2 (Figure 3.5); this profile is well suited for the isosteric method since it is relatively easy to extract relevant data for plotting. Typically, the method requires isotherms recorded at a minimum of two temperatures but in this study the data are based on measurements recorded at

four different temperatures in order to yield statistically reliable results. The isotherms are used to determine equilibrium pressures for each temperature at a specific loading.

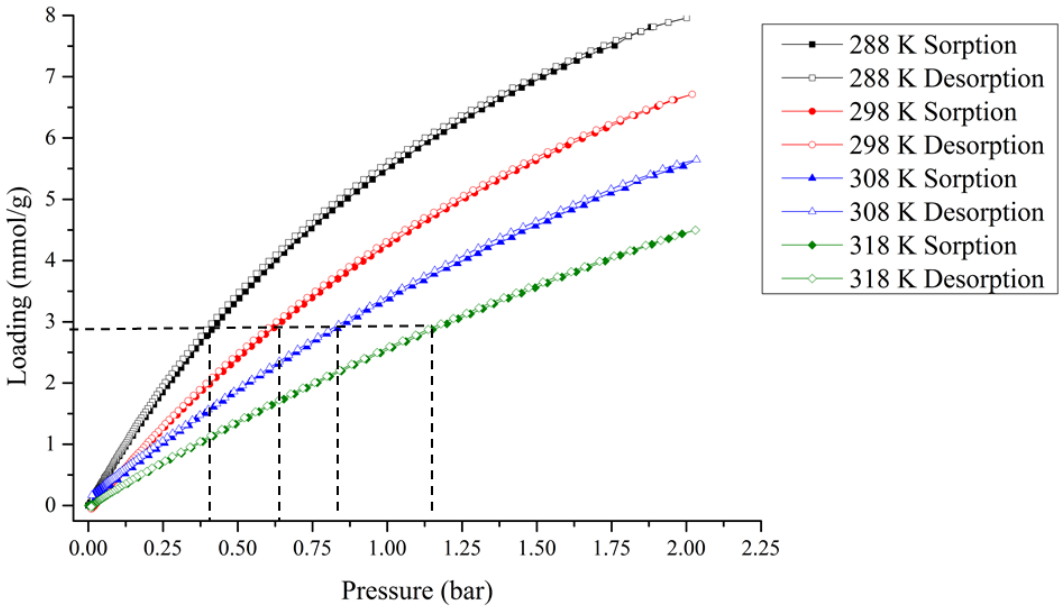

Figure 3.5 CO_2 sorption isotherms for CuHKUST at four temperatures: 288, 298, 308 and 318 K. The dashed lines represent pressure values at constant loading.

Isosteres for specific guest loading (above Figure 3.5) are plotted as ln$P$ as a function of 1000 K/T (pressure in Pa and temperature in K yields Q_{st} in kJ/mol). The temperature unit chosen is to ensure that the end Q_{st} result has units of kJ/mol. Figure 3.6 shows representative isosteres at a selected narrow range of constant loading. The isosteres are not completely linear and thus the gradients of the lines are not uniform over the four temperatures.

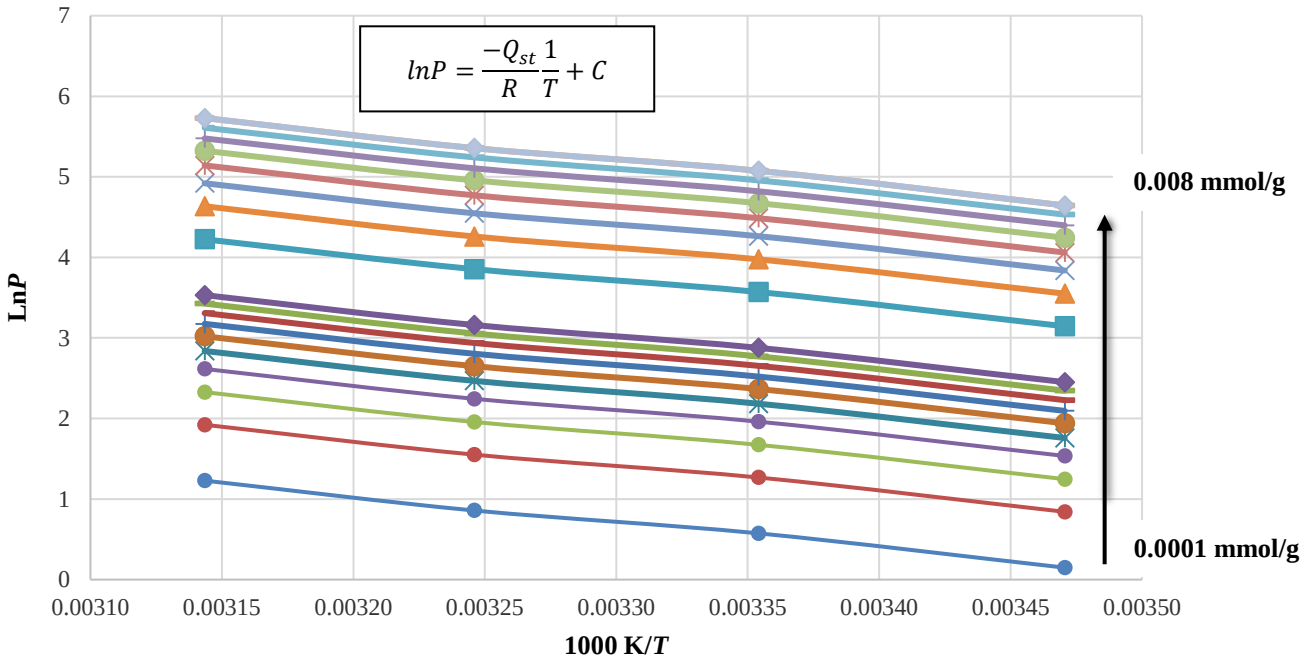

Figure 3.6 CO_2 isosteres (ln*P* vs 1000/*T* at constant loading) for CuHKUST. The gradient is used to determine Q_{st}. The arrow represents incremental increases in loading.

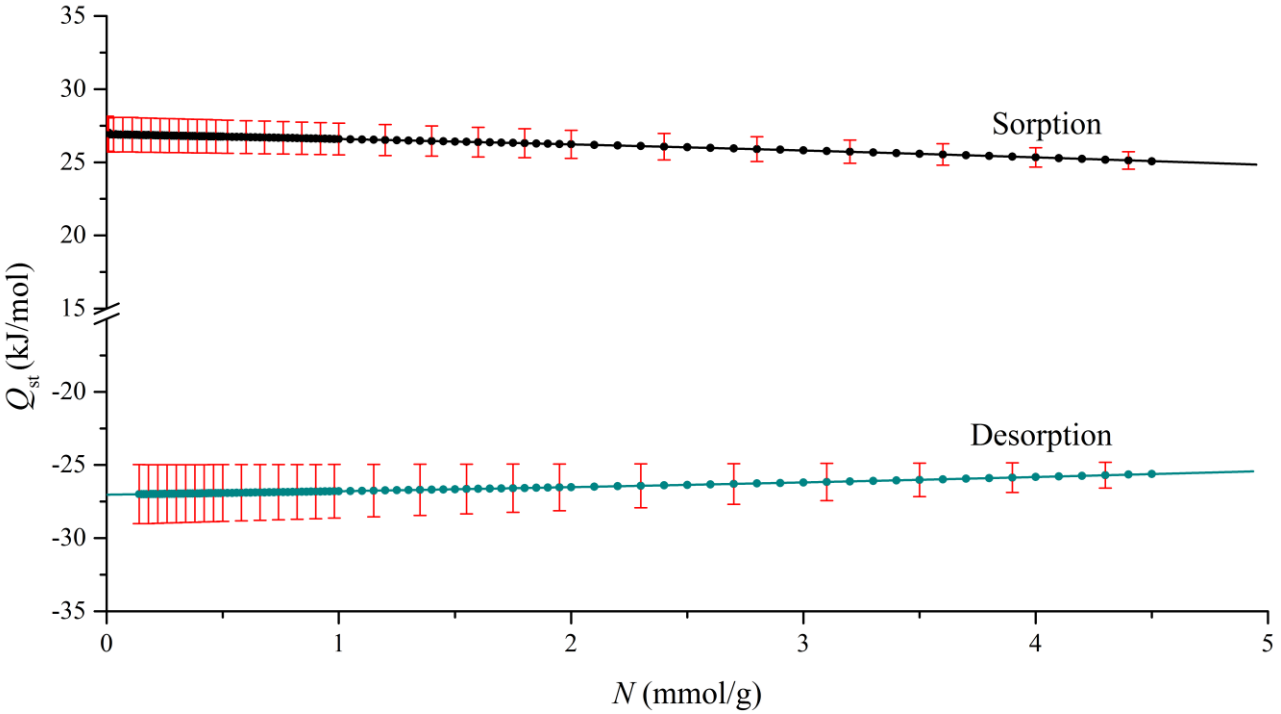

Figure 3.7 Q_{st} curves determined using the isosteric method for CuHKUST with CO_2. Parabolic fitting parameters and statistics can be found in Appendix A, Table S1.

Figure 3.7 shows the Q_{st} curves obtained using the isosteric method. The decreasing trend of the curve with higher loading is typical for a heterogeneous adsorbent surface.[9] If the curve were to trend upwards with increased loading, this would be attributed to "lateral interactions", which are attractive adsorbate-adsorbate interactions.[9] When both a heterogeneous surface and lateral interactions are present that combine to affect the shape of the curve, then a steady trend may be observed.[10–12] However, it is not possible to know if the curve has multiple contributions (from heterogeneous surfaces *and* lateral interactions) or single contributions (heterogeneous surfaces *or* lateral interactions) and that one effect is not masked by the other. It follows that a curve trending downwards does not necessarily mean that there are no lateral interactions present, but merely that the heterogeneous surface contribution is dominant. Conversely, if the curve trends upwards, the dominant lateral interactions overshadow the heterogeneous surface contribution.

The zero-loading values from the isosteric method (taken where the fitted curve crosses the ordinate), compares well with the reported values; 26.91 kJ/mol for sorption and 27.03 kJ/mol for desorption. Conventionally Q_{st} is presented at zero-loading, since there is little contribution from adsorbate-adsorbate (gas-gas) interactions at low loading, so this gives an indication of the interaction between the adsorbate and adsorbent.[10] The error bars shown in Figure 3.7 are errors in the slope of Eq. 2.4 at each point. This was acquired from the LINEST function shown in Eq. 3.5, see Section 3.3.

3.2.2 PGDSC method

The pressure measurements obtained from the PGDSC method require corresponding loading values for the determination of Q_{st}. This is obtained from sorption isotherms; the same isotherms recorded for the isosteric method shown in Figure 3.5. The sorption and desorption curves are separated to allow curve fitting for each section as shown in Figures 3.8 and 3.9. A "find Y from X" function in OriginPro[13] allowed loading to be extracted from the isotherms, similarly to how the pressures were obtained at constant loading in the isosteric method. The fitted curves all have R^2 values above 0.99 (see Figures S2 and S3 in Appendix A) and thus provides reliable loading values from the PGDSC pressure ranges.

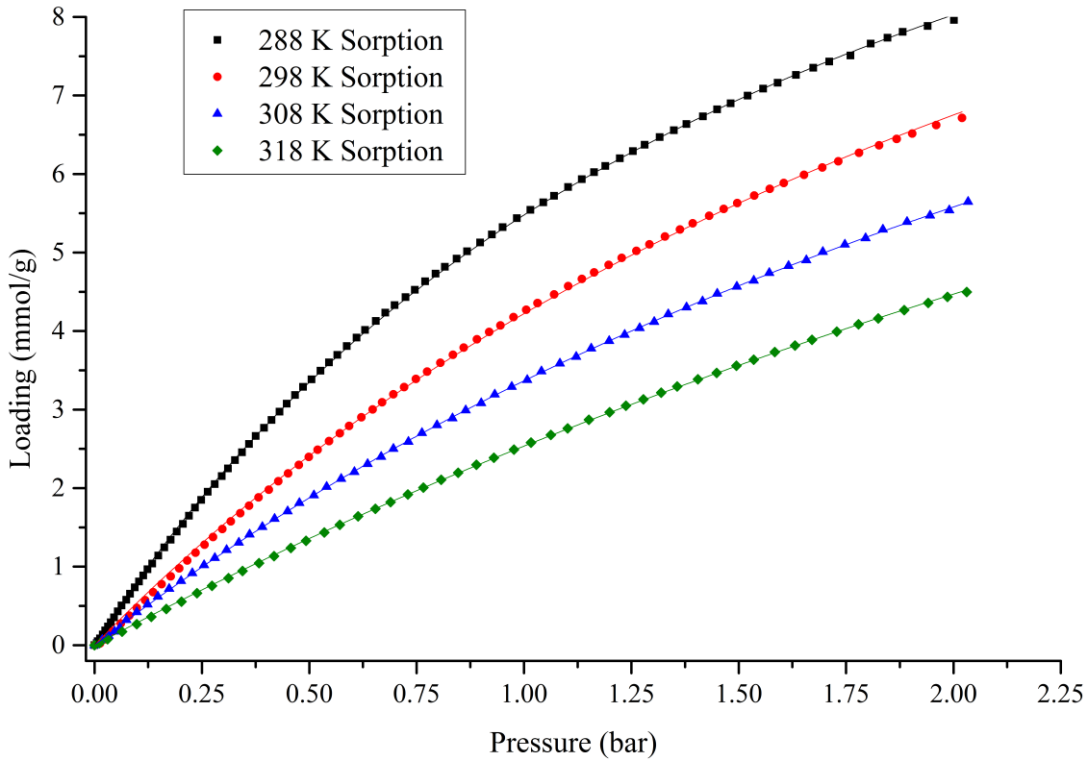

Figure 3.8 CO_2 sorption data for CuHKUST with a scaled Langmuir fit. Fitting parameters and statistics can be found in Appendix A, Table S2.

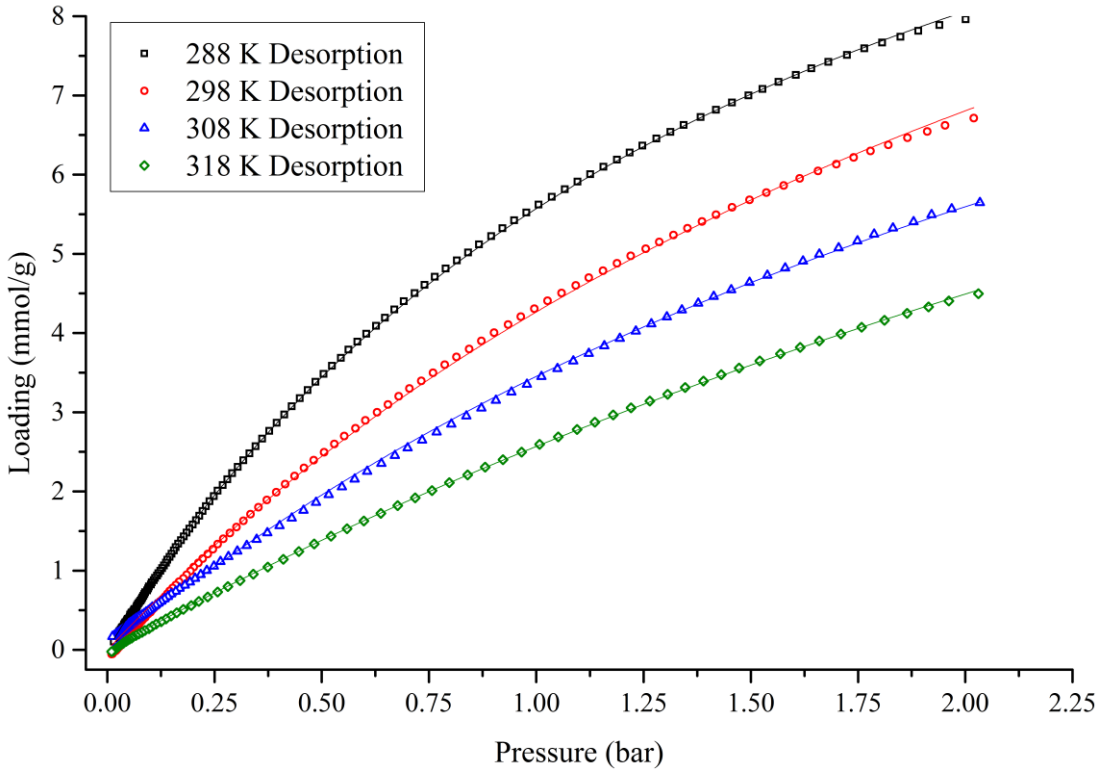

Figure 3.9 CO_2 desorption data for CuHKUST with a scaled Langmuir fit. Fitting parameters and statistics can be found in Appendix A, Table S3.

The heat flow measured with the PGDSC instrument is shown in Figure 3.10 and Figure 3.11. Three PGDSC cycles for each temperature were carried out to prove reproducibility. The three cycles are overlaid for all four temperatures at both pressure ranges (0.05-0.35 bar and 0.25-2.0 bar). The cycles are almost identical at each temperature for the two pressure ranges, showing reproducibility of the heat-flow measurements. At higher temperatures, less heat is released, as expected since the amount of adsorptive taken up decreases with increasing temperature (see Chapter 1, Section 1.2). This is reflected in the integral heat (Q^{int}) curves shown in Figure 3.12. Q^{int} shows the total heat evolved during the whole process of sorption and desorption. This is advantageous for industrial purposes in itself, as the amount of heat involved in the adsorption process affects the temperature of the environment and thus the working capacity of the material.[14] The shapes of the heat flow profiles are consistent with Type I sorption as there are no energetic events besides the steady uptake of gas. Thus the profile is a smooth curve with no sharp peaks in the exothermic (positive axis) or endothermic directions (negative axis).

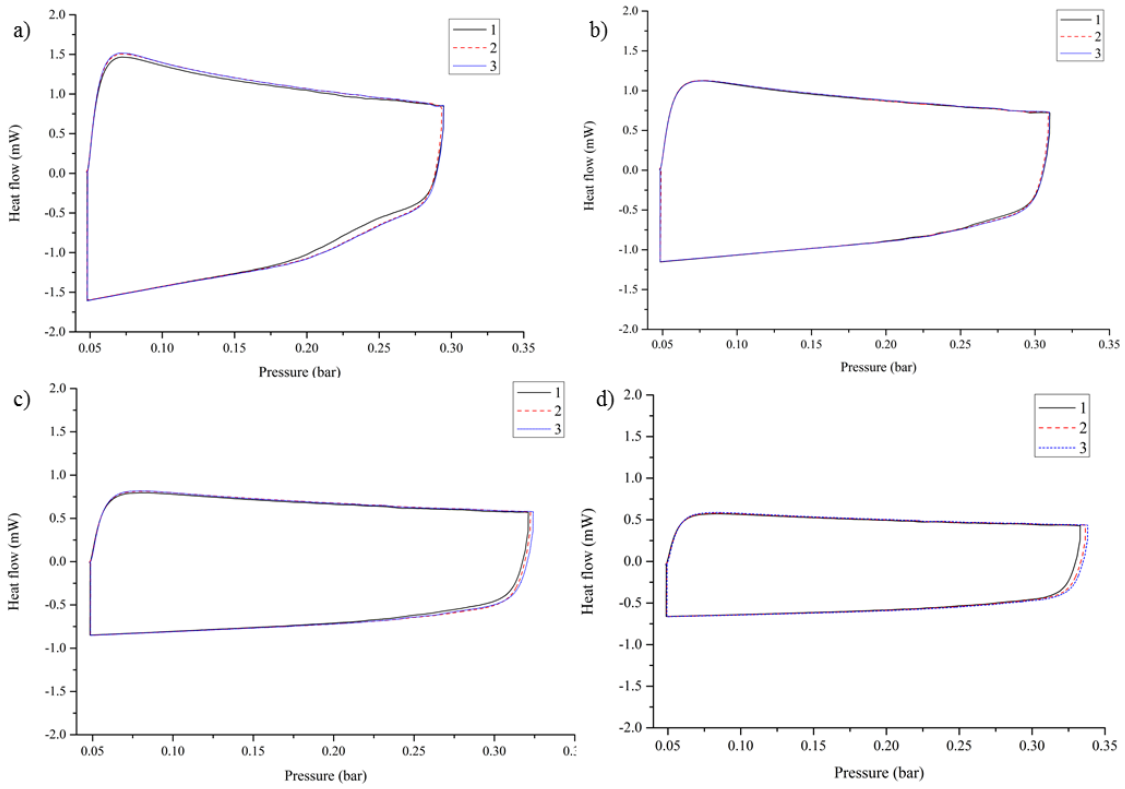

Figure 3.10 Heat-flow curves as a function of pressure for CuHKUST with CO_2 at the selected temperatures: **a)** 288, **b)** 298, **c)** 308 and **d)** 318 K. These experiments were carried out over a pressure range of 0.05-0.35 bar.

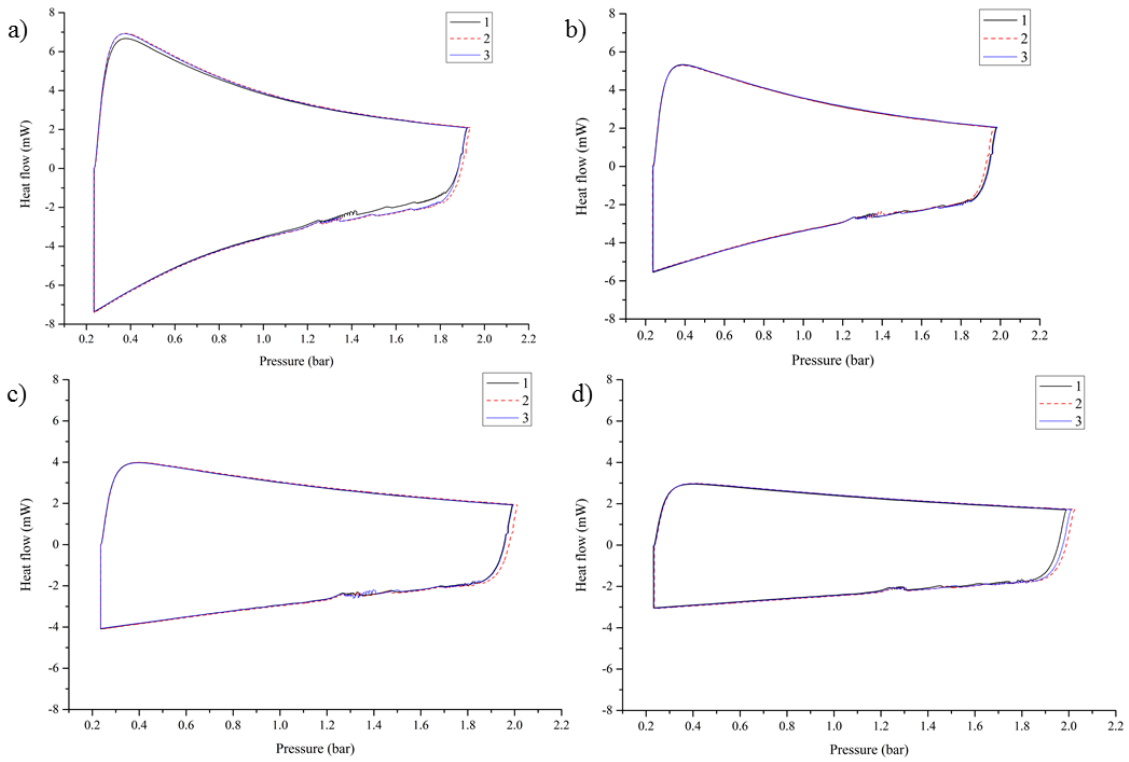

Figure 3.11 Heat-flow curves as a function of pressure for CuHKUST with CO_2 at the selected temperatures: **a)** 288, **b)** 298, **c)** 308 and **d)** 318 K. These experiments were carried out over a pressure range of 0.25-2.0 bar.

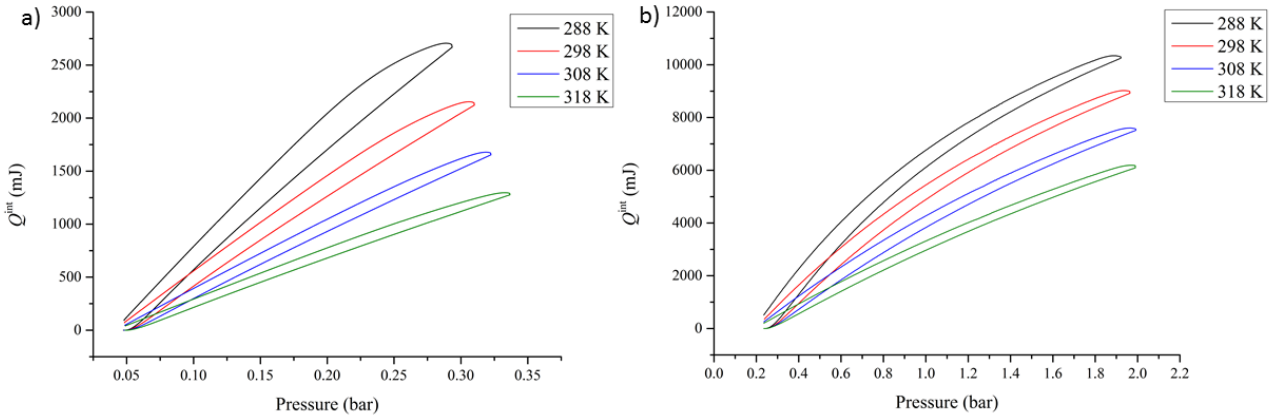

Figure 3.12 Averaged integral heat (Q^{int}) for CuHKUST with CO_2 at 288, 298, 308 and 318 K for both pressure ranges. **a)** 0.05-0.35 bar and **b)** 0.25-2.0 bar.

The averaged integral heats (Q^{int}) from the three cycles are shown in Figure 3.12. To make differentiation possible the sorption and desorption sections are separated. For the range 0.05-0.35 bar, the Q^{int} curves are differentiated (Q^{diff}) as is, without fitting curves to the data, and the thermodynamic term (RT) is added to obtain Q_{st}. The results are shown in Figure 3.13 for sorption and Figure 3.14 for desorption. The sorption Q_{st} curve decreases with increasing loading until it plateaus, whereas the desorption Q_{st} curve has a more linear

shape. The experimental errors are ignored, as explained in Section 3.3, since they are negligible when compared to the averaging error (Figure 3.20 and Figure 3.21).

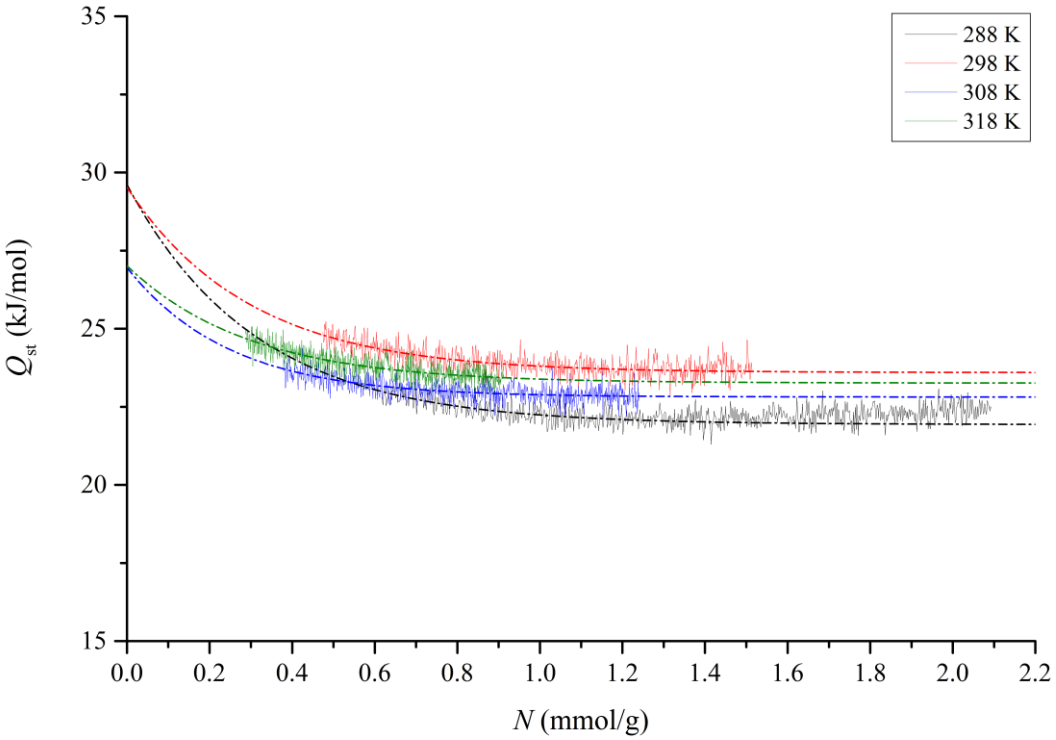

Figure 3.13 Q_{st} curves from the sorption section of the data for each temperature for CuHKUST with CO_2 in the pressure range of 0.05-0.35 bar. The slightly transparent lines represent the experimental data while the dotted lines represent the fitted curve (exponential decay fit). The fitting parameters and statistics can be found in Appendix A, Table S4.

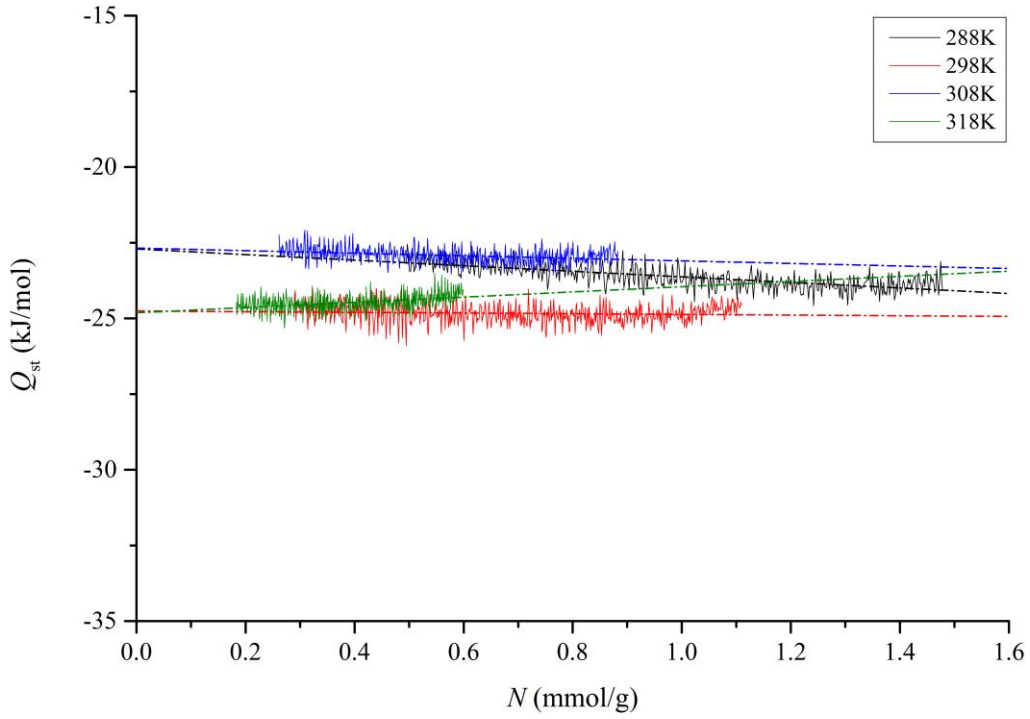

Figure 3.14 Q_{st} curves from the desorption section of the data for each temperature for CuHKUST with CO_2 at a pressure range of 0.05-0.35 bar. The slightly transparent lines represent the experimental data while the dotted lines represent the fitted curve (line fit). The fitting parameters and statistics can be found in Appendix A, Table S5.

For the pressure range 0.25-2.0 bar, a curve was fitted to the Q^{int} data as the unfitted (unsmoothed) data resulted in erratic Q^{diff} curves, Figure 3.15. The fitted curves are used instead of the smoothing functions available in OriginPro, such as the adjacent-averaging method and the Savitzky-Golay method, because these methods do not give representative curves and have a substantial effect on the final Q_{st} results. The resultant Q_{st} curves, using fitted curves for Q^{int}, for each temperature are shown in Figure 3.16 and 3.17. These higher pressures (higher loading) curves are more linear. The Q_{st} curves, both sorption and desorption, for 308 K show an anomalous gradient compared to the other three temperatures. It is unclear why this temperature, specifically, leads to a different result and further investigation needs to be carried out to elucidate the cause.

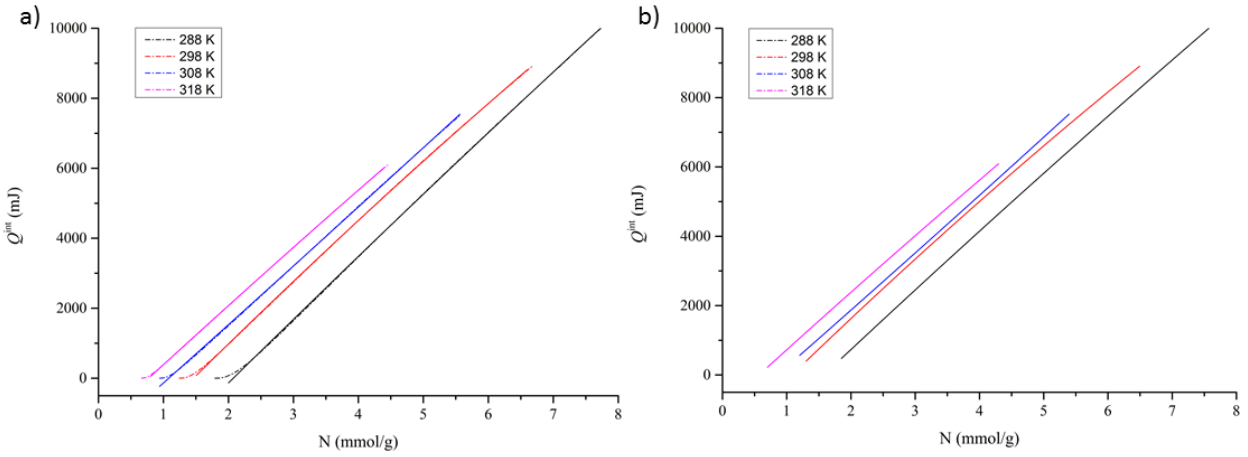

Figure 3.15 Q^{int} data (dotted lines) for the 0.25-2.0 bar pressure range at each temperature with fitted lines (solid colour). a) sorption fitted with a parabola, b) desorption fitted with a parabola. Fitting parameters and statistics can be found in Appendix A, Tables S6 asn S7.

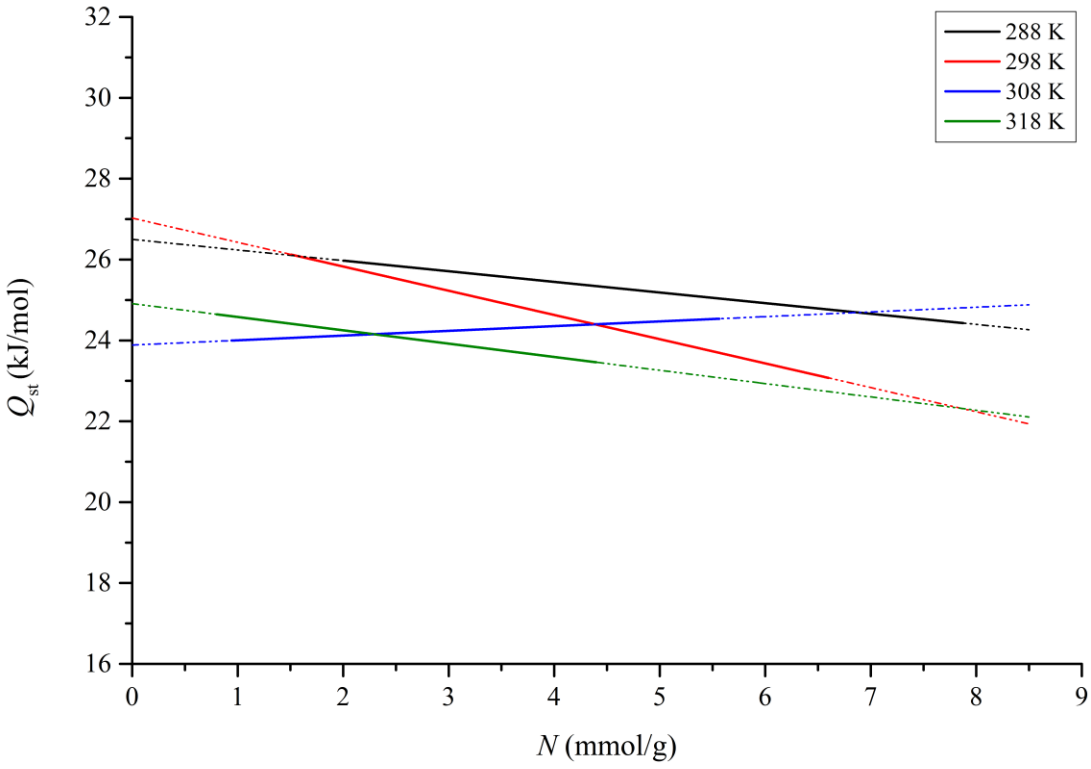

Figure 3.16 Q_{st} curves from the sorption section of the data for each temperature for CuHKUST with CO_2 in the pressure range of 0.25-2.0 bar. The solid line represents the data while the dotted line represents the fitted line (straight line fit). Fitting parameters and statistics can be found in Appendix A, Table S8.

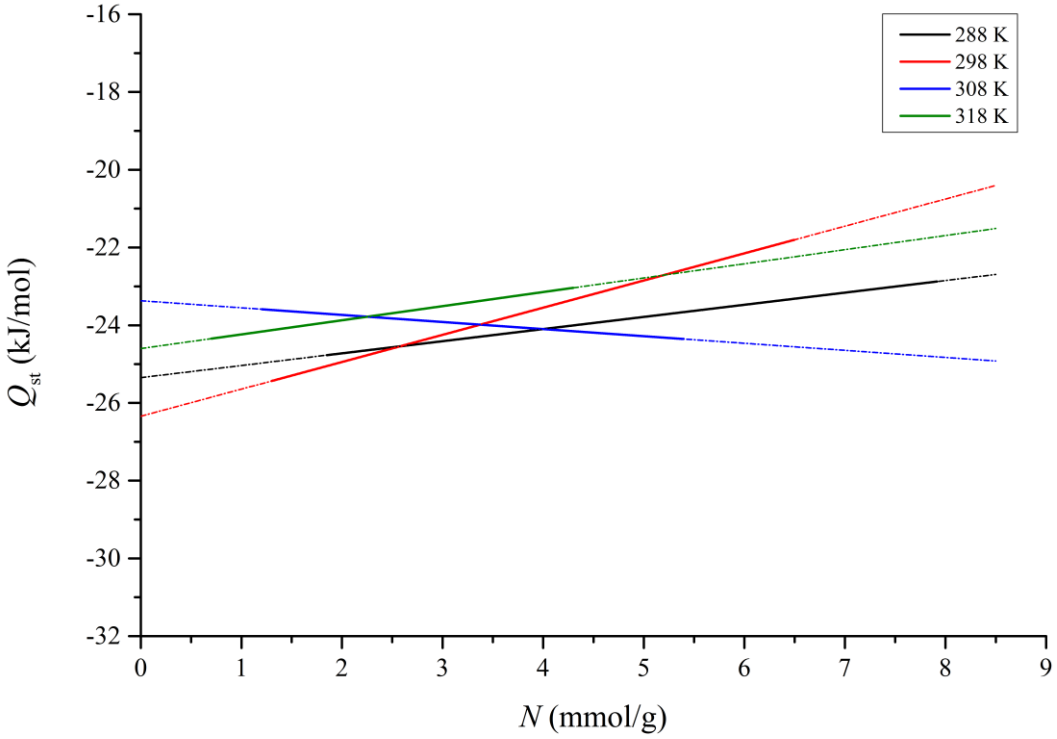

Figure 3.17 Q_{st} curves from the desorption section of the data for each temperature for CuHKUST with CO_2 in the pressure range of 0.25-2.0 bar. The solid line represents the data while the dotted line represents the fitted line (straight line fit). Fitting parameters and statistics can be found in Appendix A, Table S9.

The Q_{st} curves, for both pressure ranges are averaged over the four temperatures and with error bars plotted in Figure 3.18. Figure 3.18 shows the final Q_{st} plots obtained after averaging the data measured at the four temperatures, with the averaging errors shown. The values have relatively small averaging errors, demonstrating that the Q_{st} data obtained using the PGDSC method are temperature independent. The PGDSC Q_{st} data obtained at zero-loading (approximately 24-28 kJ/mol) are within the range of values reported in the literature (isosteric method). The PGDSC Q_{st} data also compare well with the Q_{st} value of 30 kJ/mol obtained from differential thermal analysis (DTA).[15] A conclusion about the influence of temperarture on differential thermal analysis could not be made as the temperature range used was not reported.

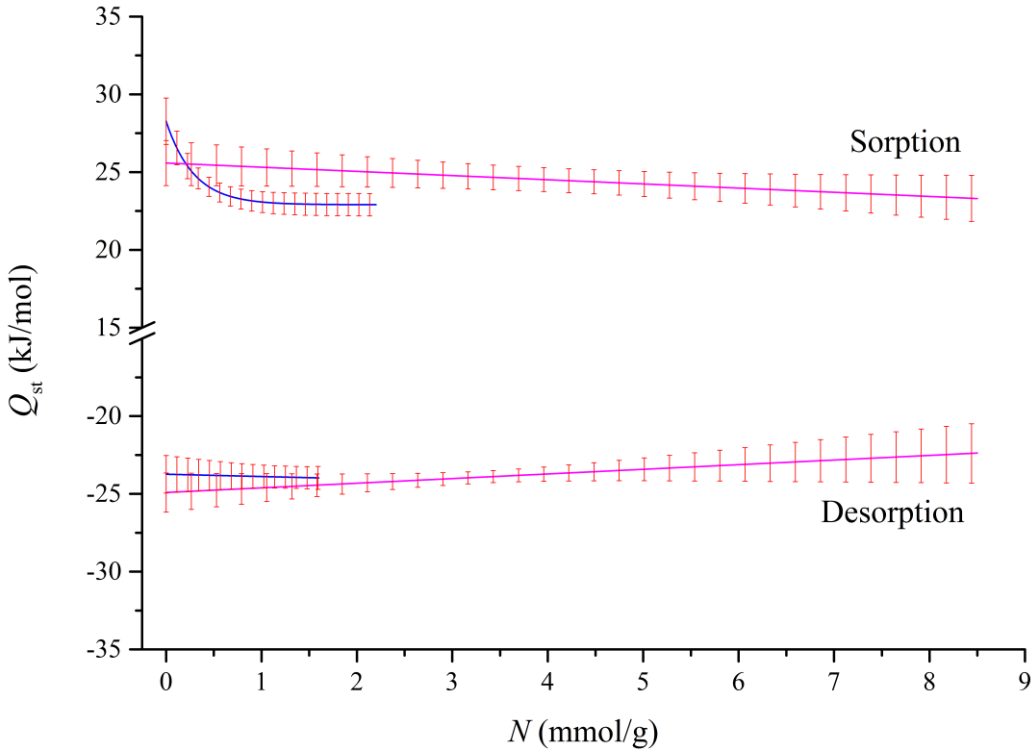

Figure 3.18 Average Q_{st} curves for CuHKUST with CO_2 determined with the PGDSC method with error bars shown in red.

The data obtained from the desorption portion of the PGDSC experiments appear to produce lower Q_{st} values than those from the sorption portion. This may be due to the changeover of the syringe pump when it switches from increasing pressure (compression) to decreasing pressure (expansion), thus preventing the system from returning to the baseline before starting desorption. This affects the total heat measured. Another factor that could influence this difference between the Q_{st} data obtained from sorption and desorption is the minor hysteresis present at very low loading (Figure 3.19). The pathway of sorption at low loading is very slightly different to that for desorption and thus the Q_{st} values will differ slightly at this loading. The two zero-loading Q_{st} values obtained from sorption and desorption sections are different and should be treated as separate values because of this slight hysteresis. The Q_{st} value determined from the sorption section provides thermodynamic information about the uptake process while the value determined from the desorption section pertains to the regeneration of the material as the gas is expelled. The branches of the Q_{st} curve at higher loading for sorption and desorption do, however, compare well.

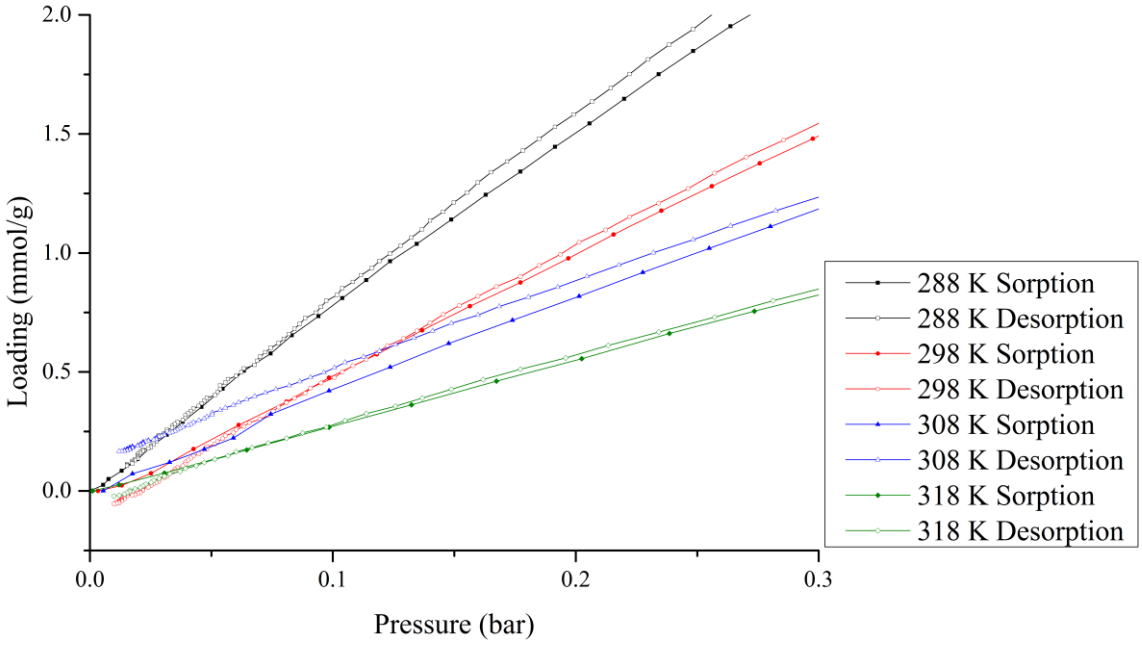

Figure 3.19 Enlarged section of the sorption isotherm for CuHKUST with CO_2 at four temperatures showing slight hysteresis at low pressures (low loading), particularly at 308 K.

3.2.3 Comparison

A summary of the results obtained for both the isosteric and PGDSC methods are presented in Table 3.2; these are compared to the literature values previously reported. The errors associated with the PGDSC Q_{st} values are small (largest = 1.46 kJ/mol). Considering that the differences in literature values obtained using the isosteric method are large (the largest being 11.8 kJ/mol) the PGDSC method appears to produce reliable results.

Although the PGDSC experiments were carried out at multiple temperatures, this is not necessary to obtain a reliable Q_{st} value. The temperature independence of the PGDSC method allows for Q_{st} determination to be achieved with one sorption and one PGDSC experiment carried out at the same temperature. This is less tedious than carrying out multiple sorption experiments at various temperatures, as in the isosteric method. Although it is possible to determine Q_{st} from the isosteric method at just two temperatures, a more reliable result can be obtained at three or more temperatures, which makes the isotherm measurements tedious. There have been considerable advances in calorimeters that have combined instrumentation to allow for simultaneous measurements of adsorption isotherms and heat flow, meaning that future calorimetric experiments may become even simpler.[16]

Table 3.2 Comparison of literature Q_{st} values with experimental values using the isosteric method and calorimetry.

Method		Q_{st} at low loading (kJ/mol)	Temperature range (K)
Isosteric method		23.2[5]	273-295
		25.9 (±0.4)[8[#]]	283-343
		28[4]	276-317
		29.2[2]	308-343
		35[7]	295-423
		26.91[a]	288-318
		27.03[b]	288-318
Calorimetric methods	DTA	30[15 [*]]	not reported
	Low range (PGDSC)	28.27 ± 1.46[a]	288-318
		23.74 ± 1.18[b]	288-318
	High range (PGDSC)	25.58 ± 1.42[a]	288-318
		24.91 ± 1.23[b]	288-318

[#] Average value – Sips parameters used [*] differential thermal analysis (DTA) [a] sorption data. [b] desorption data.

3.3 Error analysis

To obtain the error in the Q_{st} values determined from the isosteric method in Section 3.2.1, the LINEST function in Excel was used. This function returns an array of statistical values describing the slope, including the error in the slope. LINEST uses the following linear regression equations:

$$SSE\ (Sum\ of\ Squares) = \sum_{i}^{N}(y_i - \hat{y}_i)^2 \qquad \textbf{Eq. 3.1}$$

$$SSE = \sum(y_i - \bar{y})^2 - m\sum y_i(x_i - \bar{x}) \qquad \textbf{Eq. 3.2}$$

$$SSE = \sum(y_i - \bar{y})^2 - \frac{(\sum y_i(x_i - \bar{x}))^2}{\sum(x_i - \bar{x})^2} \qquad \textbf{Eq. 3.3}$$

$$SER\ (Standard\ Error\ of\ Regression) = \sqrt{\frac{SSE}{N-2}} \qquad \textbf{Eq. 3.4}$$

$$SE\ (Slope) = \frac{SER}{\sqrt{\sum(x_i - \bar{x})^2}} \qquad \textbf{Eq. 3.5}$$

To assess the experimental error of the PGDSC method in Section 3.2.2, the following error analysis was used. Eq. 3.6 was applied to the error in Q^{int}, obtained from the PGDSC heat flow measurements, and the error in loading (n), obtained from the sorption isotherms.[17]

$$\bar{x} = \bar{x} \pm \frac{z\sigma}{\sqrt{N}} \qquad \textbf{Eq. 3.6}$$

where:

$\bar{x}$ = mean

z = 1.96 (95% confidence interval)

σ = standard deviation

N = sample size (3 since three cycles were carried out at each temperature)

These errors were propagated accordingly:[18]

$$\frac{\Delta Q^{int}}{\Delta n} = Q^{diff} \qquad \textbf{Eq. 3.7}$$

$$\frac{A}{B} = R \qquad \textbf{Eq. 3.8}$$

$$\left(\frac{S_R}{R}\right)^2 = \left(\frac{S_A}{A}\right)^2 + \left(\frac{S_B}{B}\right)^2 \qquad \textbf{Eq. 3.9}$$

where:

S_R = overall experimental error in Q^{diff}

S_A = error in Q^{int}

S_B = error in n

Since

$$Q_{st} = Q^{diff} + RT \qquad \textbf{Eq. 3.10}$$

the experimental error is present in Q^{diff} and this will translate to Q_{st}. The experimental error is negligible compared to the standard deviation from the averaging of Q_{st} values at different temperatures and can thus be ignored when reporting the Q_{st} values. The overall Q_{st} results will be reported with only averaging errors shown.

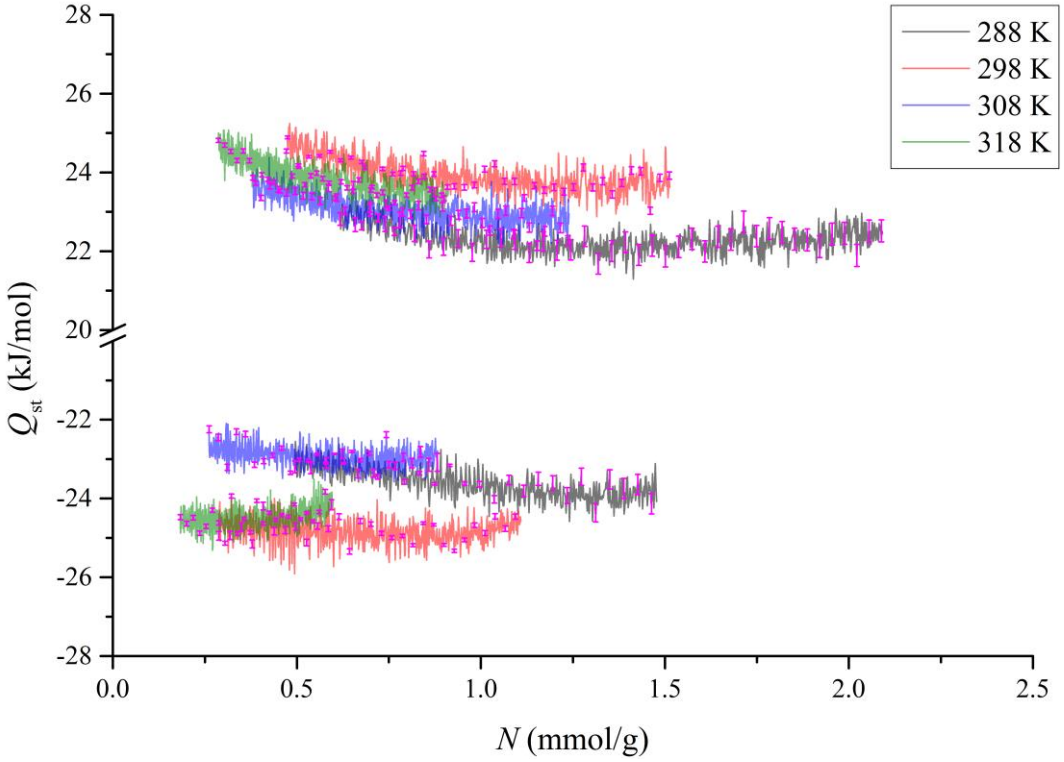

Figure 3.20 Experimental errors for CuHKUST Q_{st} with CO_2 obtained from the PGDSC method for the pressure range of 0.05-0.35.

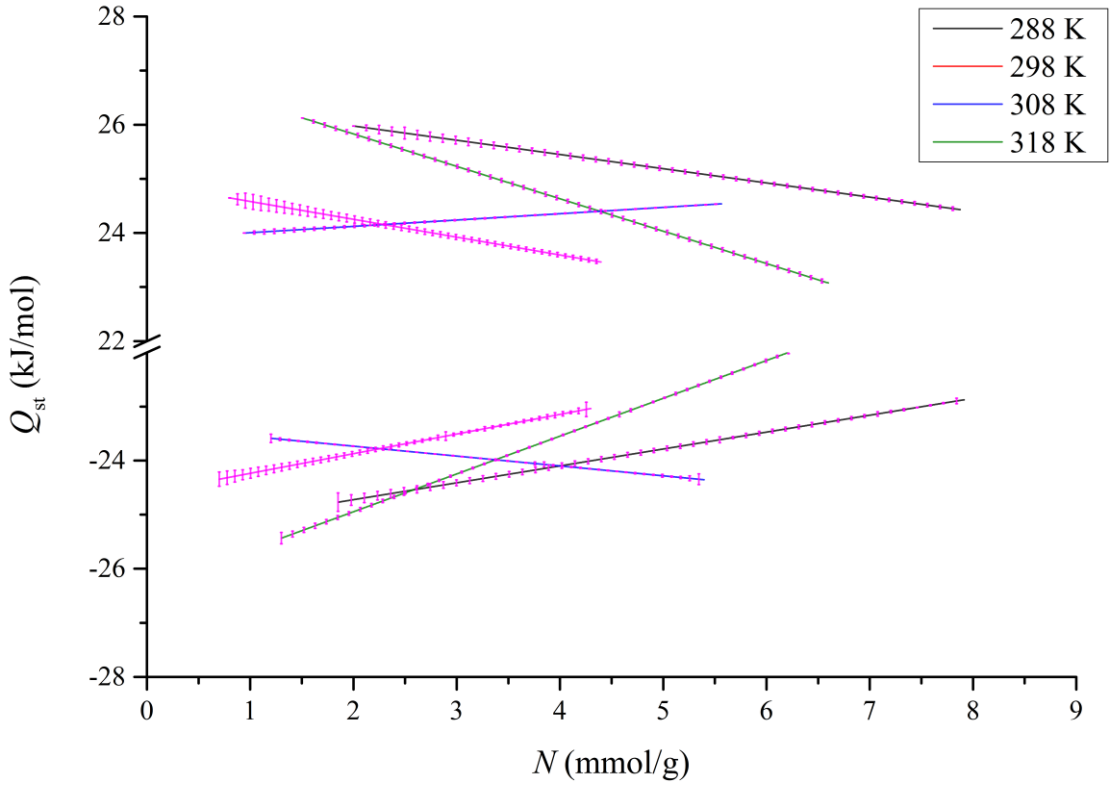

Figure 3.21 Experimental errors for Q_{st} for CuHKUST with CO_2 obtained from the PGDSC method for the pressure range of 0.25-2.0 bar.

3.4 Summary

In conclusion, it has been demonstrated that the PGDSC scanning calorimetric technique produces reliable temperature independent Q_{st} values that compare well with literature values. From the literature data reported for the isosteric method, it appears that a correlation exists between the values obtained for Q_{st} and the temperature range over which the data were measured. Specifically, the Q_{st} values tend to be higher for temperature ranges above 298 K. The PGDSC method uses direct measurement of heat flow whereas the widely used isosteric method yields heat values derived from approximated thermodynamic expressions and the assumption that the bulk gas has ideal behaviour. Moreover, the calorimetric method involves a single sorption isotherm in addition to a single PGDSC experiment to obtain Q_{st} values, as opposed to the multiple sorption isotherms over a range of temperatures for the isosteric method. Future PGDSC measurements could be made even simpler with combined instrumentation. Finally, it is conventional to report Q_{st} at zero-loading as it takes into account only the adsorbent-adsorbate interactions. However, we suggest that it is more suitable, in the industrial context, to report the full Q_{st} data, allowing investigators to have access to the entire loading range as this will provide information about the entire adsorption process. This will allow thermal effects to be managed more effectively in adsorption systems and further improve the working capacity of the porous materials.

3.5 References

1 S. S.-Y. Chui, S. M.-F. Lo, J. P. H. Charmant, A. G. Orpen and I. D. Williams, *Science.*, 1999, **283**, 1148–1150.

2 J. Moellmer, A. Moeller, F. Dreisbach, R. Glaeser and R. Staudt, *Microporous Mesoporous Mater.*, 2011, **138**, 140–148.

3 J. L. C. Rowsell and O. M. Yaghi, *J. Am. Chem. Soc.*, 2006, **128**, 1304–1315.

4 A. Policicchio, Y. Zhao, Q. Zhong, R. Agostino and T. Bandosz, *Appl. Mater. Interfaces*, 2014, **6**, 101–108.

5 Y. Zhao, M. Seredych, J. Jagiello, Q. Zhong and T. J. Bandosz, *Chem. Eng. J.*, 2014, **239**, 399–407.

6 S. Ye, X. Jiang, L. W. Ruan, B. Liu, Y. M. Wang, J. F. Zhu and L. G. Qiu, *Microporous Mesoporous Mater.*, 2013, **179**, 191–197.

7 Q. M. Wang, D. Shen, M. Bülow, M. Ling Lau, S. Deng, F. R. Fitch, N. O. Lemcoff and J. Semanscin, *Microporous Mesoporous Mater.*, 2002, **55**, 217–230.

8 P. Aprea, D. Caputo, N. Gargiulo, F. Iucolano and F. Pepe, *J. Chem. Eng. Data*, 2010, **55**, 3655–3661.

9 A. Chakraborty, B. B. Saha, I. I. El-Sharkawy, S. Koyama, K. Srinivasan and K. C. Ng, *High Temp. - High Press.*, 2008, **37**, 109–117.

10 F. Rouquerol, J. Rouquerol and K. Sing, *Adsorption by Powders and Porous Solids*, Academic Press, London, 1999.

11 M. Suzuki, *Chemical engineering monographs: Adsorption engineering*, Kodansha Ltd., Tokyo, 1990, vol. 25.

12 J. A. Dunne, R. Mariwala, M. Rao, S. Sircar, R. J. Gorte and A. L. Myers, *Langmuir*, 1996, **12**, 5888–5895.

13 E. Seifert, *J. Chem. Inf. Model.*, 2014, **54**, 1552–1552.

14 K. J. Chang and O. Talu, *Appl. Therm. Eng.*, 1996, **16**, 359–374.

15 Z. Liang, M. Marshall and A. L. Chaffee, *Energy and Fuels*, 2009, **23**, 2785–2789.

16 W. Zimmermann and J. U. Keller, *Thermochim. Acta*, 2003, **405**, 31–41.

17 J. P. Holman, *Experimental Methods for Engineers - Internation Edition*, McGraw-Hill, Singapore, 8th edn., 2012.

18 R. A. Day and A. L. Underwood, *Quantitative Analysis*, Prentice-Hall Inc., New Jersey, 4th edn.

Chapter 4 Applying the PGDSC method for the direct determination of isosteric heat to a flexible PCP: $[Cd(oba)(bpy)]_n$

The PGDSC method, validated in Chapter 3 with CuHKUST and CO_2, was applied to a 2D-layered PCP that displays stepped sorption profiles with hysteresis for CO_2, CH_4 and N_2 gases. Some of the characterisation and sorption data presented below formed part of a previous unpublished study.

Soft porous materials (third generation materials) have some flexible properties that depend on the displacement or movement of motifs. The presence of 2D interdigitated layers, in particular, can lead to interesting unconventional sorption properties as the layers can facilitate displacement allowing for guest exchange or uptake (Figure 4.1).[1,2] The literature shows that there are various ways to design interdigitated layers,[3] specifically through the combination of bipyridyl and dicarboxylate ligands with a transition-metal node.[4,5] The use of V-shaped dicarboxylates can lead to the formation of a double chain motif that forms the "digits" of the interdigitation; see the representation in Figure 4.2. The dicarboxylate ligands, as well as the bipyridyl ligands, can take part in π-π stacking between layers to stabilise the structure, but this is not a requirement for interdigitation.[4]

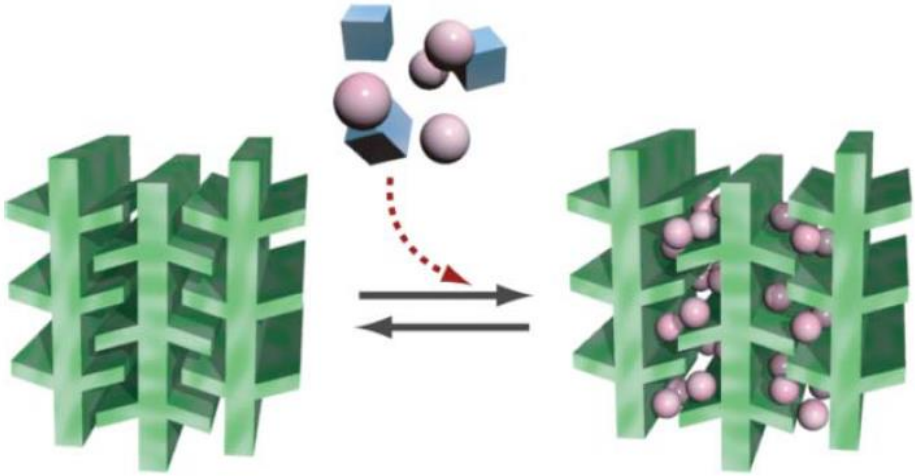

Figure 4.1 Interdigitated 2D layers allow movement of motifs to accommodate guest molecules. Figure adapted from Horike *et al.*[4]

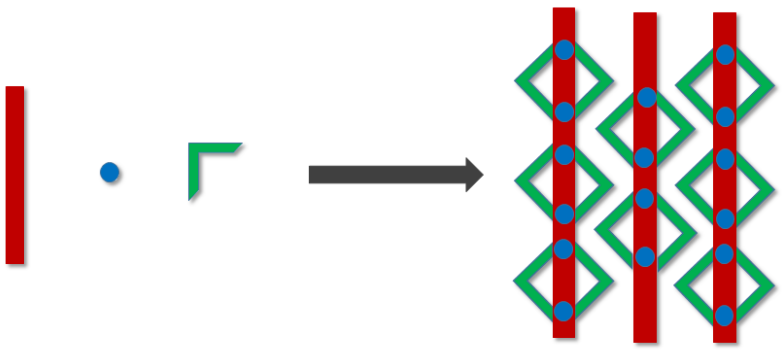

Figure 4.2 Scheme showing how interdigitation occurs with bipyridyl ligands (red rectangles), V-shaped dicarboxylates (green V shape) and metal nodes (blue sphere). This is just a representation; in an actual framework, the dimeric metal nodes will align with the layer extending into the page**.**

[Cd(oba)(bpy)]$_n$ was chosen as a test compound as it exhibits interesting gas sorption profiles, which is an ideal model to apply the PGDSC method to. Synthesis of [Cd(oba)(bpy)]$_n$, or a material with these components, has previously been reported by Ma *et al.*[6] but appears to be a different form than the material in this investigation, as the unit cell parameters from SCXRD do not match (see Table 4.2 at the end of this chapter). The reported structure is described as having 1D chains connected by bipyridyl pillars to form a 3D structure, contrary to the 2D-layered motif observed in this study. This difference in structure can be attributed to the slightly different experimental conditions. Ma *et al.* used a different solvent mixture and higher reaction temperature. The study does not report an activated structure nor any gas sorption results, but does investigate luminescence properties. Thus this material is ideal for sorption property investigation. Materials with motifs similar to that seen in this study have been reported using naphthalene and benzene dicarboxylates and display stepped sorption.[4,7]

4.1 Characterisation

4.1.1 SCXRD

Using single-crystal XRD data, the material was elucidated to be a 2D-layered structure. The ASU for the as-synthesised form (**1a**) is shown in Figure 4.3 with a partially modelled DMF molecule, which is disordered over two positions with a 60:40 occupancy ratio. One-dimensional (1D) double chains are formed by the oba ligands coordinating to the dimeric cadmium metal centres in the equatorial positions, as shown in Figure 4.4a. The bpy ligands act as pillars in the axial positions, creating the 2D layer, as displayed in Figure 4.4b. These layers interdigitate to form the 3D arrangement shown in Figure 4.5. All hydrogen atoms in the figures are omitted for clarity.

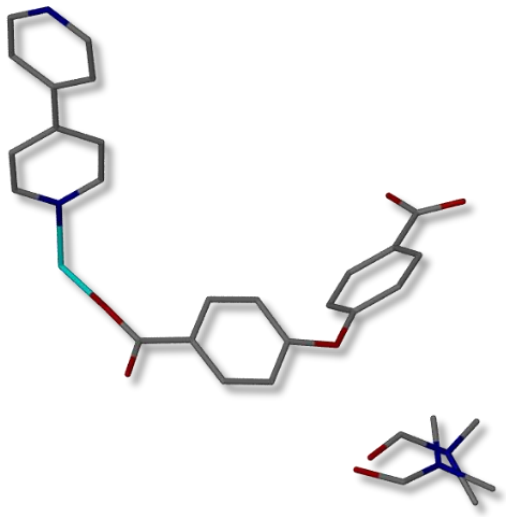

Figure 4.3 ASU of as-synthesised [Cd(oba)(bpy)]$_n$ (**1a**) with the trapped DMF molecule disordered over two positions. SCXRD data were collected at 100 K.

The DMF guest molecules could not be modelled satisfactorily and thus SQUEEZE was applied as an alternative method of interpreting electron density (form **1sq**).[8] The electron count confirms the presence of approximately 1.6 DMF molecules per ASU trapped in the voids, although TGA shows a solvent loss matching 1.16 DMF molecules per ASU. Figure 4.6, where only the major component is shown for clarity, illustrates how the guest DMF molecules arrange in the voids.

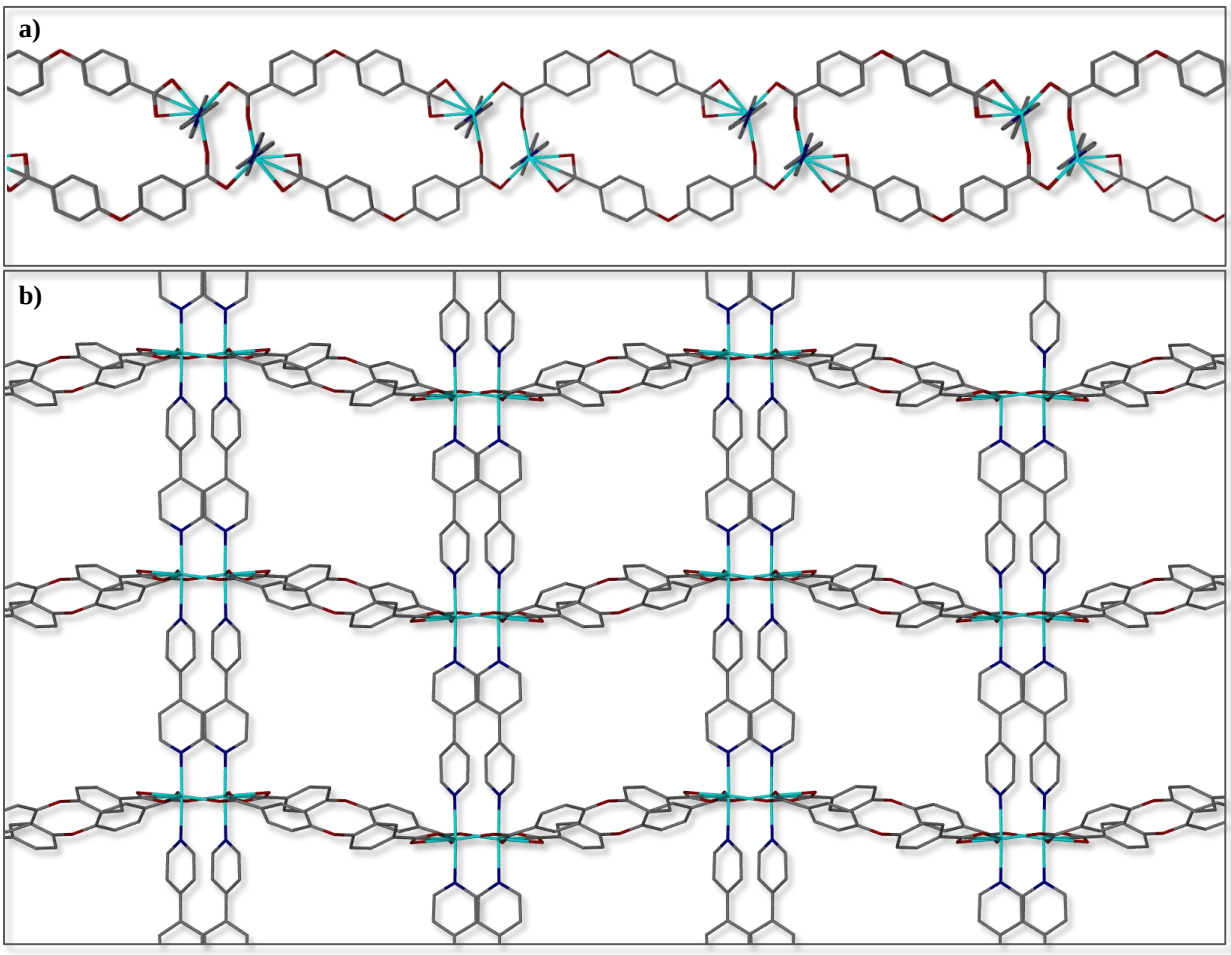

Figure 4.4 Compound **1a.** a) Viewed along [0 1 0] showing the double chains created by the cadmium nodes linked by oba ligands. b) The 2D sheet is formed through the coordination of the bpy ligand to the metal nodes connecting the chains, viewed along [1 0 1]. The DMF guest molecules are omitted for clarity.

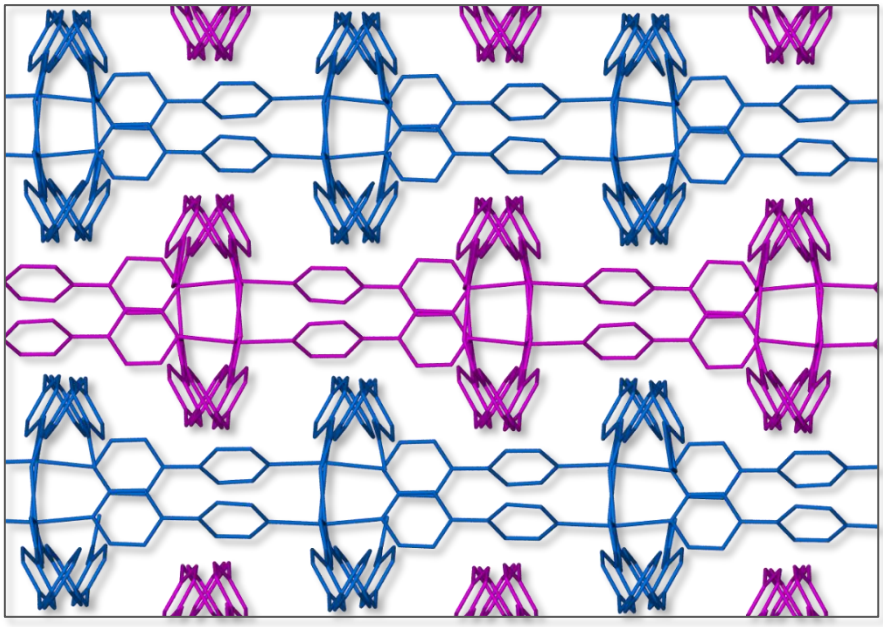

Figure 4.5 2D interdigitated layers of **1a** viewed along [1 1 1]. The different colours indicate separate layers.

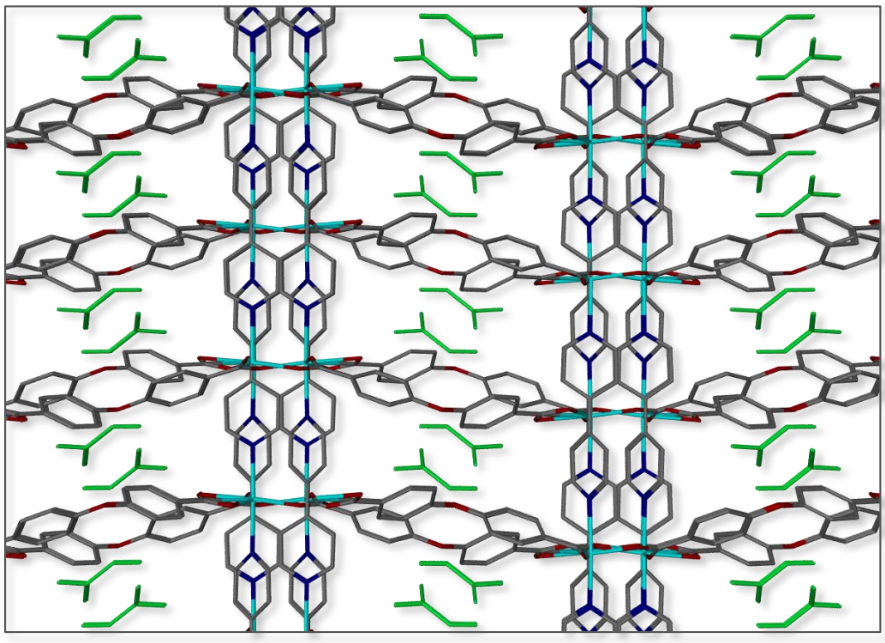

Figure 4.6 Viewed along the [1 0 0], showing **1a** with DMF molecules (green) in the voids. Only one component of the disordered DMF molecule has been shown for clarity.

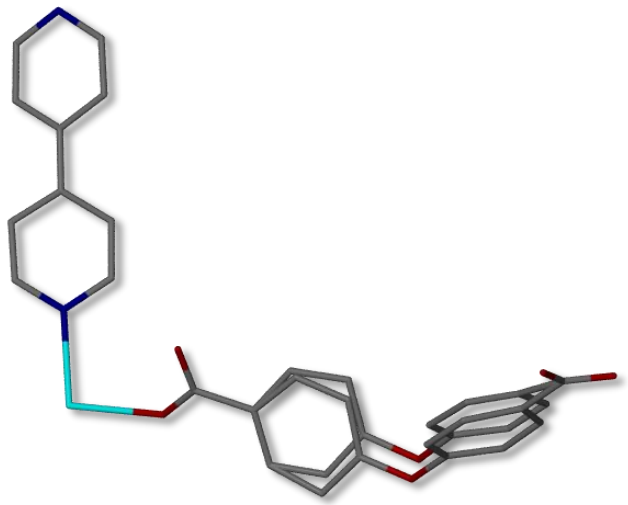

Figure 4.7 ASU of **1b** with the oba ligand disordered over two positions. SCXRD data were collected at 100 K.

The as-synthesised material was activated by applying heat (150 °C) under dynamic vacuum to remove the DMF solvent molecules while retaining crystallinity. Once activated (**1b**), the packing arrangement of the material changes slightly, with the space group changing from *C*-centred *C*2/*c* to primitive $P2_1/c$. The *c*-axis length is halved and the β angle increases (see Table 4.2). The oba aromatic rings are disordered over two positions with a 55:45 occupancy ratio, as shown in Figure 4.7. The double chain, shown in Figure 4.8a, and the 2D sheet created by the bpy ligand, shown in Figure 4.8b, essentially lead to a similar 2D interdigitated motif as in the as-synthesised form. The looped chain contracts in terms of the loops (distance between adjacent metal clusters decreases) while it expands in terms of the metal clusters (the distance between the two metal nodes in the cluster increases). The distance between the layers decreases resulting in a more closely packed material. These small changes in the motif cause a different orientation of the layers than in the as-synthesised material. The layers interdigitate in an ABAB fashion, as shown in Figure 4.9, which is different to the interdigitation shown in Figure 4.5 where the layers are interdigitated in an AAAA manner.

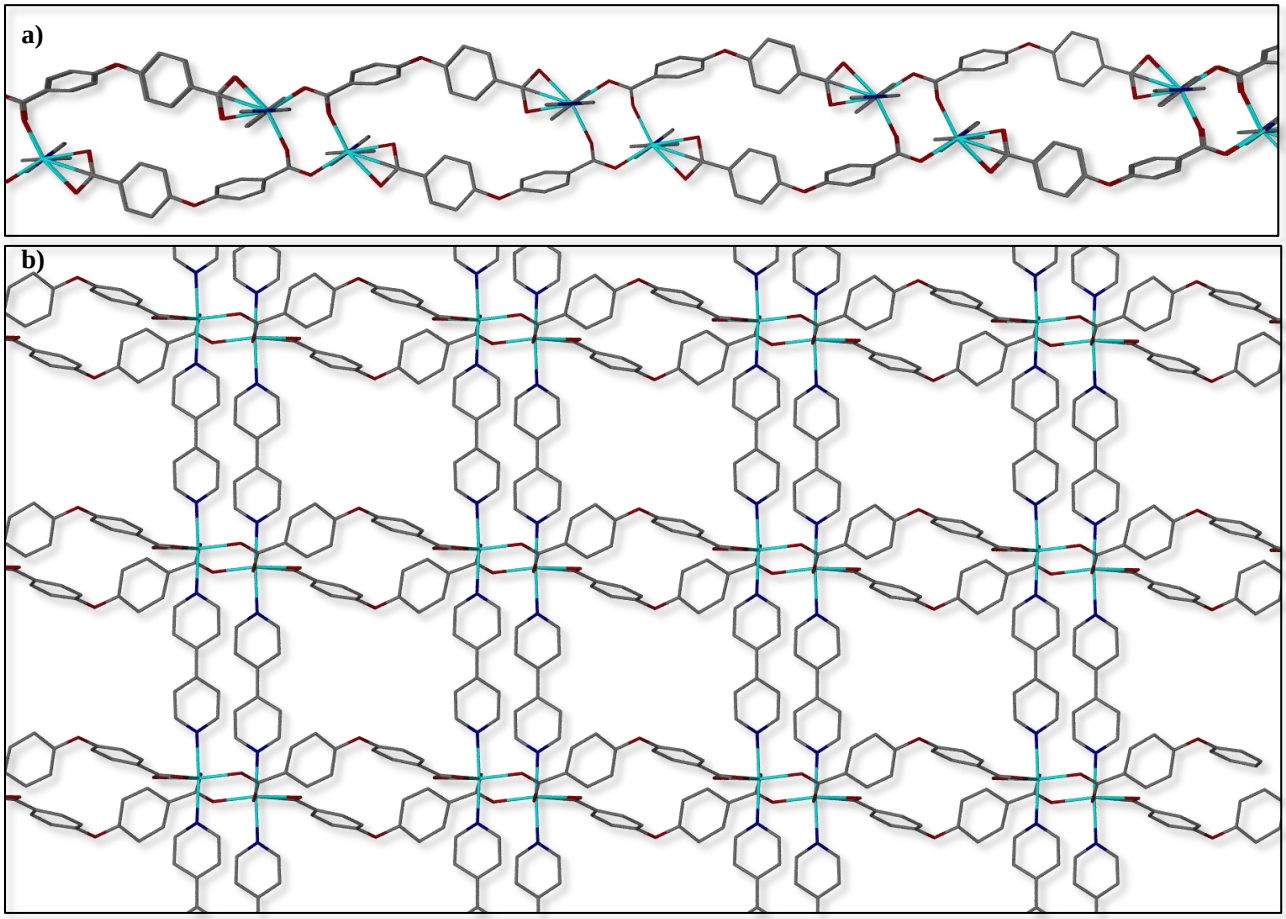

Figure 4.8 Compound **1b** a) viewed along [0 1 0] showing the 1D looped chains and b) viewed along [0 0 1], the 2D sheet pillared by bpy ligands. Only the major component of the disordered oba ligands are shown for clarity. Additionally the hydrogen atoms have been omitted for clarity.

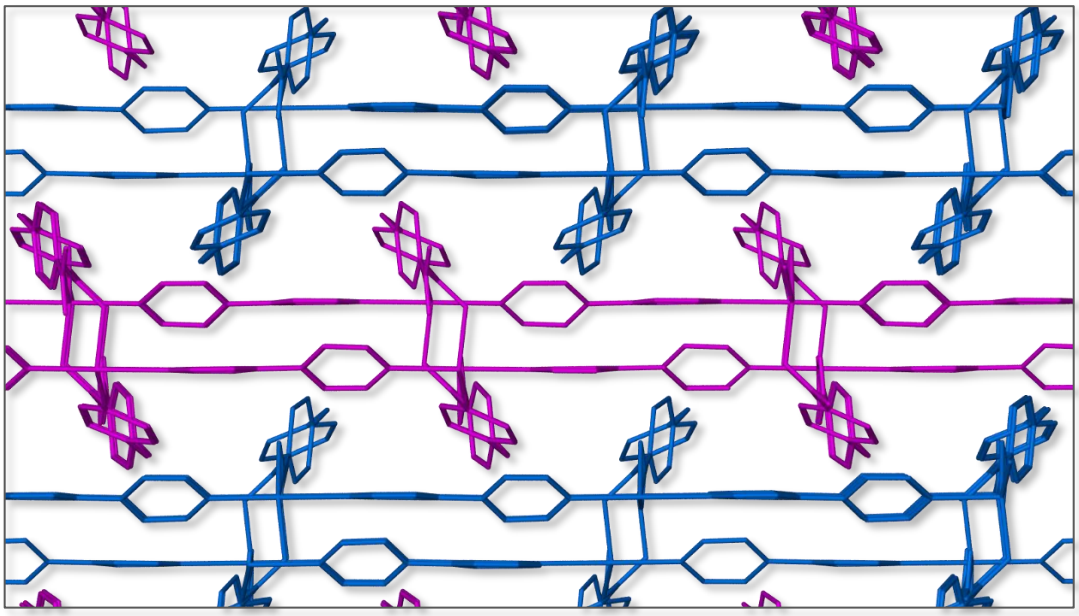

Figure 4.9 Viewed along [1 0 0], ABAB interdigitated 2D layers of **1b** are shown. The different colours are used to show the different layers.

The space available for guest uptake can be estimated using Mercury.[9,10] Figure 4.10 shows a comparison of the solvent-accessible space of the as-synthesised and the activated materials. For the as-synthesised form, the SQUEEZEd version (**1sq**) was used where the solvent molecules have essentially been omitted. A spherical probe (of radius 1.4 Å) sweeps out the available space to a potential guest molecule within a host framework. The solvent-accessible surface is mapped out by the centre of the probe, while the solvent-exclusion surface is mapped out by the surface of the probe that is in contact with the host framework. Table 4.1 shows a comparison of the volumes of the generated surfaces. For **1sq**, the large dumbbell-shaped voids imply porosity (virtual porosity). Although some interconnections are visible, the solvent accessible volume is highly dependent on the probe size used. The flexibility of the material due to the flexible oba ligand and the interdigitated layers allows for movement during gas sorption, which could lead to accessibility of these semi-isolated voids. To further understand the mechanism of sorption, SXCRD with an environmental gas cell is required where the phase changes can be observed as a function of pressure. Form **1b** has very small 1D isolated voids, which are likely unable to accommodate guest molecules. Form **1a** can be considered "open" and **1b** "closed". To compare the "open" and "closed" forms, the distances between the metal nodes and layers were measured using XSeed[11,12] (Table 4.1).

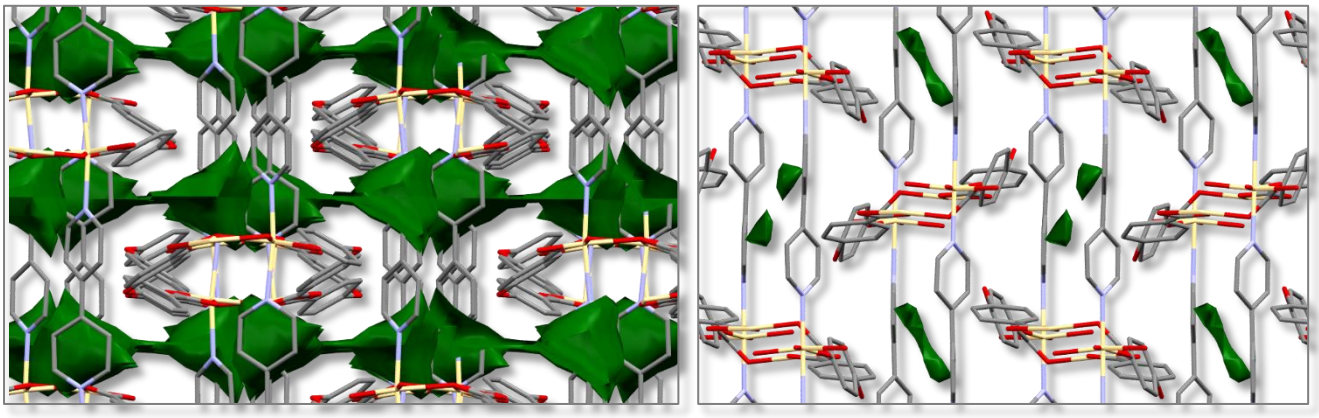

Figure 4.10 Solvent-accessible space, represented in green, calculated in Mercury using a 1.4 Å probe radius. **Left)** Form **1sq** shows 4.1% solvent accessible space per unit cell, viewed along [1 0 1]. **Right)** Form **2** shows 0.5% solvent accessible space per unit cell viewed along [1 0 0].

Table 4.1 Comparison of structural properties for the two forms of $[Cd(oba)(bpy)]_n$

	1a (open)	**1b (closed)**
Distance between Cd atoms in the dimeric metal node (Å)	3.953	4.676
Distance between Cd atoms in adjacent dimeric metal nodes (loops) (Å)	12.443	11.702
Distance between layers (Å)	7.727	6.8145
Solvent-accessible surface volume ($Å^3$/unit cell)	212.43 (4.1 %)	11.79 (0.5%)
Solvent-exclusion surface volume ($Å^3$/unit cell)	1178.50 (22.5%)	172.20 (7.5%)

4.1.2 PXRD

The experimental PXRD pattern of **1a** corresponds well to that calculated from the SCXRD structures, as shown in Figure 4.11 4.11. The PXRD patterns for **1b**, however, have some differences compared to the calculated pattern shown in Figure 4.12. Some of the shifted peaks may be due to the temperature difference between the room temperature PXRD data collections and the SCXRD data collection carried out at 100 K. Another reason for the difference in the profiles is the presence of preferred orientation due to the plate-like morphology of the crystals and the tendency of plates to pack in the same orientation.

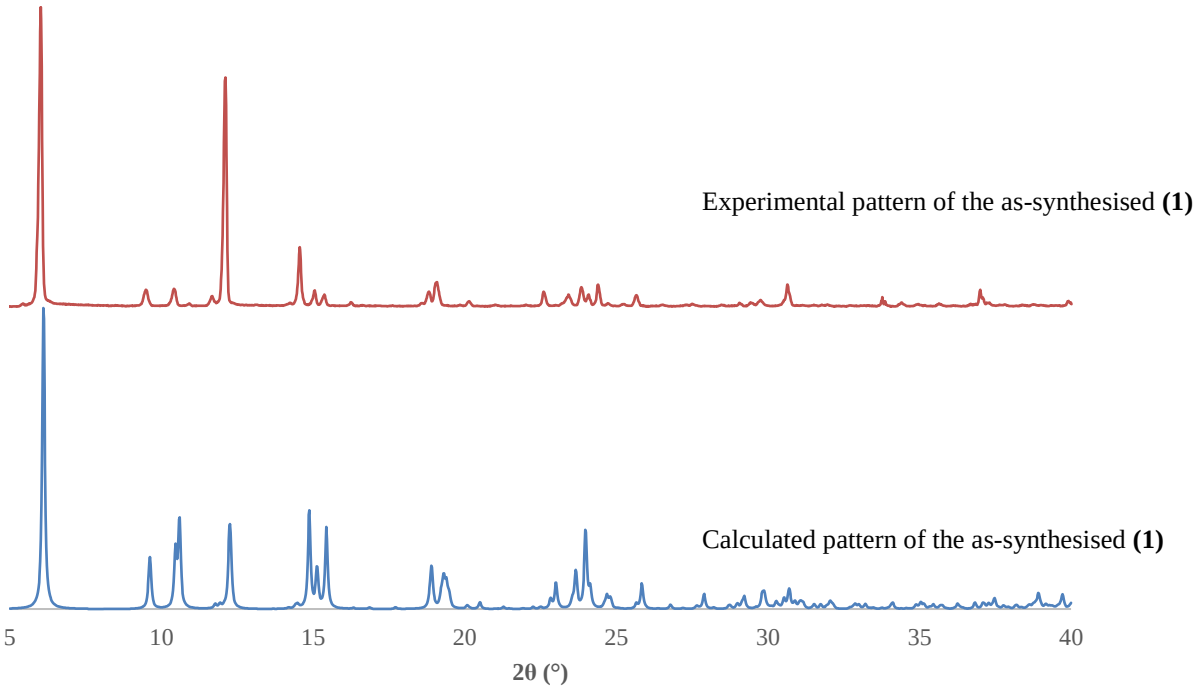

Figure 4.11 PXRD profiles for **1a**. **Bottom:** The calculated PXRD profile of the as-synthesised material based on SCXRD data collected at 100 K. **Top:** Experimental PXRD profile of the as-synthesised material collected at room temperature.

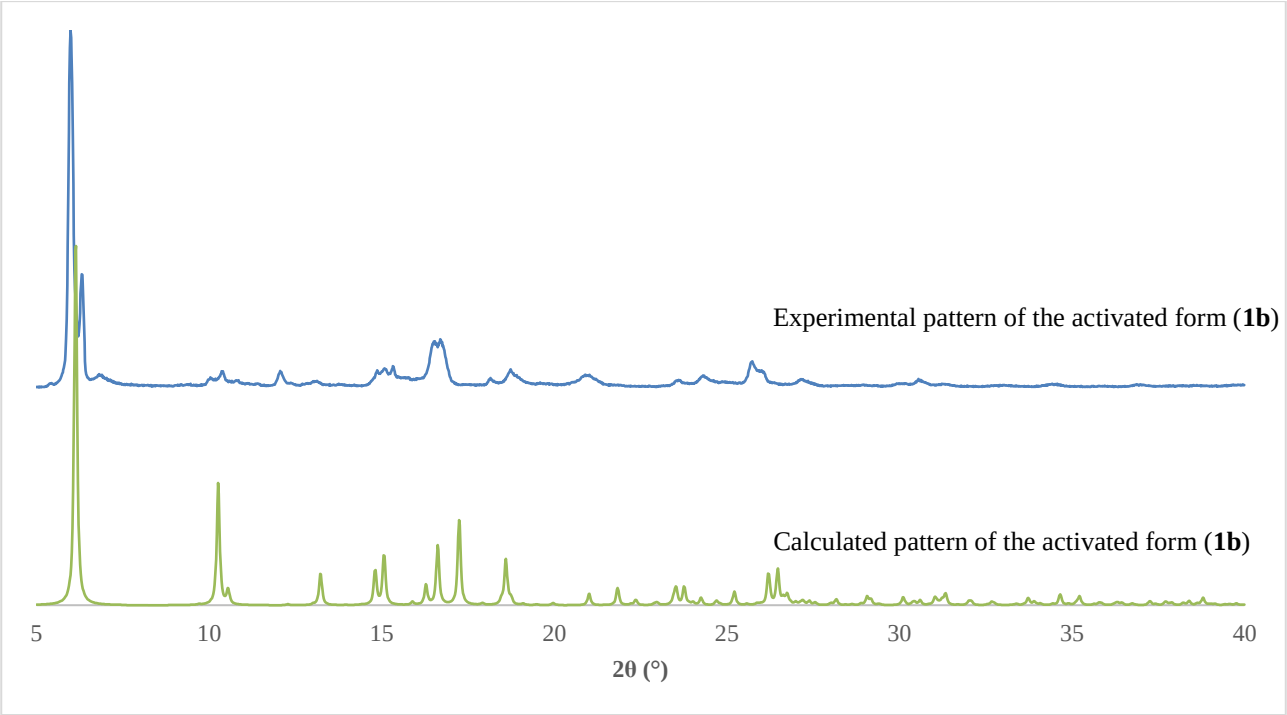

Figure 4.12 PXRD profiles of **1b**. **Bottom:** Calculated profile of the as-synthesised material based on SCXRD data collected at 100 K. **Top:** Experimental profile of the as-synthesised material measured at room temperature.

4.1.3 TGA

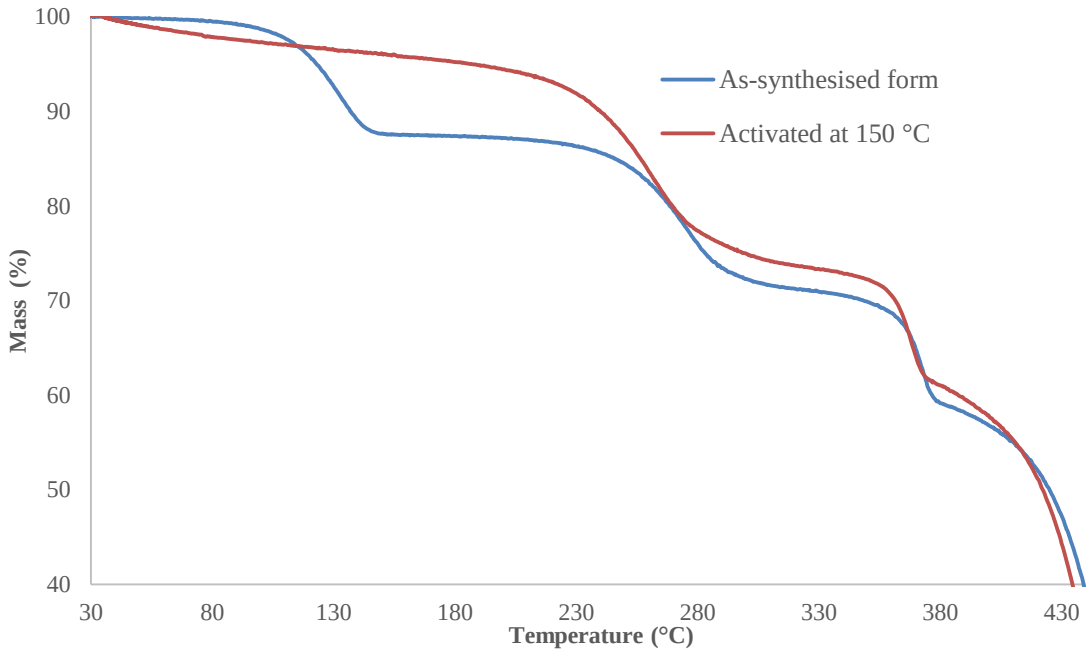

Figure 4.13 TGA of **1a** and **1b**. The as-synthesised form displays a % mass loss corresponding to 1.16 molecules of DMF. This mass loss is not present for **1b** except for a slight slope which can be attributed to some water uptake from the atmosphere.

In Figure 4.13, the thermogram of the as-synthesised material shows a mass loss of 12.46% between 100-150 °C, corresponding to the release of 1.16 DMF molecule per ASU. This mass loss is less than that predicted using SQUEEZE, i.e. 1.6 DMF molecules per ASU. There are two possible reasons for the difference. Firstly, SQUEEZE includes all residual electron density, which may include residual electron density peaks around the metal centres, overestimating the amount of DMF present. The other possibility is that some solvent is lost before the TGA is carried out and thus the amount of DMF present is underestimated. The TGA trace shows that activation of the sample was successful since, after exposure to dynamic vacuum at 150 °C for 24 hours, there is no major weight loss in the temperature range where DMF guest molecules are lost. There is a small mass loss owing to decomposition of the material, which commences at 250 °C for both forms.

4.2 Results and discussion

Gas sorption, as well as PGDSC, studies were carried out on **1b** (activated form) at room temperature for CO_2, N_2 and CH_4. Following the method developed in Chapter 3 with CuHKUST, the sorption and desorption isotherms were fitted independently. The loading was obtained from these fitted curves while the heat released in the process was extracted from the heat flow measurements. Combining these results, Q_{st} curves were constructed for the three gases. All experiments were carried out at 298 K, with all fitting statistics and information provided in Appendix A.

4.2.1 Gas sorption

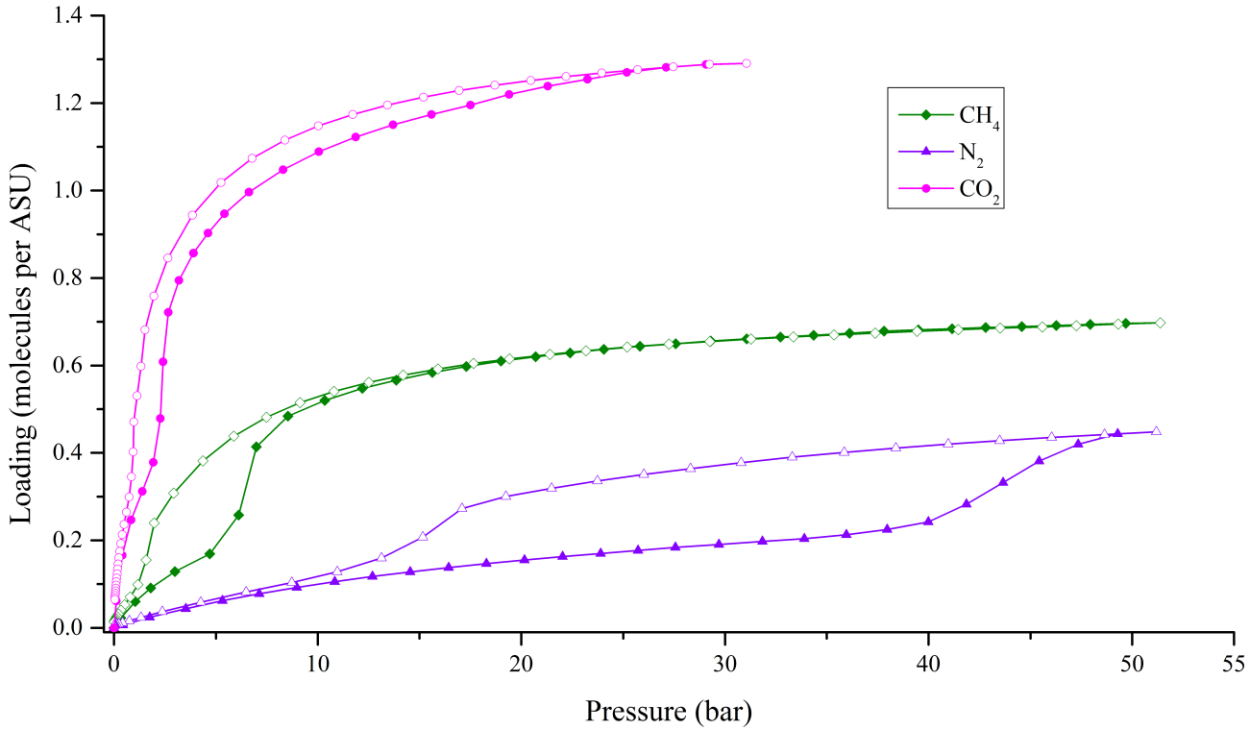

Figure 4.14 Sorption profiles for three gases (CH_4, N_2, and CO2) at 298 K by **1b**, showing stepped profiles with hysteresis to varying degrees. Closed data points show sorption and open data points show desorption.

The sorption profiles shown in Figure 4.14 exhibit stepped sorption with hysteresis. The stepped profiles can be attributed to "opening" of the framework as a pressure-induced effect. For CO_2, N_2 and CH_4 gases, the gate-opening pressures were between 2-3 bar, 38-40 bar and 4-5 bar, respectively. The Brunauer-Teller profile that most closely matches the experimental profiles for the three gases is Type IV. The "opening" of the framework can be observed when comparing the distance between the layers in **1a** and **1b,** as shown in Figure 4.15. The flexibility of the material allows for structural transformations from the open form to the closed form. The movement of the layers is reversible based on the powder profiles shown in Figure 4.16 and 4**.**17, where the final pattern after desorption matches the original activated phase. Using variable PXRD, with CO_2 gas, the phase change could be followed by monitoring the changes in the PXRD profiles. It also served to confirm the reversibility of the phase change. This shows that the phase transitions are reversible and that the material is reusable and can be regenerated for further sorption experiments.

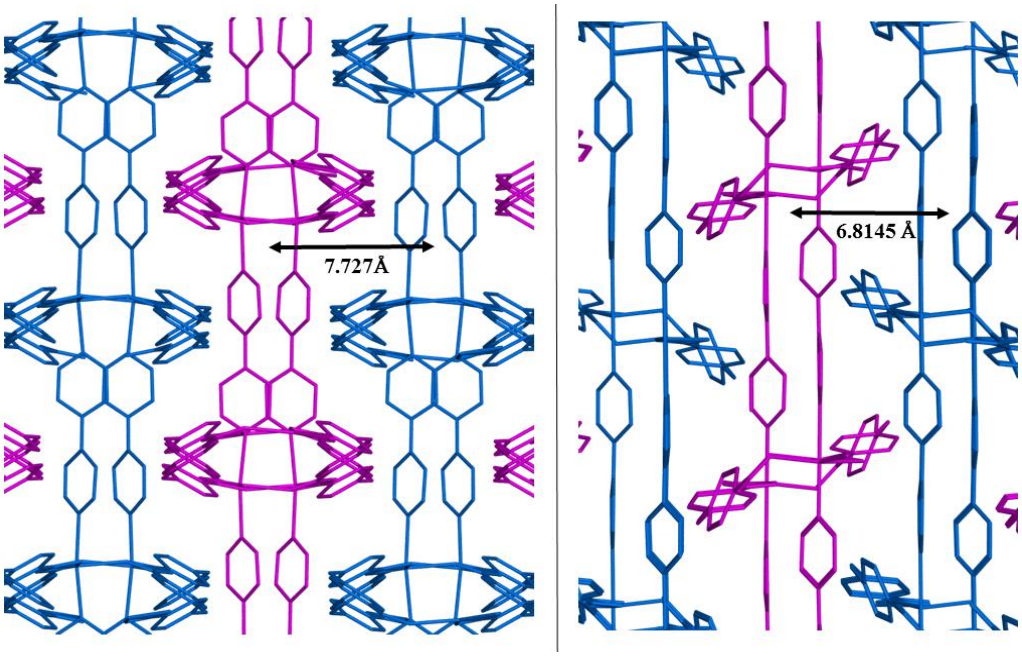

Figure 4.15 Comparison of the distances between the interdigitated 2D layers in **1a** and **1b**.

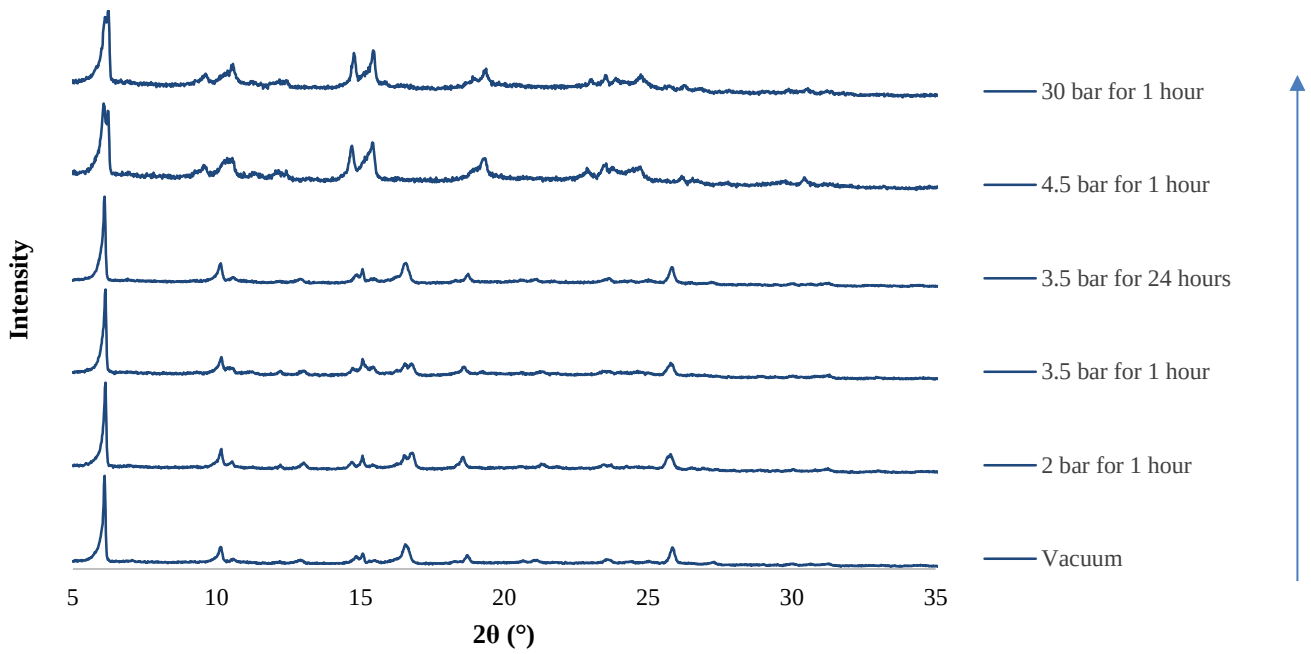

Figure 4.16 Variable pressure PXRD profiles showing CO_2 sorption for **1b** at 298 K. The blue arrow shows the order of execution of the experiments.

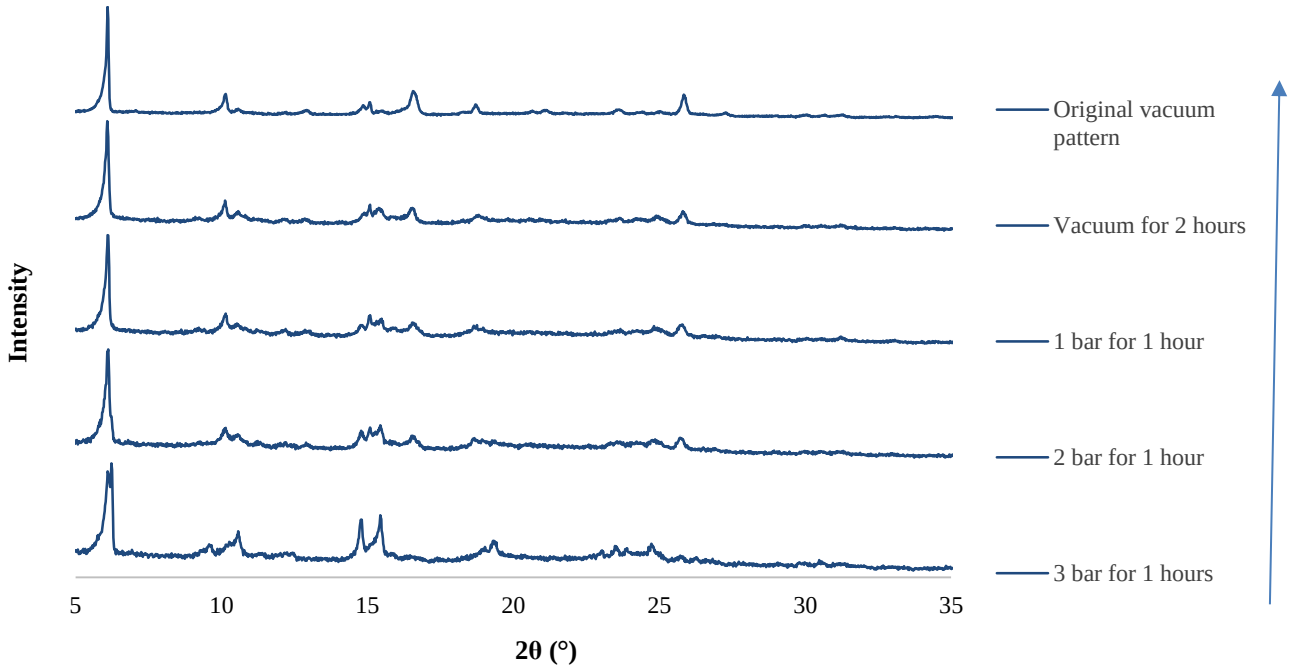

Figure 4.17 Variable pressure PXRD profiles showing CO_2 desorption for **1b** at 298 K. The blue arrow shows the order of execution of the experiments.

It is noteworthy that hysteresis, such as that observed in this study, is rather uncommon for N_2. It is expected that, since N_2 gas is neutral with few induced-dipole moments and because the gas molecules are small in size, there will be little or no interaction between the gas and the framework, and therefore no hysteresis. A previous study has shown nitrogen hysteresis in a material with 2D interdigitated layers.[2] The

sorption profile is shown in Figure 4.18. Kituara *et al.* reported that even gases with weak dispersive interactions can display sorption hysteresis with flexible materials, as facilitated by layer displacement.[2]

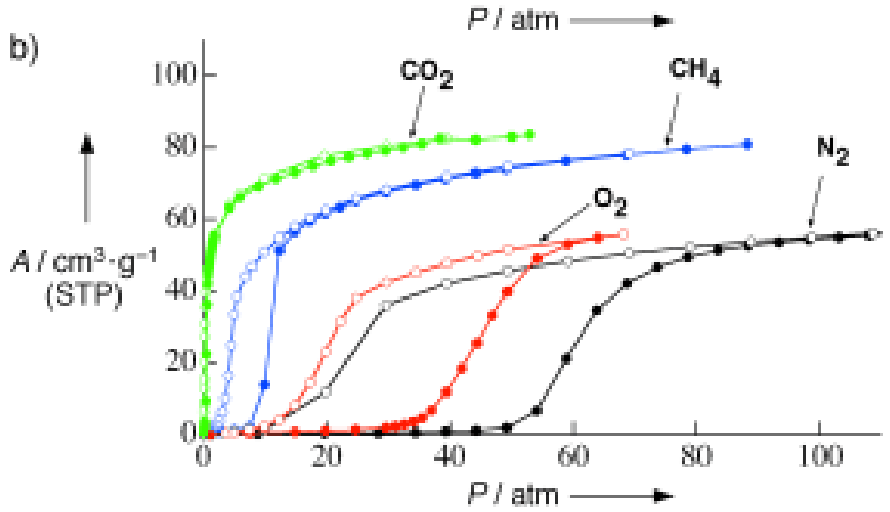

Figure 4.18 Sorption hysteresis for N_2 gas with a 2D interdigitated material carried out by Kitaura *et al.*[2]

As previously mentioned, loading is required to determine Q_{st} from heat-flow data, and can be obtained from the sorption isotherms. Curves were fitted separately to sorption and desorption sections (Figures 4.19, 4.20 and 4.21) to allow gas loading to be obtained with the OriginPro "find X from Y" function. To fit curves more easily and precisely to the sorption data for CO_2 and CH_4 gas, the axes were inverted (Figure 4.19 and Figure 4.21) This does not affect the Q_{st} calculations since the same function for finding loading from the pressure range can be utilised ("find Y from X").

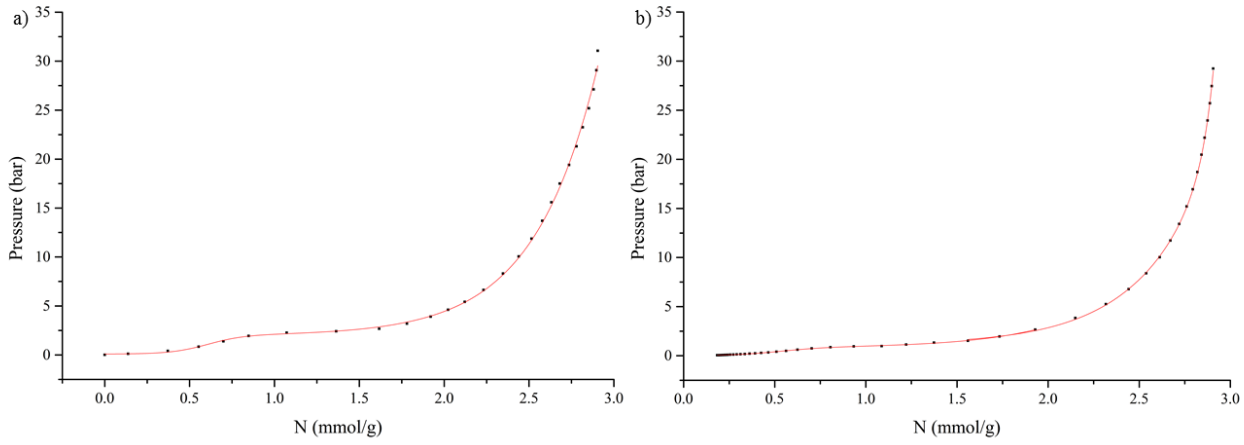

Figure 4.19 CO_2 sorption data collected at 298 K for **1b** with fitted curves, **a)** sorption is fitted with a double Boltzmann fit **b)** desorption is fitted with biphasic dose response fit. Fitting parameters and statistics can be found in Appendix A, Table S10 and S11.

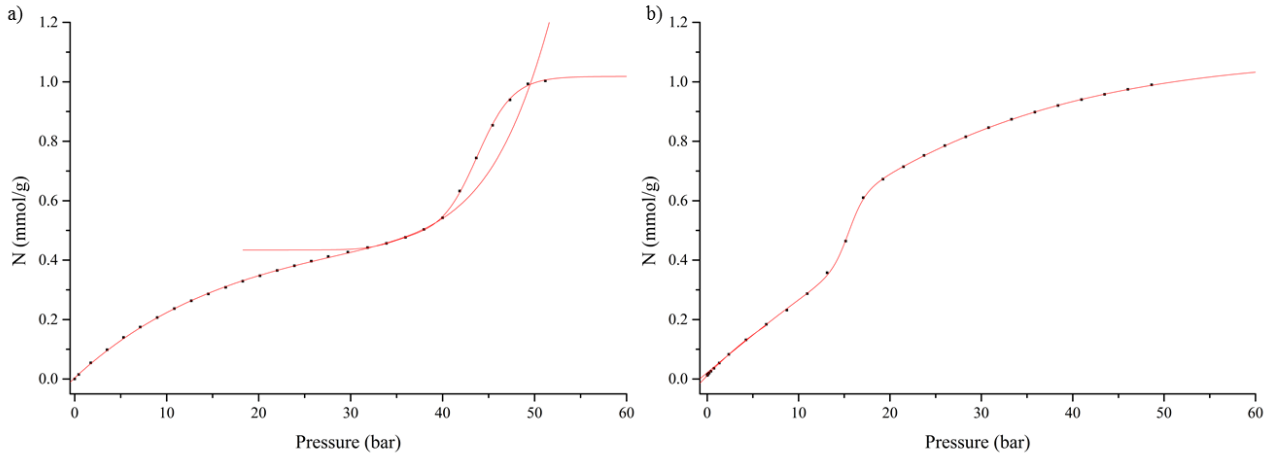

Figure 4.20 N_2 sorption data collected at 298 K for **1b** with fitted curves, **a)** sorption fitted with a biphasic dose response fit; the overlapping curves are due to the separately fitted sections **b)** desorption fitted with a biphasic dose response fit. Fitting parameters and statistics can be found in Appendix A, Tables S12 and S13.

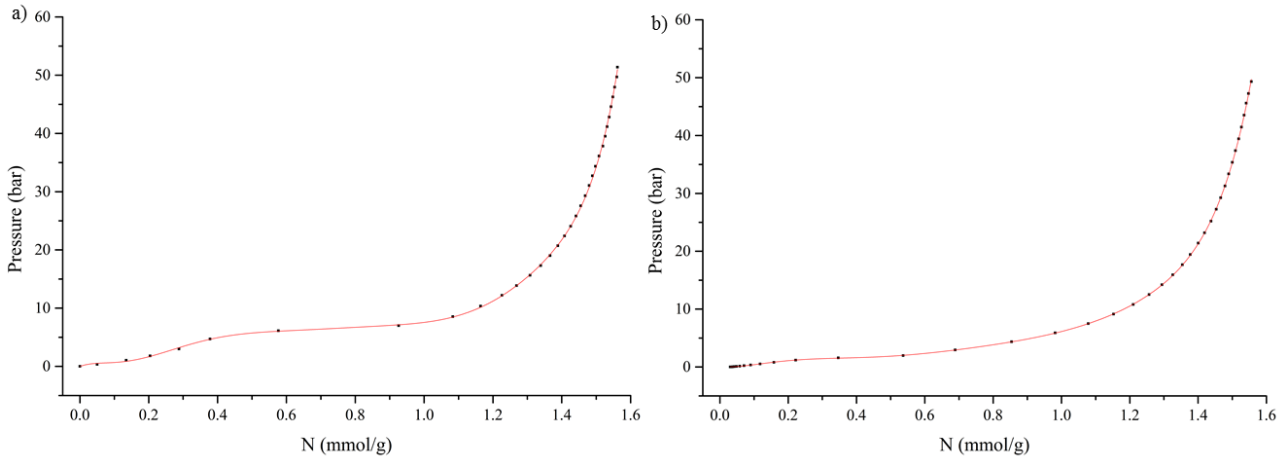

Figure 4.21 CH_4 sorption data collected at 298 K for 1b with fitted curves, **a)** sorption fitted with a polynomial fit **b)** desorption fitted with a polynomial fit. Fitting parameters and statistics can be found in Appendix A, Tables S14 and S15.

4.2.2 Heat measurements

The heat-flow profile for CO_2 shown in Figure 4.22 displays a large exothermic peak corresponding to the sorption gate-opening inflection point at 2.5 bar. The framework undergoes a structural phase change from closed to open, allowing rapid intake of CO_2 gas molecules. The gap at 11 bar in the heat-flow curve for CO_2 is due to the instrument's limitation of gas compression. With an initial pressure of 1 bar, a maximum of 10 bar can be reached. For higher pressure ranges, a higher initial pressure is necessary, which needs to be changed manually. The data are later merged.

Figure 4.23 shows the heat flow for the sorption of N_2 gas. The initial small peak (point A) is due to merging of the heat-flow curves at 10 bar. If it were possible to measure heat flow continuously over the total pressure range then there would be a continuous steady increase in heat flow as there are no corresponding inflection points in the sorption isotherm. This indicates that there is no structural transition at this point and

no heat-flow peak anticipated, although the measurement would need to be repeated to confirm this hypothesis. The large exothermic peak during the sorption of N_2 corresponds to the gate-opening pressure of 40 bar, showing an abrupt intake of gas due to opening of the framework. Figure 4.24 for CH_4 also exhibits an exothermic peak corresponding to a gate-opening pressure of 5 bar. The desorption peaks occurs at different onset pressures to the sorption peaks which corresponds to hysteresis in the sorption isotherms.

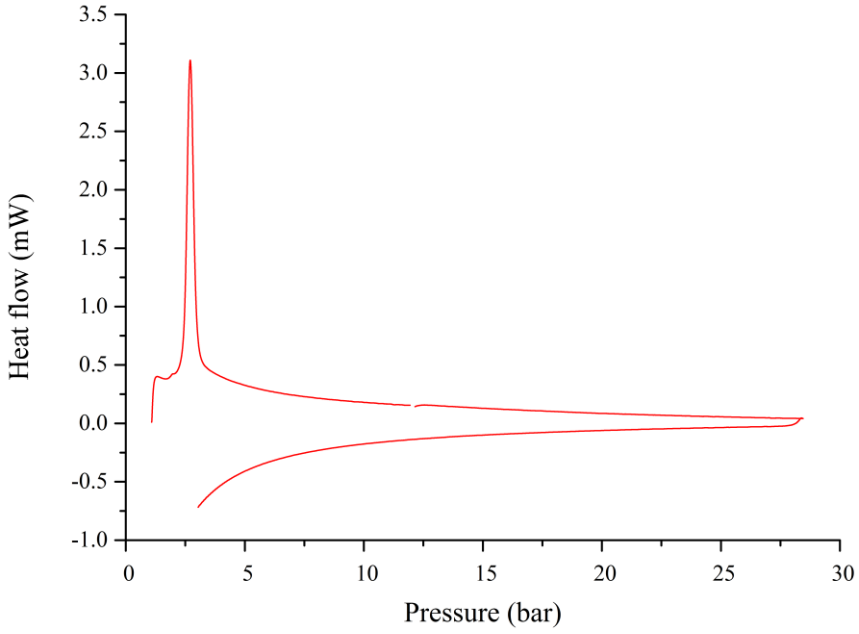

Figure 4.22 Heat flow curves as a function of pressure for CO_2 sorption by **1b** at 298 K.

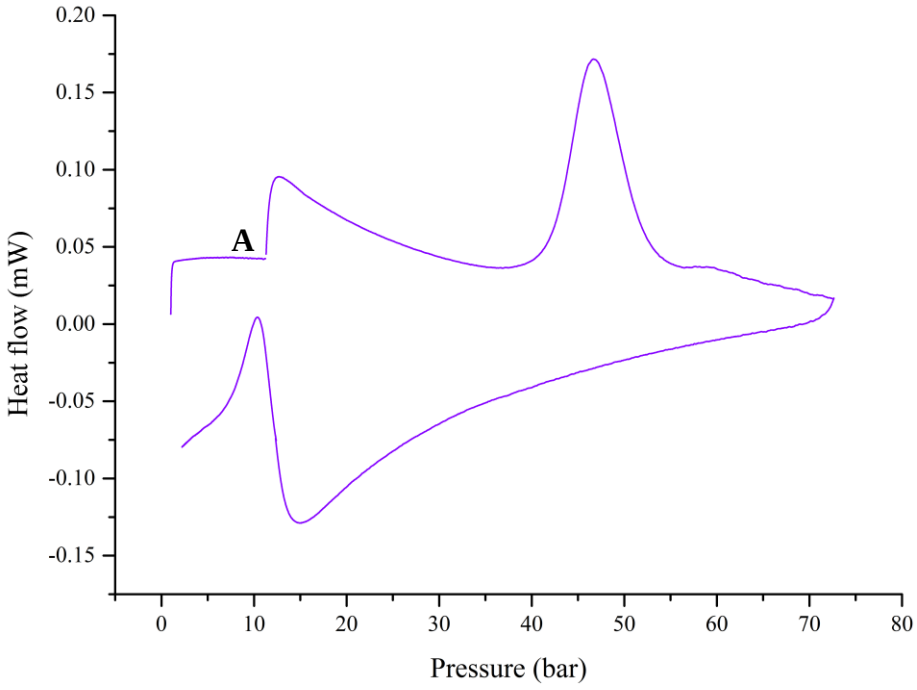

Figure 4.23 Heat flow curves as a function of pressure for N_2 sorption by **1b** at 298 K.

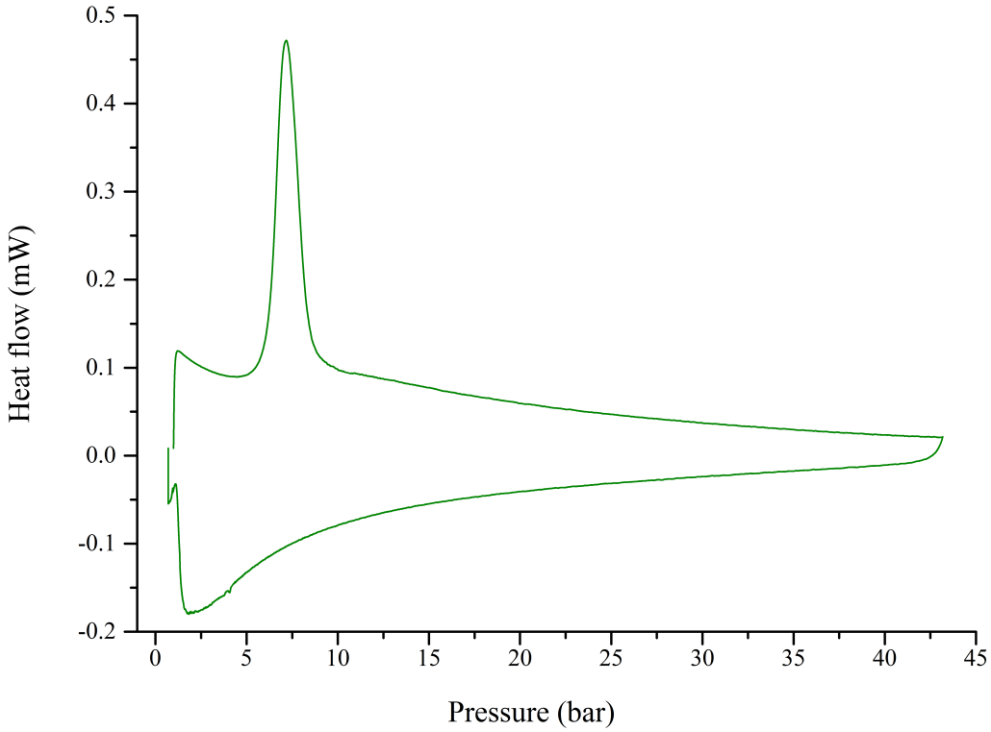

Figure 4.24 Heat flow curves as a function of pressure for CH_4 sorption by **1b** at 298 K.

The heat-flow profiles for both N_2 and CH_4 exhibit exothermic peaks at the end of desorption, at 12 and 2 bar, respectively. Since desorption is an endothermic process (see Chapter 1) this is unexpected. Both profiles show a steady decline of heat flow during desorption, suggesting that gas desorption takes place over a large pressure range. The desorption exothermic peak could represent the heat associated with the structural transformation from "open" back to "closed", essentially forcing out any remaining gas molecules. The peak has heat-flow contribution from desorption, meaning that the amount of heat flow measured does not directly correspond to the structural transformation and could be masked by some heat of desorption. The CH_4 desorption peak is not fully visible at 298 K and PGDSC experiments were thus recorded at higher temperatures in an attempt to elucidate the peak to confirm its presence, as shown Figure 4.25. The PGDSC experiment carried out at 343 K displayed the desorption peak most clearly compared to experiments at 313,323 and 333 K.

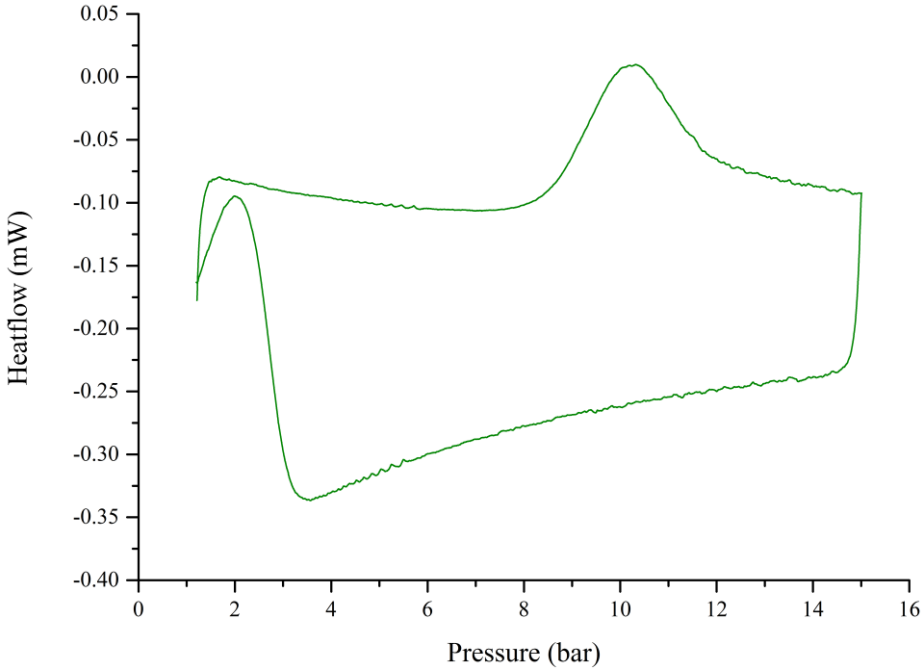

Figure 4.25 Heat flow profile for **1b** with CH_4 at 343 K showing the unusual exothermic peak during the desorption section.

The integral-heat curves are shown in Figures 4.26, 4.27 and 4.28, for CO_2, N_2 and CH_4, respectively. Smoothing of these curves was not possible as the smoothing functions in OriginPro were not suitable for these kind of data, which dramatically changed the outcome of the Q_{st} calculations. To overcome this issue, curves were fitted to the data as accurately and precisely as possible. In some cases the data was divided into ranges and each range was fitted separately but on the same axes to create overlapping fitted curves. The curve fitting parameters and statistics can be found in the Appendix A.

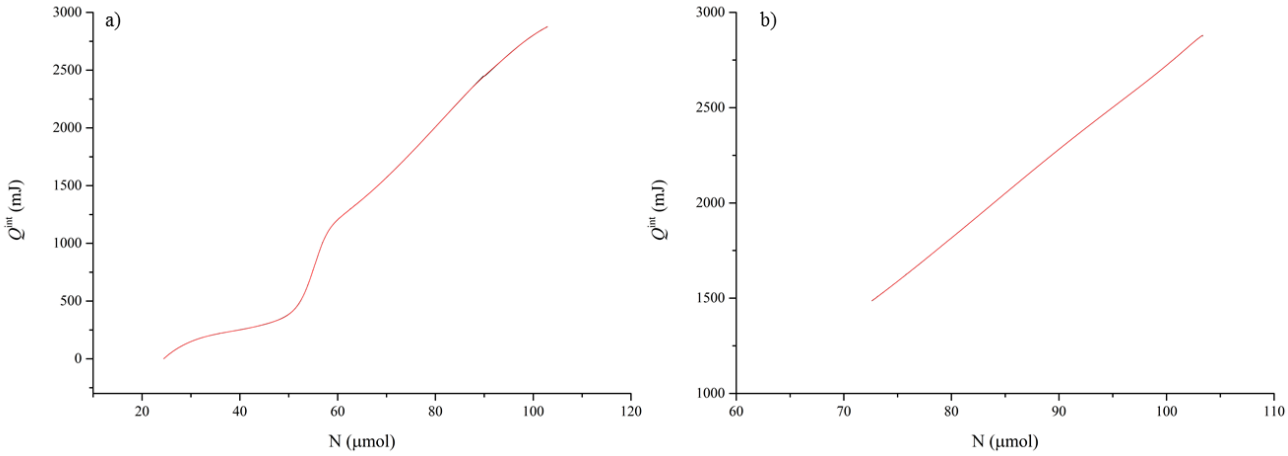

Figure 4.26 Integral heat with fitted curve for sorption of CO_2 at 298 K by **1b**. The black lines represent the experimental data while the red line represents the fitted curves. **a)** sorption fitted with a polynomial fit **b)** desorption fitted with a polynomial fit. Fitting parameters and statistics can be found in Appendix A, Tables S16 and S17.

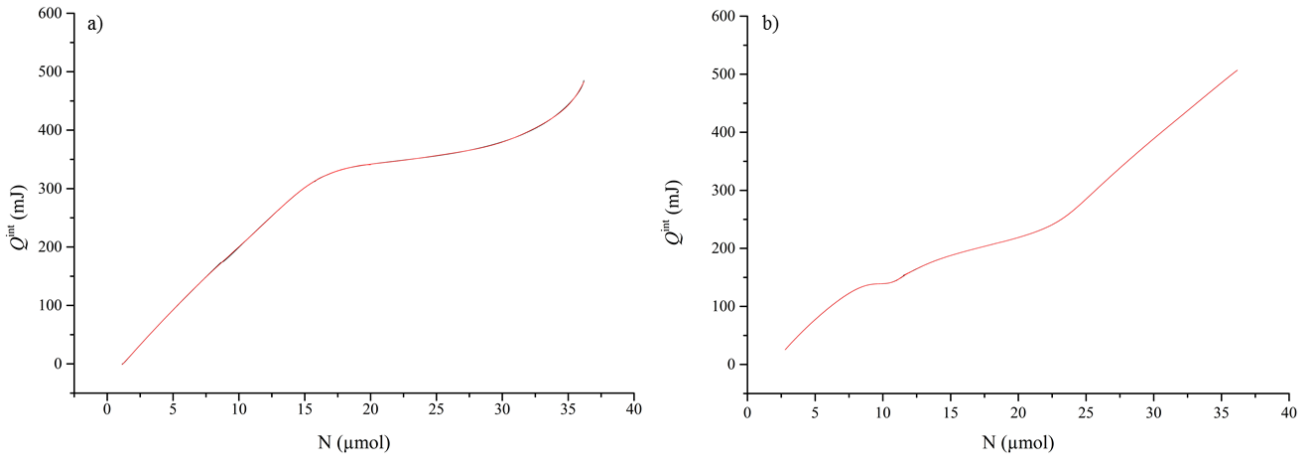

Figure 4.27 Integral heat with fitted curve for sorption of N_2 at 298 K by **1b**. The black lines represent the experimental data while the red line represents the fitted curves. **a)** sorption fitted with a polynomial fit, **b)** desorption fitted with a polynomial fit. Fitting parameters and statistics can be found in Appendix A, Tables S18 and S19.

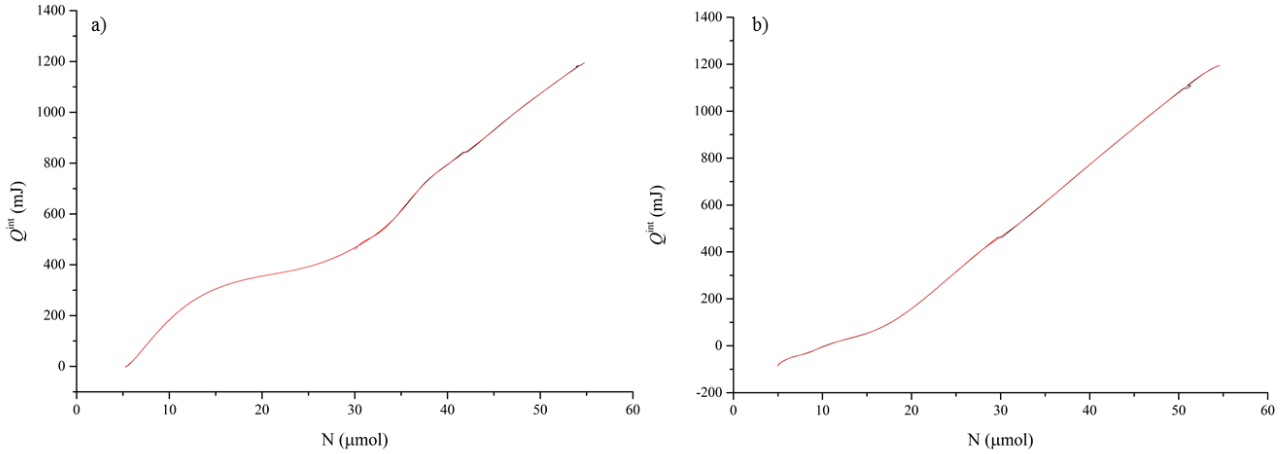

Figure 4.28 Integral heat with fitted curve for sorption of CH_4 at 298 K by **1b**. The black lines represent the experimental data while the red line represents the fitted curves. **a)** Sorption fitted with a polynomial fit, **b)** Desorption fitted with polynomial fit. Fitting parameters and statistics can be found in Appendix A, Tables S20 and S21.

4.2.3 Isosteric heat

Q_{st} was determined through the method laid out in Chapter 2, whereby the gas loading is extracted from the sorption data and the differential heat is extracted from the PGDSC data. Adding a thermodynamic term, RT, to the differential heat gives Q_{st}. Figure 4.29 shows the Q_{st} curve for CO_2. The initial values of the sorption section are due to a small amount of sorption occurring at pressures below 2 bar. The large peak at approximately 1.5 mmol/g loading (N) corresponds to the exothermic peak in the heat-flow curve in Figure 4.22, which is attributed to an abrupt intake of gas as a result of a structural transformation ("closed" to "open" form). The heat associated with the structural transformation, although exothermic, cannot be differentiated from the heat evolved during the gas uptake as the latter is much larger and will most likely mask the structural-transformational heat. Figure 4.30 shows how the peak coincides with the abrupt increase in the amount of

total integral heat released during sorption of CO_2. The Q_{st} curve shows how the "affinity" of the framework for the gas increases as a result of the framework changing to accommodate the guest.

Little Q_{st} information is available for the desorption section of the CO_2 Q_{st} curve, except that it corresponds to the Q_{st} determined from sorption. To obtain better Q_{st} results for desorption of CO_2, the PGDSC experiments need to be repeated at lower desorption pressure ranges. Due to time constraints this was not carried out, but it is an obvious option for future work.

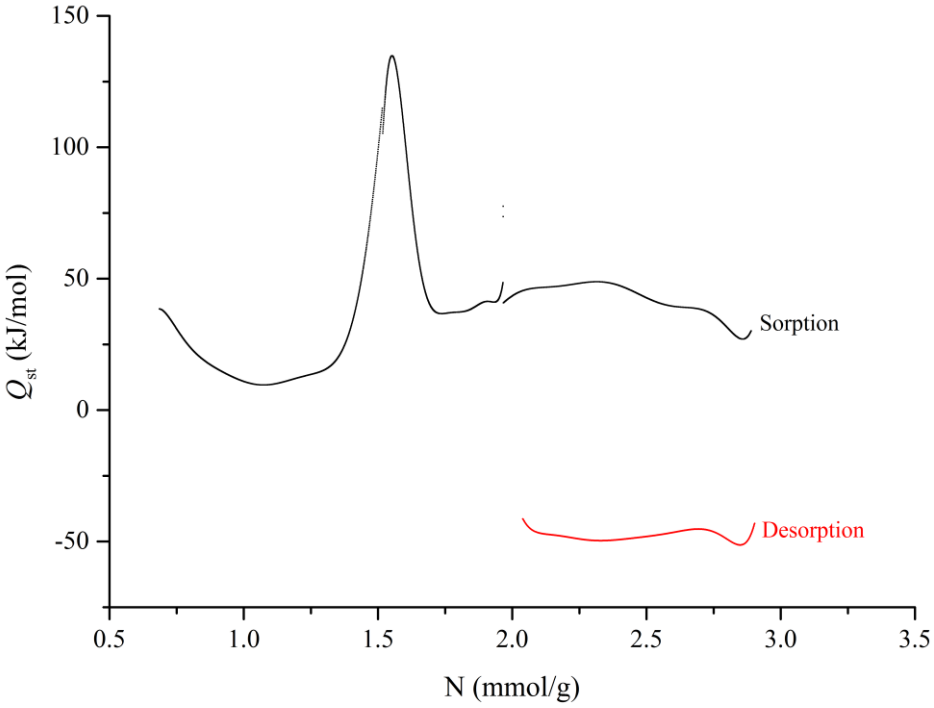

Figure 4.29 Q_{st} curve for **1b** and CO_2.

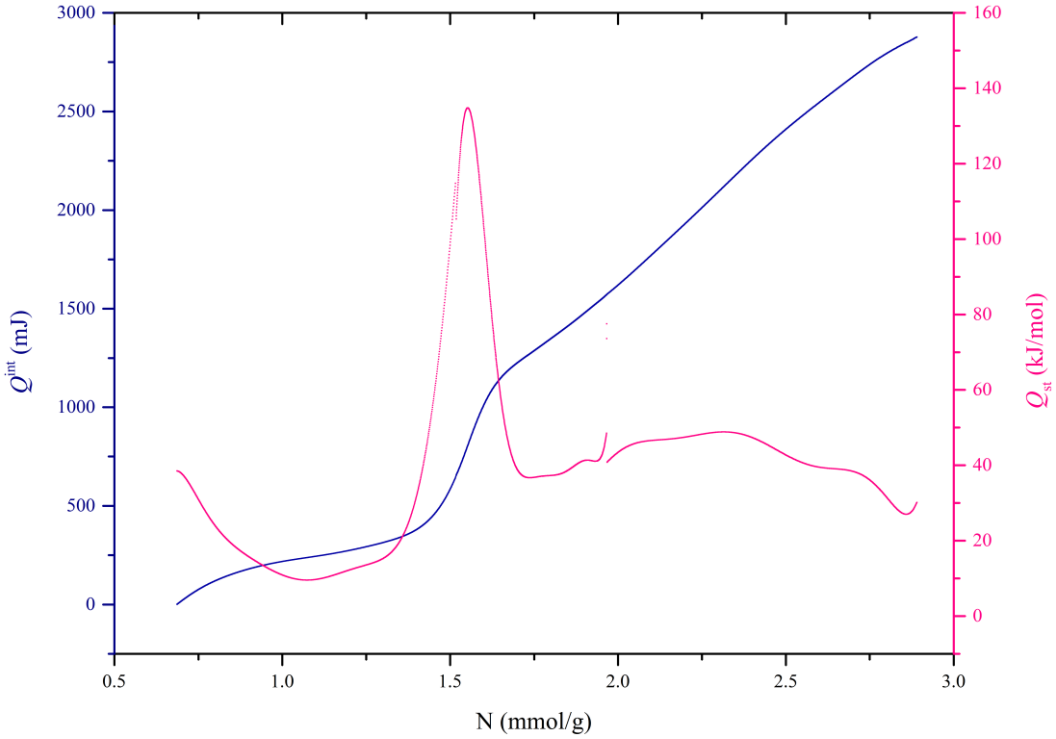

Figure 4.30 An overlay of Q_{st} and Q^{int} (total heat released) for sorption of CO_2 by **1b** carried out at 298 K.

Q_{st} results for N_2 gas are somewhat incomplete as the sorption was measured up to 50 bar, whereas the PGDSC experiments were carried out to pressures as high as 70 bar. This resulted in a large peak in the heat-flow curve being cut off halfway through the peak. An observation can, however, be made about the Q_{st} curve; the obvious beginning of a peak can be seen at 1 mmol/g loading. Another sorption experiment up to higher pressures would help reveal this peak. A peak during the desorption process of N_2, tending towards the positive, can be observed that corresponds to the unusual exothermic peak observed in the desorption section of the heat-flow curve in Figure 4.23. This "exothermic" peak in the Q_{st} curve indicates that the framework does not have a high affinity for N_2 gas at this loading. This supports the theory that the framework undergoes a transformation back to a "closed" form that is less porous.

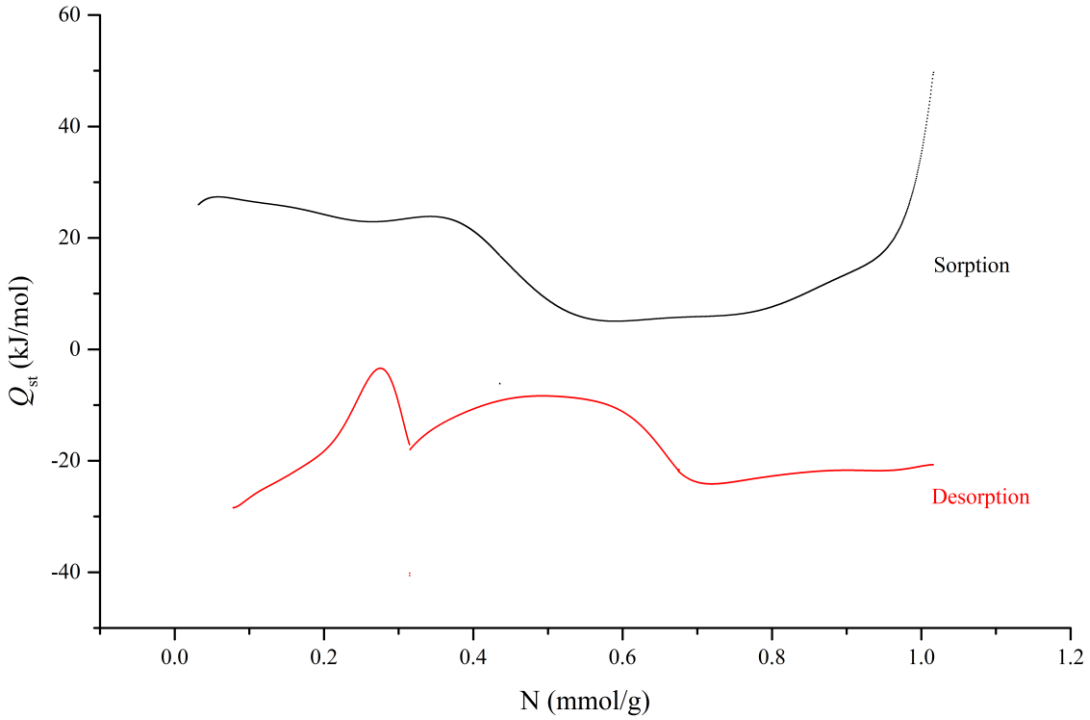

Figure 4.31 Q_{st} curve for **1b** and N_2.

CH_4 gas is important for studies involving purification or storage of natural gas.[13,14] The Q_{st} results for CH_4 are not conclusive but some observations can be made. From the raw Q_{st} data in Figure 4.32, obtained without fitting a curve to Q^{int} data, we can see that this gives a very broad picture of the affinity of the gas to the framework as a function of loading. Only when the fitted lines are applied to the Q^{int} data are applied before the Q_{st} calculations are carried out, are there distinct peaks corresponding to increases in the uptake of gas. The gaps in the Q_{st} curves are as a result of the separately collected PGDSC data, as described previously. The exothermic peak present in the heat-flow curve is also partly reflected by the Q_{st} curve trending to the positive, meaning that the affinity of the framework for CH_4, decreases observed for N_2 gas.

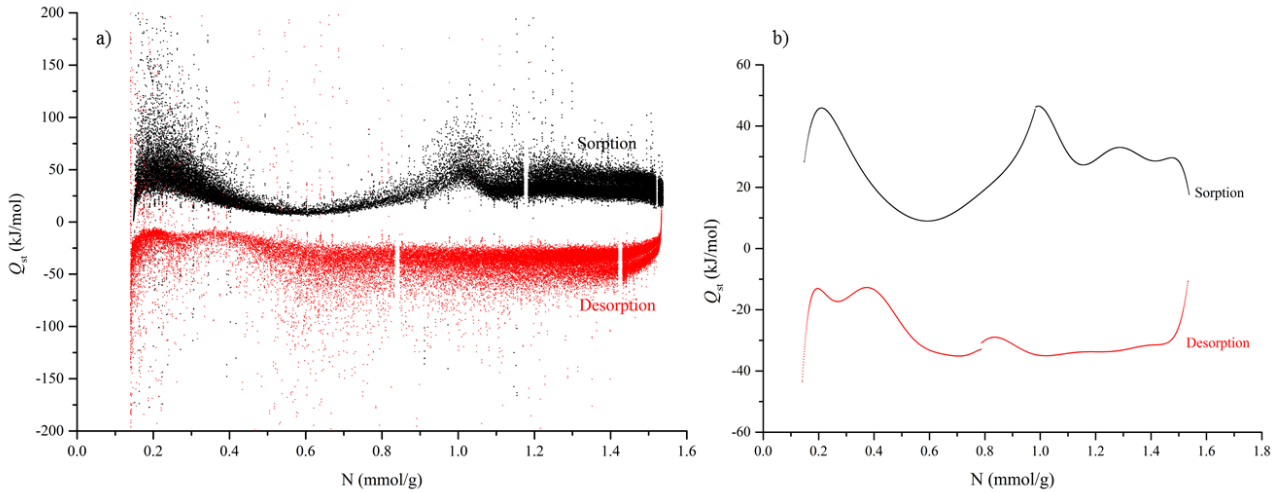

Figure 4.32 Q_{st} results for CH_4 gas with **1b**, **a)** without making use of fitted Q^{int} curves and **b)** calculated Q_{st} using fitted Q^{int} curves.

Comparing the Q_{st} results, $[Cd(oba)(bpy)]_n$ has the highest affinity for CO_2 gas over N_2 and CH_4. The Q_{st} results for N_2 are not complete but based on the heat-flow profiles (Figure 4.22 and Figure 4.23) for CO_2 and N_2, a higher heat flow for N_2 was recorded. Heat flows of 3.0 and 1.7 mW was recorded for CO_2 and N_2, respectively. The sorption profile in Figure 4.14 also shows that the material takes up more molecules of CO_2 (1.3) per ASU than N_2 (0.4). This is not an absolute proof of selectivity and breakthrough experiments need to be carried out with a mixture of gases to show true selectivity. These results do, however, give an indication of preference of the material which is important information for separation studies. Zero-loading values, in this instance, do not give information about the gas interaction with the material since the main adsorption takes place after gate-opening pressures and was thus not determined. Furthermore, we recommend that the full range of Q_{st} values be reported for materials exhibiting stepped sorption and hysteresis. All of the Q_{st} curves reflect the presence of hysteresis, as do Q_{st} curves obtained from Type I sorption.

Q_{st} values have, in the past, been used to differentiate between chemisorption and physisorption. If the value exceeds 20 kJ/mol then it is considered to be chemisorption.[15,16] The Q_{st} values for this model compound are significantly above 20 kJ/mol at multiple points in the curve, especially for peaks that correspond to the structural transformation that causes a sudden intake of gas molecules. Since this sorption process is reversible without heat input, it is unlikely that chemisorption occurs. Thus this way of distinguishing between types of adsorption interactions is not applicable to materials that display stepped-sorption profiles.

Note that the PGDSC and sorption experiments were originally carried out for exploratory purposes without the initial intent of determining Q_{st} and thus the pressure ranges used, both in sorption and PGDSC experiments, do not include low pressure readings below 1 bar. In some cases, the sorption and PGDSC pressure ranges do not match entirely. Nevertheless, the PGDSC method was successfully applied and Q_{st} could be determined with the available data.

4.3 Summary

Owing to the high demand on the instrumentation, these experiments were not able to be repeated to verify results. However, what can be gained from these results is proof that the PGDSC method for direct isosteric heat determination can be applied to stepped sorption or any sorption profile and not limited to Type I. Q_{st} curves could be determined across the whole experimental pressure range, as opposed to just reporting the zero-loading value. This was achieved through one PGDSC and one sorption measurement at the same temperature, with no need for multiple isotherms over a range of temperatures, as is required with the conventional isosteric method.

The Q_{st} results for $[Cd(oba)(bpy)]_n$ show that the material has the highest affinity for CO_2 over N_2 and CH_4. The Q_{st} curves across the whole loading range are presented as the main results since the zero-loading value does not give information about the interaction of the gas with the framework in this system. Only at higher pressures, once the structural transformation has taken place, does the framework open up and take up large amounts of gas. Thus the zero-loading value for this compound is of little use.

The application of flexible PCPs and MOFs in industry depends on the study of all characteristics of the porous material, specifically thermodynamic properties. Thus gaining an estimate of the enthalpy of the

association/dissociation of the gas to a material is an important step in making porous PCPs a viable alternative for gas storage, separation and catalysis.

.

4.4 Crystallographic data

Table 4.2 Crystallographic data for all forms

Identification code	**Literature[6]**	**1a**	**1sq**	**1b**
Empirical formula	$C_{24}H_{16}CdN_2O_5$	$C_{26.86}H_{22.64}CdN_{2.97}O_{5.97}$	$C_{24}H_{16}CdN_2O_5$	$C_{24}H_{16}CdN_2O_5$
Formula weight	524.79	595.01	524.79	524.81
Temperature (K)	293(3)	100(2)	100(2)	100(2)
Wavelength (Å)	0.71073	0.71073	0.71073	0.71073
Space group	*C*2/*c*	*C*2/*c*	*C*2/*c*	$P2_1/c$
Unit cell dimensions (Å, °)	a = 16.329(4)	a = 15.453(6)	a = 15.453(6)	a = 15.503(3)
	b = 16.899(2)	b = 11.702(4)	b = 11.702(4)	b = 11.747(2)
	c = 17.410(3)	c = 29.745(13)	c = 29.745(13)	c = 13.629(2)
	β = 114.377(13)	β = 103.538(5)	β = 103.538(5)	β = 111.717(2)
Volume (Å^3)	4375.8(13)	5230(4)	5230(4)	2306.0(7)
Z	8	8	8	4
Calculated density (g cm^{-3})	1.593	1.511	1.333	1.465
Absorption coefficient (mm^{-1})	1.036	0.88	0.867	0.981
F (000)	2096	2403	2096	984
Crystal size (mm^3)	0.46×0.34×0.32	0.461×0.177×0.144	0.461×0.177×0.144	0.461×0.177×0.144
θ range for data collection (°)	1.82-27.50	2.206 to 28.339	2.217 to 25.000	2.237 to 28.225
Miller index ranges	Not reported	$-19 \le h \le 19$, $-15 \le k \le 7$, $-37 \le l \le 39$	$-18 \le h \le 18$, $-13 \le k \le 7$, $-35 \le l \le 35$	-17 h , 20, -15 ≤ k ≤ 13, -17 ≤ l ≤ 17
Reflections collected	5949	16383	13433	14248
Independent reflections	5040[R_{int} = 0.0379]	6145 [R_{int} = 0.0391]	4576 [R_{int} = 0.0361]	5433 [R_{int} = 0.0807]
Completeness to q_{max} (%)	Not reported	0.942	0.993	0.954
Max. and min. transmission	0.7321 and 0.6494	0.9100 and 1	0.9100 and 1	0.777 and 1
Refinement method	Not reported	Full-matrix least-squares on F2	Full-matrix least-squares on F2	Full-matrix least-squares on F2
Data / restraints / parameters	5040/0/289	6145 / 0 / 304	4576 / 0 / 289	5433 / 24 / 314
Goodness-of-fit on F2	1.081	1.069	1.048	0.993
Final R indices [I > 2s(I)]	R1 = 0.0408, wR2 = 0.1120	R1 = 0.0429, wR2 = 0.1100	R1 = 0.0274, wR2 = 0.0632	R1 = 0.0822, wR2 = 0.1911
R indices (all data)	R1 = 0.0501, wR2 = 0.1178	R1 = 0.0585, wR2 = 0.1194	R1 = 0.0349, wR2 = 0.0665	R1 = 0.1470, wR2 = 0.2273
Largest diff. peak and hole (e Å^{-3})	Not reported	1.524 and -0.623	0.343 and -0.310	3.960 and -1.244

4.5 References

1 S. Horike, S. Shimomura and S. Kitagawa, *Nat. Chem.*, 2009, **1**, 695–704.

2 R. Kitaura, K. Seki, G. Akiyama and S. Kitagawa, *Angew. Chem. Int. Ed.*, 2003, **42**, 428–431.

3 D. V. Soldatov, *J. Chem. Crystallogr.*, 2006, **36**, 747–768.

4 S. Horike, D. Tanaka, K. Nakagawa and S. Kitagawa, *Chem. Commun.*, 2007, 3395–3397.

5 D. Tanaka, K. Nakagawa, M. Higuchi, S. Horike, Y. Kubota, T. C. Kobayashi, M. Takata and S. Kitagawa, *Angew. Chemie - Int. Ed.*, 2008, **47**, 3914–3918.

6 Y. Ma, Y. He, L. Zhang, X. Wang, J. Gao and Z. Han, *Struct. Chem.*, 2007, **18**, 1005–1009.

7 K. Nakagawa, D. Tanaka, S. Horike, S. Shimomura, M. Higuchi and S. Kitagawa, *Chem. Commun.*, 2010, **46**, 4258–4260.

8 A. L. Spek, *Acta Crystallogr. Sect. C Struct. Chem.*, 2015, **71**, 9–18.

9 C. F. Macrae, P. R. Edgington, P. McCabe, E. Pidcock, G. P. Shields, R. Taylor, M. Towler and J. van de Streek, *J. Appl. Crystallogr.*, 2006, **39**, 453–457.

10 C. F. Macrae, I. J. Bruno, J. A. Chisholm, P. R. Edgington, P. McCabe, E. Pidcock, L. Rodriguez-Monge, R. Taylor, J. van de Streek and P. A. Wood, *J. Appl. Crystallogr.*, 2008, **41**, 466–470.

11 L. J. Barbour, *J. Supramol. Chem.*, 2001, **1**, 189–191.

12 L. J. Atwood, J. L. and Barbour, *Cryst. Growth Des.*, 2003, **3**, 3–8.

13 J. A. Mason, M. Veenstra and J. R. Long, *Chem. Sci.*, 2014, **5**, 32–51.

14 S. Alhasan, R. Carriveau and D. S.-K. Ting, *Int. J. Environ. Stud.*, 2016, **73**, 343–356.

15 G. Della Gatta, *Thermochim. Acta*, 1985, **96**, 349–363.

16 M. Bowker, *The Basis and Applications of Heterogeneous Catalysis.*, Oxford University Press, New York, 1998.

Chapter 5 Concluding remarks

5.1 Summary and conclusions

Although there have been significant advances in the characterisation of porous materials, there is still much room for improvement. To better understand a material, we need to probe, explore and accurately measure as many of its properties as possible. The thermodynamics of sorption is especially important, since this affects how a material functions in an industrial context, where PCPs are becoming more frequently used for separation, purification and storage. Knowing the affinities of a material for particular gases, as well the amount of heat released upon guest uptake, will ultimately aid in achieving energy efficiency during adsorption processes.

Isosteric heat is an estimation of sorption enthalpy and gives an indication of the affinity of the porous material for a gas. This can be used to determine the potential selectivity of the material before any breakthrough experiments have even been attempted. Ideally, Q_{st} values should be high enough for a material to have a good affinity for a gas, but it should also be low enough such that regeneration of the host material is not too energetically costly. Conventionally, Q_{st} is measured indirectly using the isosteric method, which employs sorption isotherms over a range of temperatures to obtain isosteres (a plot of ln$P$ vs 1/T at constant gas loading). The gradients of these linear plots are used to determine Q_{st}. This is an indirect method that is widely used because of its simplicity and convenient instrumental setup. The disadvantage of this method is that it makes several assumptions, such as ideal gas behaviour, temperature-independence of ΔH_{vap} of the sorbate gas, and it ignores the adsorbed gas volume. At high pressures, these assumptions can result in severe inaccuracies in the determination of Q_{st}. Shen *et al.* warn that isosteres should not be used uncritically and show that, at pressures above 1 bar, the isosteres deviate from linearity.[1]

The other commonly used method is conventional heat-flow calorimetry, where the heat flow is measured as a function of temperature under isobaric conditions. Fewer assumptions regarding the interaction energies and the system equilibrium are made with calorimetric approaches than with the isosteric method, and calorimetry is therefore a more desirable method for obtaining accurate data.

The PGDSC instrumentation was originally developed for the measurement of heat-flow events during gas sorption and desorption. These heat-flow profiles are helpful in monitoring structural transformations, especially in flexible PCPs that can change their propensity for gas-uptake at specific gas pressures. A consequence of this is that the heat flow can be used to directly determine Q_{st}. Chapter 2 describes the setup and procedure for Q_{st} measurement by means of PGDSC. The instrument consists of a microcalorimeter that is able to detect very small changes in heat flow. The microcalorimeter is connected to a gas syringe pump. The rate of compression and exact pressure settings are controlled by computer program developed in-house. This allows heat flow to be measured in a continuous manner at a rate that is slow enough to ensure quasi-equilibrium for the duration of the experiment.

The PGDSC method requires gas loading to be quantified over the pressure range of the experiment and at least one sorption isotherm is thus required. Together, gas loading and integral heat (Q^{int}) yield differential

heat (Q^{diff}). To determine Q_{st}, the thermodynamic term RT is added to Q^{diff} over the experimental pressure range.

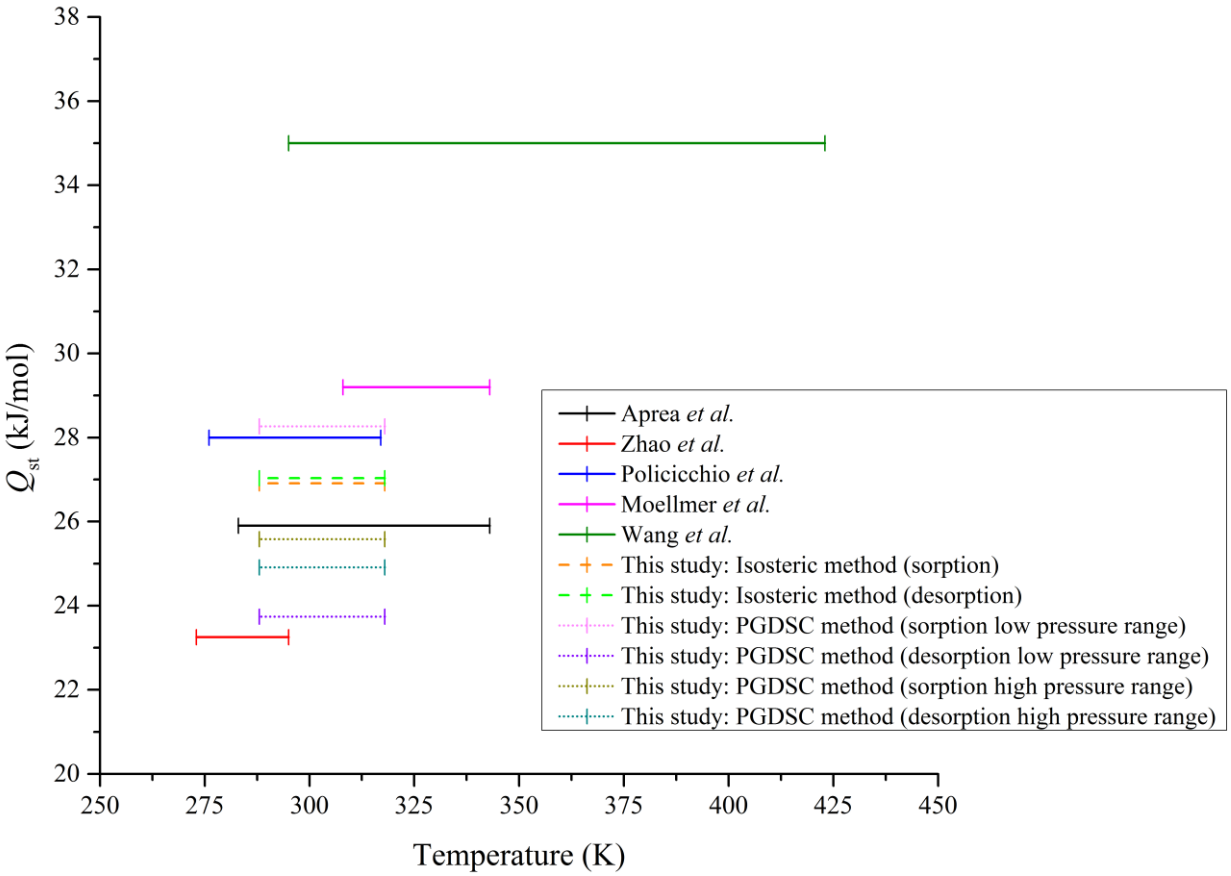

Figure 5.1 Collated Q_{st} results from Chapter 3 for CuHKUST with CO_2 gas plotted as a function of the temperature range used. Q_{st} values from the literature are also plotted. All values from the literature are for zero-loading, apart from those from Aprea *et al.*, which is an average value. All literature values were determined from the isosteric method.[2–6]

To validate the proposed method of determining Q_{st} directly, a test compound was used and the results compared to values determined from the isosteric method. The sorption of CO_2 by CuHKUST was chosen for this purpose since there are multiple studies reporting Q_{st} values in the literature, the majority of which make use of the indirect isosteric method. This makes CuHKUST a judicious choice for comparing experimental values to literature values and to thus determine whether the PGDSC method produces reliable results. Most of the Q_{st} values from the literature are reported at zero loading as this eliminates any contribution from adsorbate-adsorbate interactions and only considers adsorbate-adsorbent interactions. The experimental results are collated in Figure 5.1, including literature values determined using the isosteric method.[2–6] Comparison of the literature values reveals a trend related to the temperature range used. It appears that the higher the temperatures included in the temperature range, the higher is the calculated Q_{st} value. This is contrary to the assumption of temperature-independence by the Clausius-Clapeyron equation. Thus the isosteric method should therefore be viewed with caution. The experimental results obtained from the isosteric method, Figure 3.7, are comparable to the literature values obtained in the same manner. Moreover, the Q_{st} values determined from sorption and desorption data using the isosteric method are very similar, indicating little or

no hysteresis. The general downward trend of the curve with increasing loading can be attributed to the presence of a heterogeneous adsorbent surface, as discussed in Chapter 3.

The Q_{st} values determined using the PGDSC method show far less temperature dependence than those from the isosteric method. This is reflected in the low averaging errors over the four temperatures, the highest being 1.46 kJ/mol. This value is low compared to the differences in the literature values obtained over different temperature ranges (11.75 kJ/mol difference between the highest and lowest value). The experimental errors for the PGDSC procedure are negligible compared to those for the averaging results, see Section 3.3, and thus the errors shown for these experimental results are the averaging errors. The PGDSC Q_{st} values are comparable to those from the literature. However, they differ between the low pressure and high pressure ranges, as well as between Q_{st} values obtained from sorption and desorption. It must be noted that this comparison is between the zero-loading values only. The curves for the rest of the loading range compare well. The difference in zero-loading Q_{st} values between the two pressure ranges is most likely due to poor extrapolation of the higher pressure range curve. It is therefore recommended that only low-pressure data be used to obtain zero-loading Q_{st} values. Furthermore, it is recommended that zero-loading values only be used as a standard reference property of the material. We believe that it is more relevant, for practical purposes, to report the entire Q_{st} curve for information regarding the complete sorption process. The difference in zero-loading Q_{st} values obtained from sorption and desorption could be due to two reasons. Firstly, the changeover of the syringe pump from compression to expansion might have been too rapid and not enough time was allowed for equilibration, thus affecting the total heat measured. This could be remedied by adding a delay between the compression and expansion phases of the experiment. Secondly, there appears to be minor hysteresis at extremely low pressures, meaning that the desorption pathway is different to the sorption pathway and will thus yield different Q_{st} results. The Q_{st} curve for the low pressure range of CO_2 sorption by CuHKUST is fitted with an exponential decay curve fit, which yields higher Q_{st} values at low loading. Either this fit is not completely representative of the Q_{st} results, and extrapolation to the ordinate is therefore a poor estimate of zero-loading, or the linear fit for desorption does not reflect the true shape of the curve and very low loading data are needed in order to determine Q_{st} values that mirror those obtained from sorption.

Chapter 3 shows that the PGDSC method results in zero-loading Q_{st} values that are comparable to literature values for CO_2 sorption by CuHKUST. The method appears to be temperature independent, unlike the conventional isosteric method. In comparison to the multiple isotherm measurements required for the isosteric method, the PGDSC method is less labour intensive as only one isotherm and one PGDSC experiment (at the same temperature) are needed to obtain Q_{st} curves. Advances in combining instrumentation promote even simpler calorimetric experiments whereby simultaneous measurements of sorption and heat flow can be carried out for a less labour-intensive determination of Q_{st} in the future. The full Q_{st} curve should be reported to provide information for the full loading range for practical application. Care should be taken when fitting curves to these data if zero-loading values are required.

Q_{st} determinations were first developed for rigid porous materials such as zeolites and inflexible MOFs that exhibit Type I sorption isotherms with the assumption that no structural changes occur during the sorption

process. At zero loading, Q_{st} has been used to demonstrate the affinity of a framework for a certain gas by only taking into account the sorbent-sorbate interactions. At higher loading, the sorbate-sorbate interactions also contribute to the Q_{st} values. The study of *flexible* porous materials is still relatively new with few Q_{st} studies undertaken. These materials can undergo structural changes during the sorption process which will contribute to the overall Q_{st} values. For the purposes of this study, the Q_{st} equations developed for rigid porous materials were applied to a flexible material but it may be sensible to consider that the current Q_{st} definition may not be compatible with flexible materials. Reporting multiple Q_{st} values for different phases of the material (i.e. before and after inflection points) may be practical as the affinity of the framework after the structural change could drastically change. It was, however, beyond the scope of this study to attempt to distinguish between the different Q_{st} contributions, or to redefine the definition of Q_{st}.

One of the disadvantages of the isosteric method is that it can only be applied to Type I sorption isotherms. Chapter 4 shows how the PGDSC method can be applied to *any* porous material that can take up gas. A PCP, $[Cd(oba)(bpy)]_n$, with 2D interdigitated layers was chosen as a test compound as it displays stepped sorption as well as hysteresis in the sorption isotherms for CO_2, CH_4 and N_2 gas. The interdigitation of the layers causes the material to be flexible. When the material is activated, the layers move closer together to form a more closely packed (i.e. "closed") structure. The material exhibits gate-opening for all three gases at different pressures (each related to a specific gas); these gate-opening phenomena are evident as inflections in the sorption isotherms. At certain gas-specific pressures, the material undergoes a structural transformation from closed to open, causing a sudden uptake of the gas. The material also displays hysteresis in the N_2 sorption isotherm, which is unusual since interactions between the gas and the framework are minimal owing to the lack of a dipole moment in N_2.

For all three gases, heat-flow measurements show exothermic peaks corresponding to the gate-opening pressures. These peaks are due to the sudden uptake of gas as a result of opening of the structure. The heat associated with the structural transformation cannot be differentiated from the heat involved in gas uptake (heat of sorption). Since the "affinity" for the gas increases as the framework opens up, the exothermic peaks are reflected in the Q_{st} curves. Surprisingly, exothermic heat-flow peaks occur during the desorption phase for N_2 and CH_4 (Figures 4.23 and 4.24). This is unusual since desorption of gas molecules is typically an endothermic process. These exothermic peaks could partly reflect the heat associated with the structural transformation of the material from the open to the closed form. However, the peak due to the structural change could be partly masked by endothermic heat flow from gas desorption. The Q_{st} curve reflects this finding since it shows a "decrease" (i.e. becomes more positive) for the desorption phase, meaning that the framework experiences a decrease in affinity for N_2 and CH_4 as it returns to the closed phase. With regard to predictions of selectivity, $[Cd(oba)(bpy)]_n$ shows the highest affinity for CO_2 as compared to N_2 and CH_4 . However, breakthrough experiments[7], where the material is exposed to a mixture of gases and the breakthrough times are measured, would need to be carried out to confirm these predictions.

Previously, Q_{st} had been used to differentiate between chemisorption and physisorption. For materials with stepped sorption, this distinction is not recommended since as the large Q_{st} peaks are indicative of an abrupt

intake of gas as a result of a structural change in the material, and not necessarily indicative of chemisorption. The application of the PGDSC method can be extended to include flexible PCPs that display sorption profiles other than the typical Type I isotherms. This is an important step in extending the relevance and applicability of this method.

5.2 Future work

To further develop the PGDSC method, a second validation of the procedure needs to be carried out. A viable option is to use CuHKUST and a different gas for which there are multiple Q_{st} values reported in the literature (e.g. CH_4, as shown in Figure S1 in Appendix A). This method should then be applied to more types of compounds, covalent organic frameworks (COFs) and metallocycles, for example, where literature values exist for comparison. Subsequent to the completion of this study, the compression-expansion program of the syringe pump was improved to include a delay between the sorption and desorption processes. The anomalous Q_{st} result for temperature 308 K for sorption of CO_2 by CuHKUST needs further investigation to reveal the cause.

To improve the results presented in this study, the experiments with $[Cd(oba)(bpy)]_n$ should be repeated. Sorption isotherms and PGDSC measurements at low pressure would improve the Q_{st} results as well as help elucidate the exothermic peaks observed in the heat-flow measurements. Measurements to higher pressure (i.e. 70 bar) would complete the Q_{st} peak at high N_2 pressure. To ensure that all the heat-flow curves overlap well, the rate of pressure increase and decrease should be the same between the pressure ranges.

Specifically for $[Cd(oba)(bpy)]_n$, variable pressure SCXRD can be carried out in order to characterise the structural phase changes. The *in-house* developed environmental gas cell can be used to observe the layer movement in a single crystal as the gas pressure is increased or decreased, to shed light on the mechanism of gas uptake. To elucidate the partially observed exothermic peak for CH_4 uptake by $[Cd(oba)(bpy)]_n$, sorption isotherms and PGDSC measurements can be carried out at a higher temperature (e.g. 343 K, see Figure 4.25).

5.3 References

1 D. Shen, M. Burlow, F. Siperstein, M. Engelhard and A. L. Myers, *Adsorption*, 2000, **6**, 275–286.

2 P. Aprea, D. Caputo, N. Gargiulo, F. Iucolano and F. Pepe, *J. Chem. Eng. Data*, 2010, **55**, 3655–3661.

3 Y. Zhao, M. Seredych, J. Jagiello, Q. Zhong and T. J. Bandosz, *Chem. Eng. J.*, 2014, **239**, 399–407.

4 A. Policicchio, Y. Zhao, Q. Zhong, R. Agostino and T. Bandosz, *Appl. Mater. Interfaces*, 2014, **6**, 101–108.

5 Q. M. Wang, D. Shen, M. Bülow, M. Ling Lau, S. Deng, F. R. Fitch, N. O. Lemcoff and J. Semanscin, *Microporous Mesoporous Mater.*, 2002, **55**, 217–230.

6 J. Moellmer, A. Moeller, F. Dreisbach, R. Glaeser and R. Staudt, *Microporous Mesoporous Mater.*, 2011, **138**, 140–148.

7 M. S. P. Silva, M. A. Moreira, A. F. P. Ferreira, V. M. T. M. Silva, P. S. Gomes, M. Minceva, J. P. B. Mota and A. E. Rodrigues, *Chem. Eng. Technol.*, 2012, **35**, 1777–1785.

Appendix A: Supporting information

Chapter 3

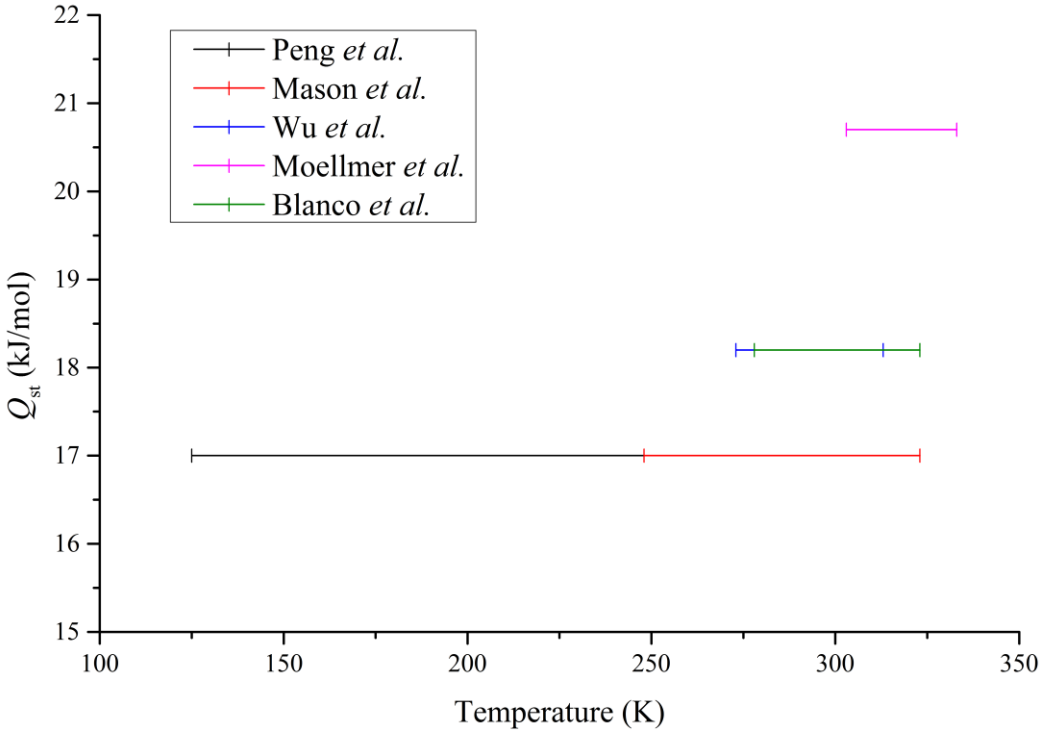

Figure S 1 Q_{st} values for CuHKUST with CH_4.[1–5]

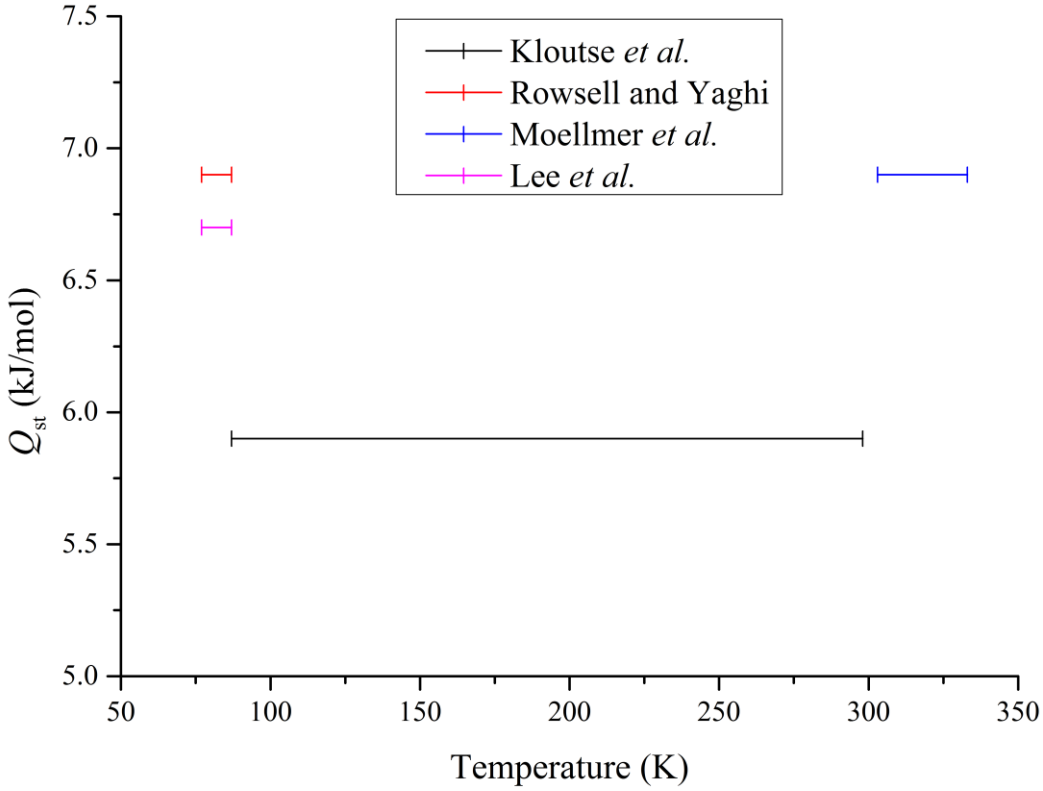

Figure S 2 Q_{st} values for CuHKUST with H_2.[4,6–8]

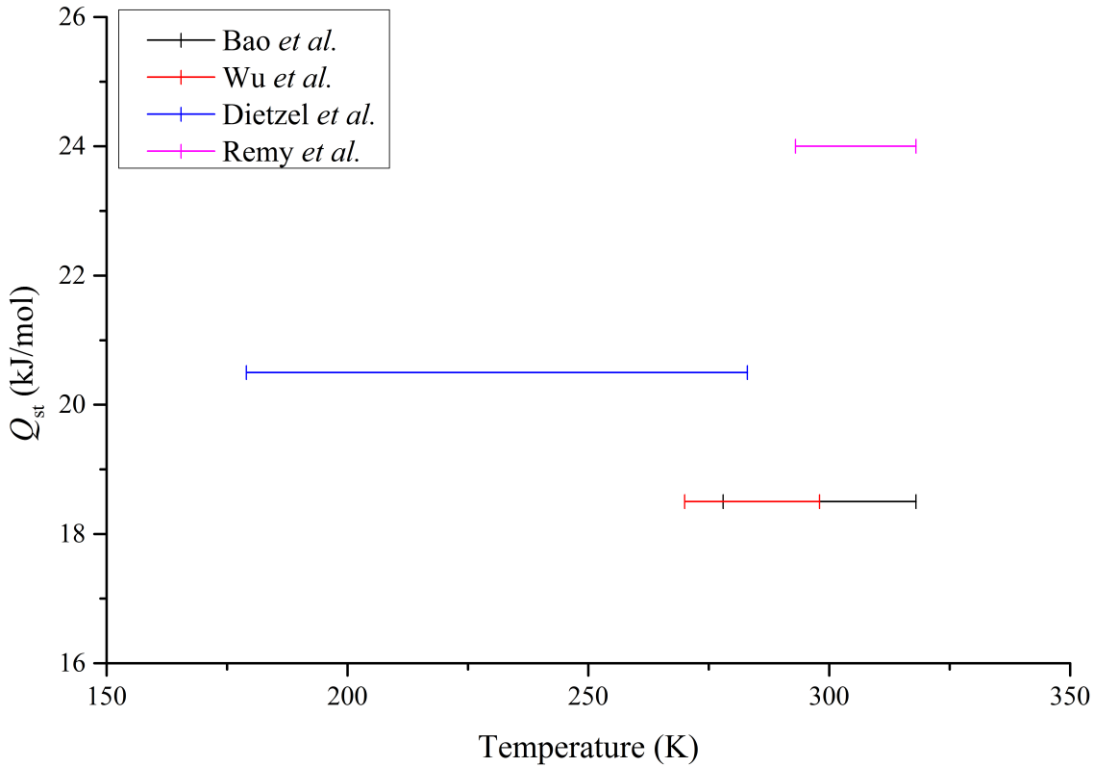

Figure S 3 Q_{st} values for Mg-MOF-74 with CH_4.[9–12]

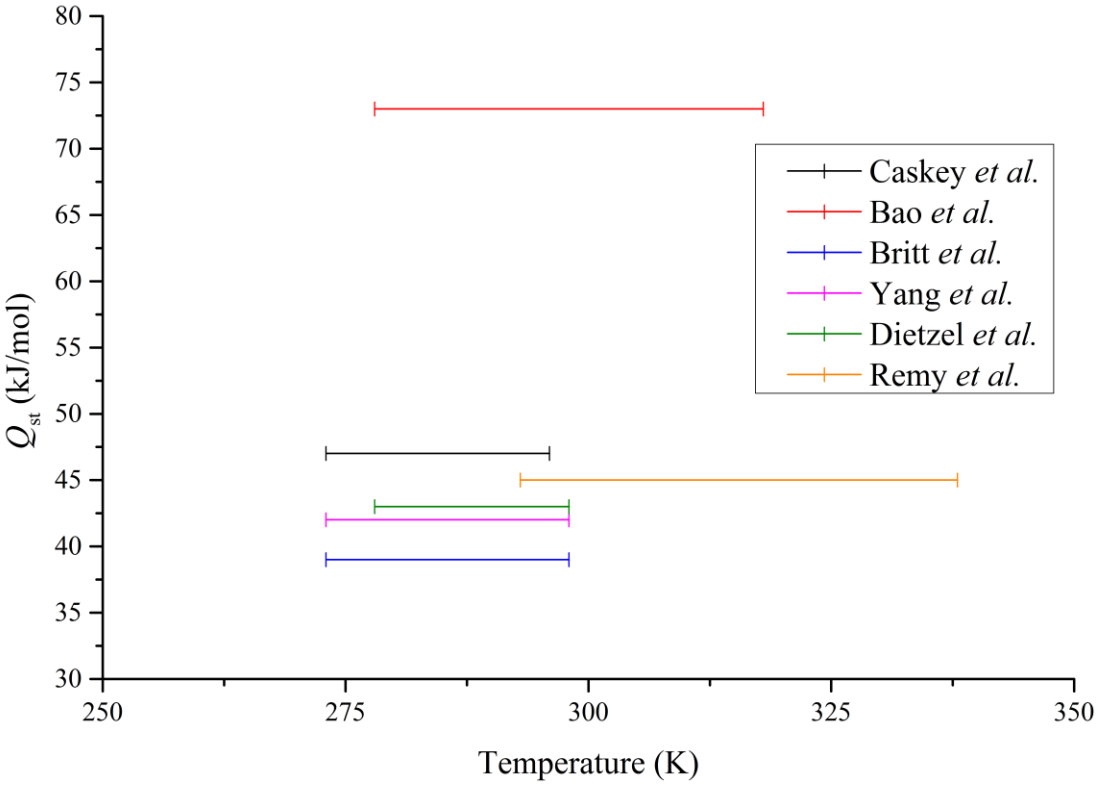

Figure S 4 Q_{st} values for Mg-MOF-74 with CO_2.[9,11–15]

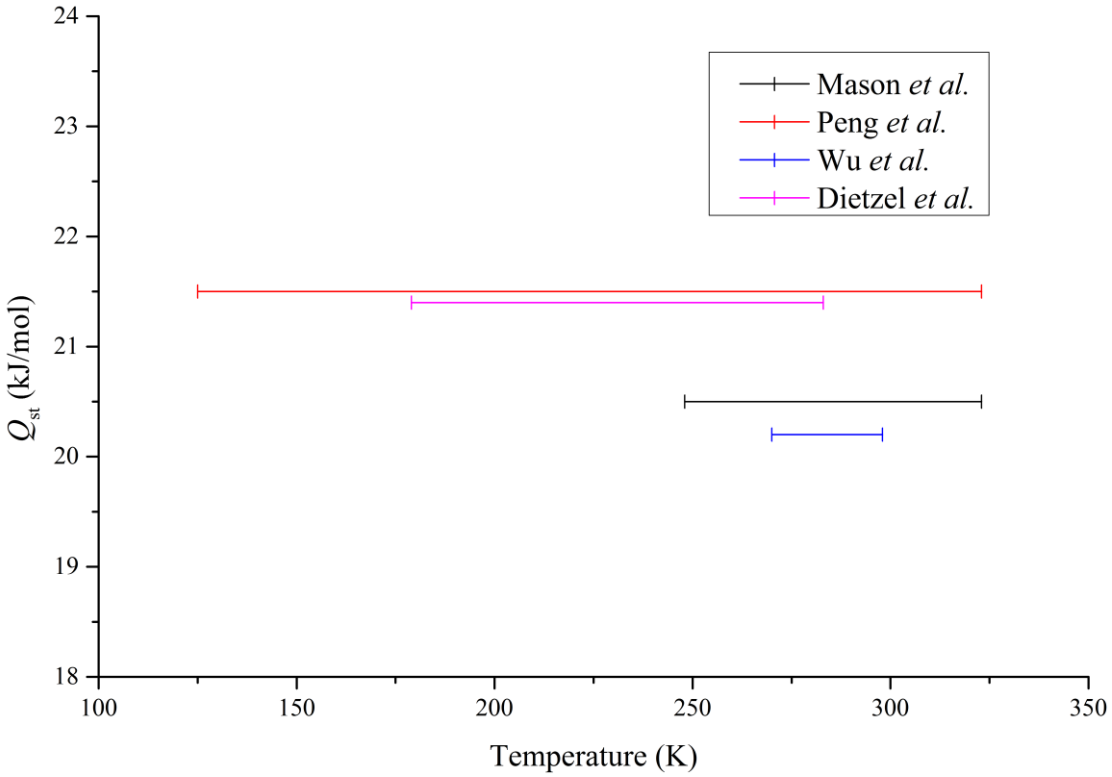

Figure S 5 Q_{st} values for Ni-MOF-74 with CH_4.[1,2,10,11]

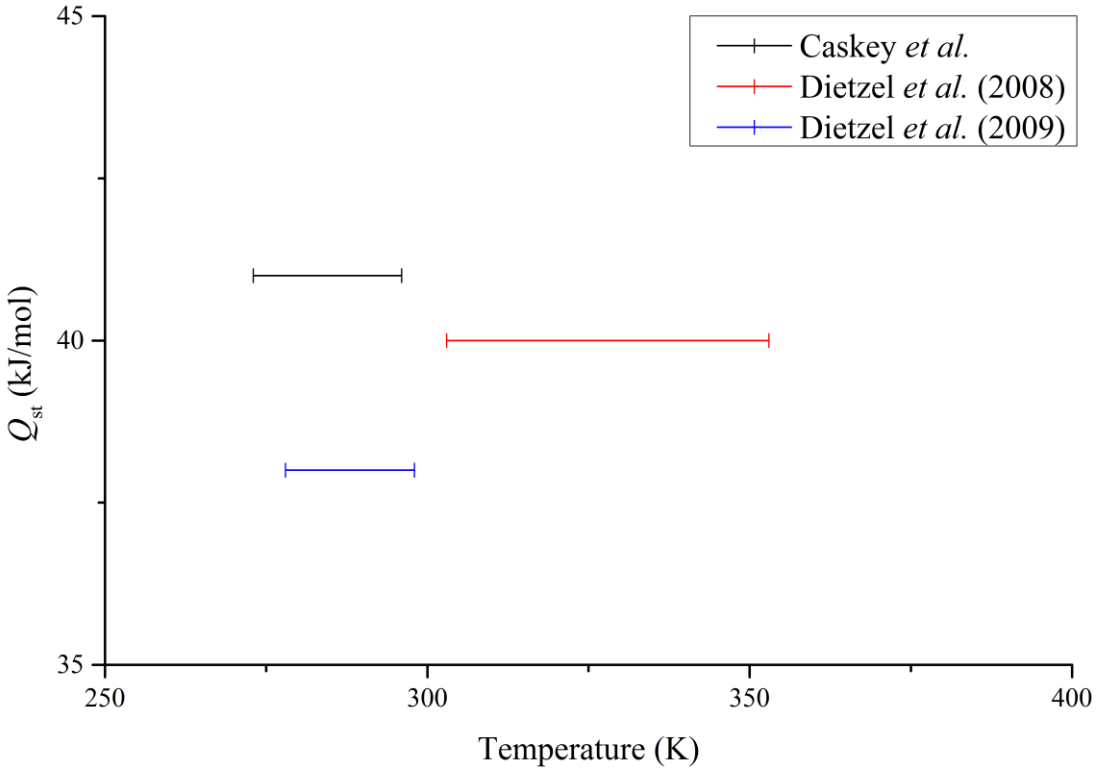

Figure S 6 Q_{st} values for Ni-MOF-74 with CO_2. [11,13,16]

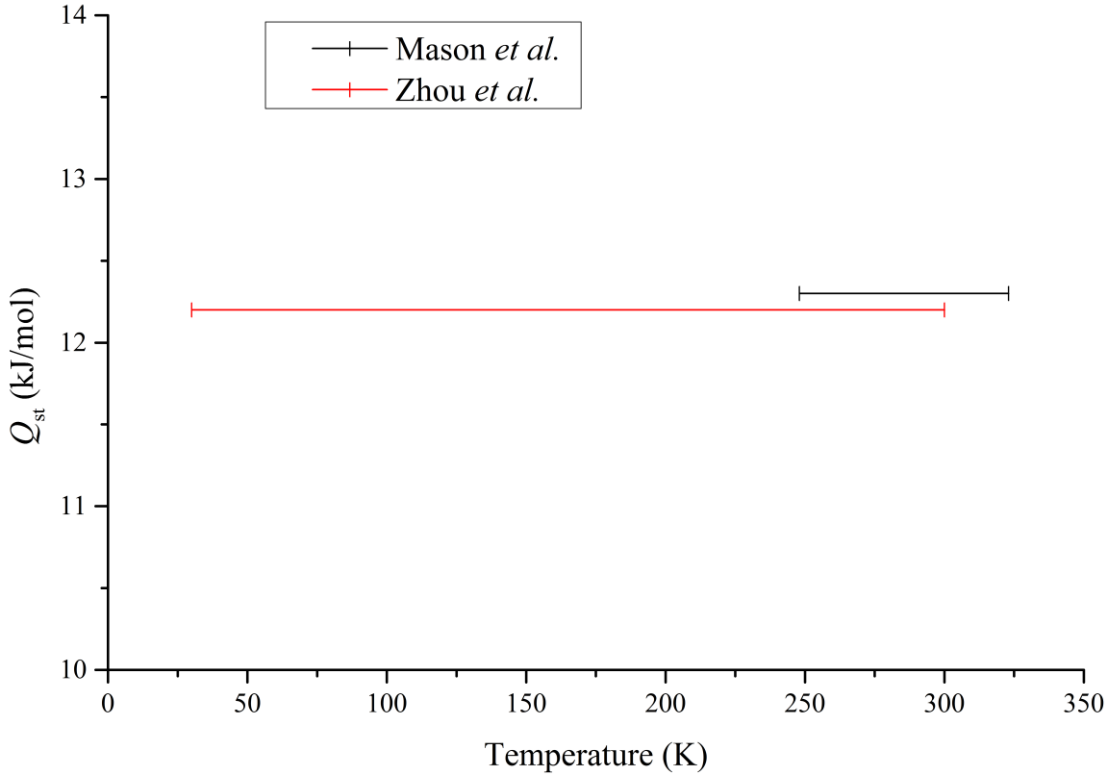

Figure S 7 Q_{st} values for MOF-5 with CH_4. [2,17]

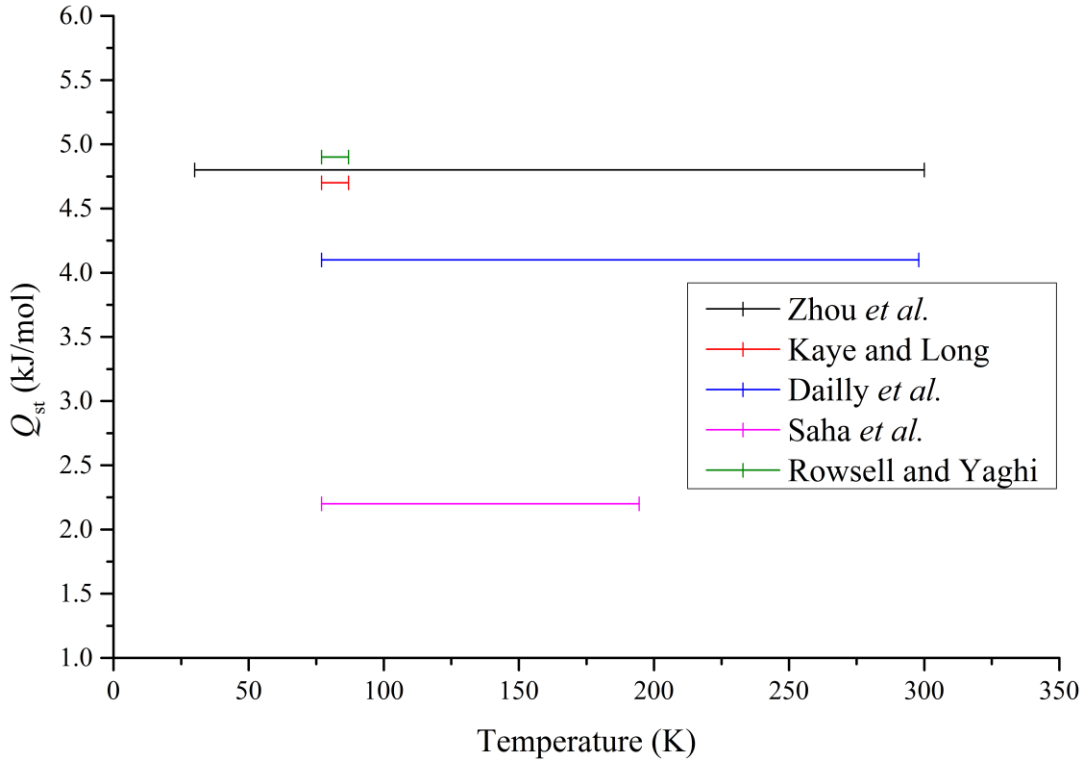

Figure S 8 Q_{st} values for MOF-5 with H_2.[7,17–20]

Table S 1 Fitting parameters and statistical analysis of the fitted curve for Q_{st} for CuHKUST with CO_2 obtained with the isosteric method in Figure 3.7.

Model	Parabola		
Equation	y = A + B*x + C*x^2		
Reduced Chi-Sqr	1.25E-04		
Adj. R-Square	1		
		Value	**Standard Error**
Q_{st}	A	26.91027	0.00156
Q_{st}	B	-0.29198	0.00266
Q_{st}	C	-0.02533	6.80E-04
Q_{st}	A	-27.0287	0.00237
Q_{st}	B	0.21252	0.0034
Q_{st}	C	0.02228	8.09E-04

Table S 2 Fitting parameters and statistical analysis of the fitted curve for sorption of CO_2 with CuHKUST data in Figure 3.8.

Model	LangmuirSCALED (User)			
Equation	y=(a*b*x)/(1+b*x)			
Reduced Chi-Sqr	5.79E-04	0.00129	1.17E-04	1.09E-04
Adj. R-Square	0.99991	0.99968	0.99996	0.99994
		Value	**Standard Error**	
Loading	a	15.01972	0.04927	
Loading	b	0.57394	0.00313	
Loading	a	16.85705	0.1638	
Loading	b	0.33405	0.00464	
Loading	a	16.31962	0.076	
Loading	b	0.2598	0.00164	
Loading	a	18.92044	0.18563	
Loading	b	0.15468	0.00185	

Table S 3 Fitting parameters and statistical analysis of the fitted curve for desorption of CO_2 with CuHKUST data in Figure 3.9.

Model	LangmuirSCALED (User)			
Equation	y=(a*b*x)/(1+b*x)			
Reduced Chi-Sqr	9.02E-04	0.00658	0.00622	5.36E-04
Adj. R-Square	0.99986	0.99855	0.99787	0.99976
		Value	**Standard Error**	
Loading	a	14.57241	0.05103	
Loading	b	0.61878	0.00364	
Loading	a	16.81227	0.33684	
Loading	b	0.34002	0.00973	
Loading	a	14.73596	0.40769	
Loading	b	0.30595	0.01188	
Loading	a	17.90932	0.35376	
Loading	b	0.16737	0.00408	

Table S 4 Fitting parameters and statistical analysis of fitted curve for Q_{st} data for the sorption of CO_2 with CuHKUST for 0.05-0.35 bar pressure range (sorption section) in Figure 3.13.

Model	ExpDec1		
Equation	y = A1*exp(-x/t1) + y0		
Reduced Chi-Sqr	0.06881		
Adj. R-Square	0.84863		
		Value	**Standard Error**
Q_{st}	y0	21.93025	0.10159
Q_{st}	A1	7.67904	3.12746
Q_{st}	t1	0.31116	0.07201
Q_{st}	k	3.21376	0.74379
Q_{st}	tau	0.21568	0.04992
Q_{st}	y0	23.59314	0.03671
Q_{st}	A1	5.92992	1.09547
Q_{st}	t1	0.29755	0.03264
Q_{st}	k	3.36081	0.36864
Q_{st}	tau	0.20624	0.02262
Q_{st}	y0	22.81091	0.02741
Q_{st}	A1	4.14414	0.75194
Q_{st}	t1	0.24844	0.02803
Q_{st}	k	4.02508	0.45415
Q_{st}	tau	0.17221	0.01943
Q_{st}	y0	23.2571	0.06236
Q_{st}	A1	3.75335	0.31449
Q_{st}	t1	0.2972	0.0319
Q_{st}	k	3.36476	0.36116
Q_{st}	tau	0.206	0.02211

Table S 5 Fitting parameters and statistical analysis of fitted curve for Q_{st} data for the sorption of CO_2 with CuHKUST for 0.05-0.35 bar pressure range (desorption section) in Figure 3.14.

Model	Line		
Equation	y = A + B*x		
Reduced Chi-Sqr	0.07721		
Adj. R-Square	0.88483		
		Value	**Standard Error**
Q_{st}	A	-22.7089	0.04477
Q_{st}	B	-0.91897	0.04313
Q_{st}	A	-24.7582	0.03555
Q_{st}	B	-0.11165	0.04774
Q_{st}	A	-22.6787	0.03991
Q_{st}	B	-0.42194	0.06608
Q_{st}	A	-24.8151	0.04193
Q_{st}	B	0.86012	0.102

Table S 6 Fitting parameters and statistical analysis of fitted curve for Q^{int} data for 0.25-2.0 bar pressure range (sorption section) in Figure 3.15a.

Model	Parabola		
Equation	y = A + B*x + C*x^2		
Reduced Chi-Sqr	415.4739		
Adj. R-Square	0.99994		
		Value	**Standard Error**
Q^{int}	A	-3832.61	6.56328
Q^{int}	B	1868.713	2.69814
Q^{int}	C	-10.1966	0.25813
Q^{int}	A	-2734.76	5.71836
Q^{int}	B	1902.987	2.93046
Q^{int}	C	-23.2126	0.34556
Q^{int}	A	-1793.97	4.28901
Q^{int}	B	1653.108	2.78031
Q^{int}	C	4.53325	0.40703
Q^{int}	A	-1326.59	4.49058
Q^{int}	B	1726.059	3.69404
Q^{int}	C	-12.7796	0.68585

Table S 7 Fitting parameters and statistical analysis of fitted curve for Q^{int} data for 0.25-2.0 bar pressure range (desorption section) in Figure 3.15b.

Model	Parabola		
Equation	y = A + B*x + C*x^2		
Reduced Chi-Sqr	181.9165		
Adj. R-Square	0.99997		
		Value	**Standard Error**
Q^{int}	A	-2778.24	3.46611
Q^{int}	B	1779.271	1.53671
Q^{int}	C	-12.1055	0.15536
Q^{int}	A	-1965.58	3.06707
Q^{int}	B	1850.096	1.71999
Q^{int}	C	-27.0919	0.21741
Q^{int}	A	-1384.83	3.44856
Q^{int}	B	1613.008	2.27049
Q^{int}	C	7.07173	0.33958
Q^{int}	A	-963.386	2.6054
Q^{int}	B	1701.924	2.30445
Q^{int}	C	-14.0805	0.4531

Table S 8 Fitting parameters and statistical analysis of fitted curve for Q_{st} data for 0.25-2.0 bar pressure range (sorption section) in Figure 3.16.

Model	Line		
Equation	y = A + B*x		
Reduced Chi-Sqr	1.67E-09		
Adj. R-Square	1		
		Value	**Standard Error**
Q_{st}	A	26.50063	3.98E-06
Q_{st}	B	-0.26307	7.61E-07
Q_{st}	A	27.0259	3.79E-06
Q_{st}	B	-0.59888	8.78E-07
Q_{st}	A	23.88563	3.40E-06
Q_{st}	B	0.11696	9.67E-07
Q_{st}	A	24.90982	3.48E-06
Q_{st}	B	-0.32971	1.24E-06

Table S 9 Fitting parameters and statistical analysis of fitted curve for Q_{st} data for 0.25-2.0 bar pressure range (desorption section) in Figure 3.17.

Model	Line		
Equation	y = A + B*x		
Reduced Chi-Sqr	2.38E-09		
Adj. R-Square	1		
		Value	**Standard Error**
Q_{st}	A	-25.3468	4.57E-06
Q_{st}	B	0.31232	8.80E-07
Q_{st}	A	-26.3436	4.29E-06
Q_{st}	B	0.69896	1.03E-06
Q_{st}	A	-23.3684	4.47E-06
Q_{st}	B	-0.18245	1.27E-06
Q_{st}	A	-24.5985	4.02E-06
Q_{st}	B	0.36327	1.48E-06

Chapter 4

Table S 10 Fitting parameters and statistical analysis of fitted curve for CO_2 sorption by 2 in Figure 4.19a.

Model	DoubleBoltzmann		
Equation	y = y0 + A * (frac / (1 + exp((x-x01)/k1)) + (1-frac) / (1 + exp((x-x02)/k2)));		
Reduced Chi-Sqr	0.13444		
Adj. R-Square	0.99837		
		Value	**Standard Error**
Pressure	y0	0.07337	0.26554
Pressure	A	6874.41917	0
Pressure	frac	2.78E-04	4.76E-05
Pressure	x01	0.60869	0.07648
Pressure	x02	4.96709	0.04477
Pressure	k1	-0.10671	0.05676
Pressure	k2	-0.37384	0.00815
Pressure	A1	1.91087	0.32708
Pressure	A2	6872.50831	0.32708
Pressure	EC50_1	1.83803	0.14058
Pressure	EC50_2	143.60775	6.42958

Table S 11 Fitting parameters and statistical analysis of fitted curve for CO_2 desorption by 2 in Figure 4.19b.

Model	BiDoseResp		

Equation	double Section1 = span*p/(1+pow(10,(LOGx01-x)*h1));
	double Section2 = span* (1-p)/(1+pow(10,(LOGx02-x)*h2));
	y=A1 + Section1 +Section2;
			double span = A2 - A1;

Reduced Chi-Sqr	4.40E-04	0.01566	
Adj. R-Square	0.99899	0.99981	
		Value	**Standard Error**
Pressure	A1	-0.02153	0.02152
Pressure	A2	58.6842	0
Pressure	LOGx01	3.26677	0.0685
Pressure	LOGx02	0.53288	0.01101
Pressure	h1	1.1123	0.0622
Pressure	h2	3.28879	0.31565
Pressure	p	0.98552	9.22E-04
Pressure	Span	58.70573	0.02152
Pressure	EC50_1	1848.2976	291.52467
Pressure	EC50_2	3.41101	0.0865
Pressure	A1	1.13889	0.28573
Pressure	A2	62503.83208	0
Pressure	LOGx01	3.37192	69.55793
Pressure	LOGx02	5.65808	381.9827
Pressure	h1	7.62589	4.03724
Pressure	h2	1.17451	0.25525
Pressure	p	0.4586	558.21383
Pressure	Span	62502.69319	0.28573
Pressure	EC50_1	2354.61647	377122.5585
Pressure	EC50_2	455069.9956	4.00E+08

Table S 12 Fitting parameters and statistical analysis of fitted curve for N_2 sorption by 2 in Figure 4.20a.

Model	BiDoseResp		

Equation	double Section1 = span*p/(1+pow(10,(LOGx01-x)*h1));
	double Section2 = span* (1-p)/(1+pow(10,(LOGx02-x)*h2));
	y=A1 + Section1 +Section2;
			double span = A2 - A1;

Reduced Chi-Sqr	6.04E-06		2.33E-05
Adj. R-Square	0.99976	0.99957	
		Value	**Standard Error**
N	A1	-14.26346	0
N	A2	3.442	0
N	LOGx01	-55.71301	1.49762
N	LOGx02	57.1216	1.67302
N	h1	0.02624	8.35E-04
N	h2	0.0879	0.00951
N	p	0.83365	5.34E-04
N	Span	17.70546	0
N	EC50_1	1.94E-56	6.22E-56
N	EC50_2	1.32E+57	5.10E+57
N	A1	0.43403	0.02301
N	A2	1.01832	0.00383
N	LOGx01	34.28008	1.56804
N	LOGx02	43.72768	0.14495
N	h1	0.30051	0.38018
N	h2	0.22028	0.01168
N	p	0.07324	0.0624
N	Span	0.58428	0.0222
N	EC50_1	1.91E+34	6.88E+34
N	EC50_2	5.34E+43	1.78E+43

Table S 13 Fitting parameters and statistical analysis of fitted curve for N_2 desorption by 2 in Figure 4.20b.

Model	BiDoseResp		

Equation	double Section1 = span*p/(1+pow(10,(LOGx01-x)*h1));
	double Section2 = span* (1-p)/(1+pow(10,(LOGx02-x)*h2));
	y=A1 + Section1 +Section2;
			double span = A2 - A1;

Reduced Chi-Sqr	3.99E-08	1.01E-05	
Adj. R-Square	0.99997	0.99989	
		Value	**Standard Error**
N	A1	-0.90173	0
N	A2	0.38326	0.0123
N	LOGx01	-7.56794	0.04853
N	LOGx02	0.05908	0.02185
N	h1	0.05177	0.00159
N	h2	18.46029	14.40037
N	p	0.99881	4.55E-04
N	Span	1.28498	0.0123
N	EC50_1	2.70E-08	3.02E-09
N	EC50_2	1.14573	0.05764
N	A1	-1.0342	0.25799
N	A2	1.0855	0.01498
N	LOGx01	-4.15268	4.44229
N	LOGx02	15.49342	0.05767
N	h1	0.024	0.00197
N	h2	0.48507	0.03453
N	p	0.89398	0.01189
N	Span	2.11971	0.27205
N	EC50_1	7.04E-05	7.20E-04
N	EC50_2	3.11E+15	4.14E+14

Table S 14 Fitting parameters and statistical analysis of fitted curve for CH_4 sorption by 2 in Figure 4.21a.

Model	Poly		
Equation	y = a0+a1*x+a2*x^2+a3*x^3+a4*x^4+a5*x^5+a6*x^6+a7*x^7+a8*x^8+a9*x^9;		
Reduced Chi-Sqr	0.08466		
Adj. R-Square	0.99974		
		Value	**Standard Error**
Pressure	a0	-0.01984	0.14511
Pressure	a1	23.09605	12.96039
Pressure	a2	-357.871	201.92891
Pressure	a3	2762.59	1232.78942
Pressure	a4	-9684.43	3812.37476
Pressure	a5	18546.79	6665.37245
Pressure	a6	-20811.2	6883.7765
Pressure	a7	13672.66	4166.3587
Pressure	a8	-4871.26	1367.12681
Pressure	a9	727.2105	187.85113

Table S 15 Fitting parameters and statistical analysis of fitted curve for N_2 desorption by 2 in Figure 4.21b.

Model	Poly		
Equation	y = a0+a1*x+a2*x^2+a3*x^3+a4*x^4+a5*x^5+a6*x^6+a7*x^7+a8*x^8+a9*x^9;		
Reduced Chi-Sqr	0.01518		
Adj. R-Square	0.99994		
		Value	**Standard Error**
Pressure	a0	0.07747	0.27262
Pressure	a1	-5.61593	10.25016
Pressure	a2	147.3967	122.3917
Pressure	a3	-749.922	666.62943
Pressure	a4	1789.695	1947.91001
Pressure	a5	-2233.27	3312.16304
Pressure	a6	1413.886	3379.81248
Pressure	a7	-306.311	2039.25284
Pressure	a8	-92.4834	670.46825
Pressure	a9	42.66858	92.57639

Table S 16 Fitting parameters and statistical analysis of fitted curve for integral heat for CO_2 sorption by 2 in Figure 4.26a.

Model	Poly		
Equation	y = a0+a1*x+a2*x^2+a3*x^3+a4*x^4+a5*x^5+a6*x^6+a7*x^7+a8*x^8+a9*x^9;		
Reduced Chi-Sqr	2.04949		
Adj. R-Square	1		
		Value	**Standard Error**
Q^{int}	a0	812980.6225	9115.64736
Q^{int}	a1	-205854.7192	1806.20949
Q^{int}	a2	22891.16257	148.43711
Q^{int}	a3	-1468.52941	6.37855
Q^{int}	a4	59.92157	0.14377
Q^{int}	a5	-1.61289	0.00176
Q^{int}	a6	0.02864	5.56E-05
Q^{int}	a7	-3.23E-04	1.13E-06
Q^{int}	a8	2.11E-06	1.06E-08
Q^{int}	a9	-6.04E-09	3.94E-11
Q^{int}	a0	-1.60E+10	22875.64968
Q^{int}	a1	2.37E+09	1070.15314
Q^{int}	a2	-1.55E+08	11.04216
Q^{int}	a3	5.91E+06	0.33806
Q^{int}	a4	-144685.3328	--
Q^{int}	a5	2355.66665	1.18E-04
Q^{int}	a6	-25.52525	2.59E-06
Q^{int}	a7	0.17751	1.87E-08
Q^{int}	a8	-7.19E-04	5.70E-10
Q^{int}	a9	1.29E-06	2.60E-12
Q^{int}	a0	-3.75E+08	782.37213
Q^{int}	a1	4.10E+07	29.81114
Q^{int}	a2	-1.99E+06	2.27454
Q^{int}	a3	55981.79516	0.05942
Q^{int}	a4	-1010.46926	2.72E-04
Q^{int}	a5	12.12079	1.08E-05
Q^{int}	a6	-0.09662	2.68E-07
Q^{int}	a7	4.94E-04	2.58E-09
Q^{int}	a8	-1.47E-06	1.22E-11
Q^{int}	a9	1.93E-09	2.36E-14

Table S 17 Fitting parameters and statistical analysis of fitted curve for integral heat for CO_2 desorption by 2 in Figure 4.26b.

Model	Poly		
Equation	y = a0+a1*x+a2*x^2+a3*x^3+a4*x^4+a5*x^5+a6*x^6+a7*x^7+a8*x^8+a9*x^9;		
Reduced Chi-Sqr	0.1232		
Adj. R-Square	1		
		Value	**Standard Error**
Q^{int}	a0	8.52E+08	1549.54137
Q^{int}	a1	-8.92E+07	87.4968
Q^{int}	a2	4.14E+06	1.83322
Q^{int}	a3	-111886.3912	0.01436
Q^{int}	a4	1941.35801	6.35E-05
Q^{int}	a5	-22.41966	1.78E-06
Q^{int}	a6	0.17232	1.03E-08
Q^{int}	a7	-8.50E-04	1.04E-10
Q^{int}	a8	2.44E-06	8.59E-13
Q^{int}	a9	-3.11E-09	2.28E-15

Table S 18 Fitting parameters and statistical analysis of fitted curve for integral heat for N_2 sorption by 2 in Figure 4.27a.

Model	Poly		
Equation	y = a0+a1*x+a2*x^2+a3*x^3+a4*x^4+a5*x^5+a6*x^6+a7*x^7+a8*x^8+a9*x^9;		
Reduced Chi-Sqr	0.12518	0.19416	
Adj. R-Square	0.99999	0.99996	
		Value	**Standard Error**
Q^{int}	a0	-22.67484	0.18497
Q^{int}	a1	11.28784	0.31334
Q^{int}	a2	10.35362	0.20657
Q^{int}	a3	-4.09803	0.07076
Q^{int}	a4	0.93188	0.01412
Q^{int}	a5	-0.12925	0.00173
Q^{int}	a6	0.01093	1.31E-04
Q^{int}	a7	-5.45E-04	6.00E-06
Q^{int}	a8	1.47E-05	1.52E-07
Q^{int}	a9	-1.64E-07	1.64E-09
Q^{int}	a0	-24560.88918	0
Q^{int}	a1	11592.3939	--
Q^{int}	a2	-2366.84687	--
Q^{int}	a3	275.20107	--
Q^{int}	a4	-20.02853	--
Q^{int}	a5	0.94662	--
Q^{int}	a6	-0.0291	--
Q^{int}	a7	5.62E-04	--
Q^{int}	a8	-6.20E-06	--
Q^{int}	a9	2.99E-08	--

Table S 19 Fitting parameters and statistical analysis of fitted curve for integral heat for N_2 desorption by 2 in Figure 4.27b.

Model	Poly		
Equation	y = a0+a1*x+a2*x^2+a3*x^3+a4*x^4+a5*x^5+a6*x^6+a7*x^7+a8*x^8+a9*x^9;		
Reduced Chi-Sqr	0.00793	0.02254	0.0098
Adj. R-Square	0.99999	0.99999	1
		Value	**Standard Error**
Q^{int}	a0	303.03323	--
Q^{int}	a1	-592.09295	--
Q^{int}	a2	466.71516	--
Q^{int}	a3	-198.26949	--
Q^{int}	a4	52.42342	--
Q^{int}	a5	-8.97595	--
Q^{int}	a6	0.99567	--
Q^{int}	a7	-0.06899	--
Q^{int}	a8	0.00271	--
Q^{int}	a9	-4.59E-05	--
Q^{int}	a0	-4003.59055	233.63819
Q^{int}	a1	980.82004	100.16242
Q^{int}	a2	51.30699	17.60788
Q^{int}	a3	-46.34462	1.54476
Q^{int}	a4	7.61634	0.04405
Q^{int}	a5	-0.65527	--
Q^{int}	a6	0.03361	--
Q^{int}	a7	-0.00104	5.18E-06
Q^{int}	a8	1.77E-05	1.28E-07
Q^{int}	a9	-1.30E-07	1.11E-09
Q^{int}	a0	1.09E+07	291.23333
Q^{int}	a1	-3.30E+06	56.70845
Q^{int}	a2	445413.0323	4.27014
Q^{int}	a3	-34963.06683	0.13483
Q^{int}	a4	1759.76746	--
Q^{int}	a5	-58.8937	--
Q^{int}	a6	1.31048	2.43E-06
Q^{int}	a7	-0.0187	7.10E-08
Q^{int}	a8	1.55E-04	1.12E-09
Q^{int}	a9	-5.71E-07	7.00E-12

Table S 20 Fitting parameters and statistical analysis of fitted curve for integral heat for CH_4 sorption by 2 in Figure 4.28a.

Model	Poly		
Equation	y = a0+a1*x+a2*x^2+a3*x^3+a4*x^4+a5*x^5+a6*x^6+a7*x^7+a8*x^8+a9*x^9;		
Reduced Chi-Sqr	0.08243	2.12074	
Adj. R-Square	1	0.99992	
		Value	**Standard Error**
Q^{int}	a0	838.67603	3.2317
Q^{int}	a1	-566.22746	2.09327
Q^{int}	a2	141.86652	0.5717
Q^{int}	a3	-17.93622	0.08654
Q^{int}	a4	1.37749	0.00802
Q^{int}	a5	-0.06803	4.73E-04
Q^{int}	a6	0.00217	1.78E-05
Q^{int}	a7	-4.30E-05	4.16E-07
Q^{int}	a8	4.81E-07	5.45E-09
Q^{int}	a9	-2.31E-09	3.07E-11
Q^{int}	a0	-2.35E+07	0
Q^{int}	a1	4.93E+06	--
Q^{int}	a2	-455165.6241	--
Q^{int}	a3	24296.81083	--
Q^{int}	a4	-826.3563	--
Q^{int}	a5	18.57035	--
Q^{int}	a6	-0.27574	3.45E-06
Q^{int}	a7	0.00261	6.04E-08
Q^{int}	a8	-1.43E-05	5.09E-10
Q^{int}	a9	3.44E-08	1.77E-12

Table S 21 Fitting parameters and statistical analysis of fitted curve for integral heat for CH_4 desorption by 2 in Figure 4.28b.

Model	Poly		
Equation	y = a0+a1*x+a2*x^2+a3*x^3+a4*x^4+a5*x^5+a6*x^6+a7*x^7+a8*x^8+a9*x^9;		
Reduced Chi-Sqr	0.29311	4.13732	
Adj. R-Square	0.99999	0.99993	
		Value	**Standard Error**
Q^{int}	a0	-3347.91474	10.22814
Q^{int}	a1	2237.98738	7.4282
Q^{int}	a2	-649.78601	2.27795
Q^{int}	a3	105.00547	0.38779
Q^{int}	a4	-10.36491	0.04049
Q^{int}	a5	0.65016	0.0027
Q^{int}	a6	-0.02603	1.15E-04
Q^{int}	a7	6.45E-04	3.05E-06
Q^{int}	a8	-9.02E-06	4.55E-08
Q^{int}	a9	5.45E-08	2.93E-10
Q^{int}	a0	1.50E+06	--
Q^{int}	a1	-366984.1351	--
Q^{int}	a2	39573.25156	--
Q^{int}	a3	-2461.70165	--
Q^{int}	a4	97.39877	--
Q^{int}	a5	-2.54296	1.35E-04
Q^{int}	a6	0.04383	1.94E-06
Q^{int}	a7	-4.81E-04	--
Q^{int}	a8	3.05E-06	--
Q^{int}	a9	-8.54E-09	--

References

1 Y. Peng, V. Krungleviciute, I. Eryazici, J. T. Hupp, O. K. Farha and T. Yildirim, *J. Am. Chem. Soc.*, 2013, **135**, 11887–11894.

2 J. A. Mason, K. Sumida, Z. R. Herm, R. Krishna and J. R. Long, *Energy Environ. Sci.*, 2011, **4**, 3030.

3 H. Wu, J. M. Simmons, Y. Liu, C. M. Brown, X. Sen Wang, M. Shengqian, V. K. Peterson, P. D. Southon, C. J. Kepert, H. C. Zhou, T. Yildirim and W. Zhou, *Chem. - A Eur. J.*, 2010, **16**, 5205–5214.

4 J. Moellmer, A. Moeller, F. Dreisbach, R. Glaeser and R. Staudt, *Microporous Mesoporous Mater.*, 2011, **138**, 140–148.

5 A. A. García Blanco, A. F. Vallone, S. A. Korili, A. Gil and K. Sapag, *Microporous Mesoporous Mater.*, 2016, **224**, 323–331.

6 A. F. Kloutse, R. Zacharia, D. Cossement, R. Chahine, R. Balderas-Xicohténcatl, H. Oh, B. Streppel, M. Schlichtenmayer and M. Hirscher, *Appl. Phys. A Mater. Sci. Process.*, 2015, 1417–1424.

7 J. L. C. Rowsell and O. M. Yaghi, *J. Am. Chem. Soc.*, 2006, **128**, 1304–1315.

8 J. Lee, J. Li and J. Jagiello, *J. Solid State Chem.*, 2005, **178**, 2527–2532.

9 Z. Bao, L. Yu, Q. Ren, X. Lu and S. Deng, *J. Colloid Interface Sci.*, 2011, **353**, 549–556.

10 H. Wu, W. Zhou and T. Yildirim, *J. Am. Chem. Soc.*, 2009, **2**, 4995–5000.

11 P. D. C. Dietzel, V. Besikiotis and R. Blom, *J. Mater. Chem.*, 2009, **19**, 7362.

12 T. Remy, S. A. Peter, S. Van Der Perre, P. Valvekens, D. E. De Vos, G. V. Baron and J. F. M. Denayer, *J. Phys. Chem. C*, 2013, **117**, 9301–9310.

13 S. R. Caskey, A. G. Wong-Foy and A. J. Matzger, *J. Am. Chem. Soc.*, 2008, **130**, 10870–10871.

14 D. Britt, H. Furukawa, B. Wang, T. G. Glover and O. M. Yaghi, *Proc. Natl. Acad. Sci. U. S. A.*, 2009, **106**, 20637–40.

15 D.-A. Yang, H.-Y. Cho, J. Kim, S.-T. Yang and W.-S. Ahn, *Energy Environ. Sci.*, 2012, **5**, 6465–6473.

16 P. D. C. Dietzel, R. E. Johnsen, H. Fjellvåg, S. Bordiga, E. Groppo, S. Chavan and R. Blom, *Chem. Commun. (Camb).*, 2008, **2**, 5125–5127.

17 W. Zhou, H. Wu, M. R. Hartman and T. Yildirim, *J. Phys. Chem. C*, 2007, **111**, 16131–16137.

18 S. S. Kaye and J. R. Long, *J.Am.Chem.Soc.*, 2005, **127**, 6506–6507.

19 A. Dailly, J. J. Vajo and C. C. Ahn, *J. Phys. Chem. B*, 2006, **110**, 1099–1101.

20 D. Saha, Z. Wei and S. Deng, *Sep. Purif. Technol.*, 2009, **64**, 280–287.